A 3-Axis Attitude Control System Hardware Design for a CubeSat

by

Jako Gerber

Thesis presented in partial fulfilment of the requirements for the degree of Master of Science in Engineering at Stellenbosch University

Department of Electrical and Electronic Engineering
University of Stellenbosch
Private Bag X1, 7602, Matieland, South Africa.

Supervisor: Prof. W.H. Steyn

December 2014

Declaration

By submitting this thesis electronically, I declare that the entirety of the work contained therein is my own, original work, that I am the sole author thereof (save to the extent explicitly otherwise stated), that reproduction and publication thereof by Stellenbosch University will not infringe any third party rights and that I have not previously in its entirety or in part submitted it for obtaining any qualification.

Signature: . . . .
J. Gerber

Date: . . . .

Copyright © 2014 Stellenbosch University
All rights reserved.

Abstract

With CubeSats becoming popular as a cheap alternative to larger satellites, the need for advanced miniature attitude determination and control systems (ADCS) arises to meet the pointing requirements of satellite operations such as earth imaging and orbit maintenance. This thesis describes the design of a complete ADCS for use on CubeSats. A previously designed CubeSat on-board-computer, CubeComputer, and fine sun and nadir sensor, CubeSense, is incorporated in the design. The remaining requirements with regard to sensors and actuators were met by CubeControl, an additional module, the design, manufacturing and testing of which are described. CubeControl can implement magnetic control with the use of a magnetometer and three magnetorquers. It is also capable of driving three reaction wheels for accurate active 3-axis stabilization.

Uittreksel

Met *CubeSats* wat gewild raak as 'n goedkoop alternatief tot groter satelliete ontstaan die behoefte vir gevorderde miniatuur oriëntasiebepaling en -beheerstelsels wat satelliet operasies soos aardwaarneming en wentelbaan korreksies moontlik maak. Hierdie tesis beskryf die ontwerp van 'n volledige oriëntasiebepaling en -beheerstelsel vir *CubeSats*. 'n Voorheen ontwikkelde *CubeSat* aanboordrekenaar, *CubeComputer*, en 'n fyn sonsensor en nadirsensor, *CubeSense*, is ingesluit in die ontwerp. Die orige benodighede met verband tot sensors en aktueerders word vervul deur *CubeControl*, 'n addisionele module waarvan die ontwerp, vervaardiging en toetsing beskyf word. *CubeControl* kan magnetiese beheer implementeer deur gebruik te maak van 'n magnetometer en drie magneetstange. Dit kan ook drie reaksiewiele aandryf vir akkurate aktiewe 3-as stabilisering.

Acknowledgements

In completing this work am deeply grateful to the following:

Prof W.H Steyn for his guidance and for providing me the opportunity to work and learn in the field of satellite engineering.

My fellow students, Willem Jordaan, Mike-Alec Kearney, Pieter Botma and Christo Groenewald for their input and support during trying times.

Johan Arendse for his friendly and skillful assistance.

Simorné Paulse, Aerolene Griebelaar and Denise Crowley for their warm-heartedness and friendly greetings.

Lourens Visagie for his crucial support on many projects.

Derik Wilbers for his unending friendship and understanding.

My family, for their endless love and support.

God, who put all these people across my path and gave everything needed for completing this work.

Contents

Declaration **i**

Abstract **ii**

Uittreksel **iii**

Acknowledgements **iv**

Contents **v**

List of Figures **ix**

List of Tables **xii**

Nomenclature **xiii**

1 Introduction **1**
- 1.1 Background 1
- 1.2 Study Objectives 2
- 1.3 Literature Review 3
  - 1.3.1 The CubeSat Standard 3
  - 1.3.2 Cubesat Trends 4
  - 1.3.3 Previous CubeSat Missions 5
  - 1.3.4 Reaction Wheel Comparison 11
- 1.4 Thesis Overview 12

2 Satellite Control Theory **13**
- 2.1 Orbit 13
- 2.2 Coordinate Frames and Satellite Attitude 14
- 2.3 Space Environment 15
  - 2.3.1 Geomagnetic Field 15
  - 2.3.2 Radiation 16

2.4 Sensors . . . 17
- 2.4.1 Magnetometers . . . 17
- 2.4.2 Rate Gyroscopes . . . 19

2.5 Actuators . . . 19
- 2.5.1 Magnetorquers . . . 19
- 2.5.2 Momentum Exchange Devices . . . 20

3 Design Overview **21**

3.1 Mission Description . . . 21

3.2 Hardware Requirements . . . 22

3.3 ADCS Composition . . . 24

3.4 CubeControl Module Overview . . . 25
- 3.4.1 Reaction Wheels . . . 26
- 3.4.2 Magnetic Torquer Rods . . . 26
- 3.4.3 Aerodynamic Paddles . . . 26
- 3.4.4 Magnetometer . . . 27
- 3.4.5 Coarse Sun Sensor . . . 27
- 3.4.6 Rate Sensors . . . 27

3.5 Preliminary Structural Layout . . . 27

3.6 Mass and Power Budget . . . 28

4 Hardware Implementation **31**

4.1 Reaction Wheels . . . 31
- 4.1.1 Motor . . . 32
- 4.1.2 Flywheel . . . 33
- 4.1.3 BLDC Motor Drivers . . . 33
- 4.1.4 Current Measurement . . . 35
- 4.1.5 Angular Encoders . . . 36
- 4.1.6 Mounting . . . 37
- 4.1.7 Magnetic Shielding . . . 37
- 4.1.8 Momentum Wheel . . . 39
- 4.1.9 Final Parameters . . . 40

4.2 Magnetorquers . . . 41

4.3 Rate Sensor . . . 45
- 4.3.1 LCG50-100 . . . 45
- 4.3.2 CRM200 . . . 48
- 4.3.3 Noise Analysis and Comparison . . . 50
- 4.3.4 Temperature Calibration . . . 51

4.3.5 Comparison 53

4.4 Aerodynamic Paddles 54

4.4.1 Stepper Motors 54

4.4.2 Optical Sensor 56

4.5 Magnetometer 58

4.5.1 Amplifier Circuit 58

4.5.2 Temperature Compensation 59

4.5.3 Set/Reset Strap 60

4.6 Coarse Sun Sensor 61

4.7 Microcontrollers 65

4.8 Power Switching 67

5 Software Design **69**

5.1 Goals 69

5.2 Overview 70

5.3 Scheduling 72

5.4 High Priority Interrupt 74

5.5 Magnetometer Subroutine 76

5.6 Momentum Wheel Subroutine 77

5.7 Rate Sensor Subroutine 79

6 Interfacing and Testing **80**

6.1 Interfacing Setup 80

6.2 Magnetometer Calibration 81

6.3 Reaction Wheel Control 83

6.3.1 Speed Measurement 83

6.3.2 Controller Model 87

6.3.3 Reaction Wheel Test Results 88

7 Conclusion **90**

7.1 ADCS Module Design 90

7.2 Hardware Development 90

7.3 Software Design 91

7.4 Other Missions 92

7.5 Further Recommendations 92

Bibliography **94**

Appendices **99**

A Mechanical Drawings **100**

B Simulink GUI **101**

List of Figures

1.1 Poly Picosatellite Orbital Deployer and cross section [1] 3
1.2 ADCS distributions [2] 5
1.3 ADCS sensors and actuators [2] 5
1.4 CanX-2 bus overview [3] 6
1.5 RAX satellites with the photodiodes circled. (a) RAX-1 (b) RAX-2 [4] 7
1.6 Dove CubeSats [5] 8
1.7 Orientations: a) during operations, b) max drag at EOM [6] 9
1.8 Engineering model of microwheel assembly [7] 9
1.9 Typical rotational wheel speed variation [8] 10
1.10 BRITE satellite [9] 10

2.1 Orbital elements [10] 13
2.2 Body- and orbit reference frames 15
2.3 Geomagnetic field intensity and direction [9] 15
2.4 The space radiation environment [11] 16
2.5 Wheatstone bridge and magnetic orientations of Magnetoresistive element [12,13] 18

3.1 ZACUBE-2 satellite model 22
3.2 Aerodynamic paddle roll actuation [14] 23
3.3 ADCS subsystems 24
3.4 CubeControl block diagram 25
3.5 ADCS layout 27

4.1 Reaction wheel system 31
4.2 Flywheel dimensions (mm) 33
4.3 Reaction wheel 37
4.4 Magnetic field standard deviation (Tesla) 38
4.5 Magnetic field bias 39
4.6 Magnetorquer implementation 42
4.7 CubeTorquer 42

4.8 Air coil magnetorquer structure prototype 43
4.9 LCG50 supporting circuitry 45
4.10 First order inverting low pass filter 46
4.11 Filtered angular rate measurements (note difference in scale) 47
4.12 MFB filter 47
4.13 CRM filtering 49
4.14 CRM measurements: Step input 49
4.15 CRM200 rate measurements with IIR filter 50
4.16 Allan variance 51
4.17 Noise on rate sensors with angular steps input 52
4.18 Rate drift during temperature variation 52
4.19 A3901 block diagram 55
4.20 A3901 block diagram 55
4.21 SG2BC posision on paddle 56
4.22 SG2BC circuit diagram 57
4.23 SG2BC accuracy test setup 57
4.24 MCU A/D output 57
4.25 HMC1053 implementation 59
4.26 Temperature calibration gains and errors 60
4.27 Magnetometer Set/Reset 60
4.28 Top and bottom of magnetometer PCBs 61
4.29 Photodiode Operational Amplifier circuit 62
4.30 Coarse sun sensor test 62
4.31 Coarse sun sensor test setup 63
4.32 Sun vector angles 63
4.33 Sensor output calibration 64
4.34 Coarse sun sensor accuracy 65
4.35 CubeControl power switching 67

5.1 Program flow overview 71
5.2 CubeControl 1s control period timing 72
5.3 Magnetometer analogue output during delays 74
5.4 I2C message structure 74
5.5 I2C ISR 75
5.6 Magnetometer subroutine 76
5.7 Motor subroutine 78

6.1 Interfacing setup 81

6.2 Magnetometers inside Helmholtz coil 82
6.3 Angle difference measurements at 3500 units / 5 ms 84
6.4 Slow speed measurements 85
6.5 Ramp speed measurement noise 86
6.6 Ramp speed noise 86
6.7 Reaction wheel closed loop model 87
6.8 Low speed transient response 88
6.9 High speed transient response 88

7.1 Mission specific CubeControl modules 92

List of Tables

1.1 Reaction wheel comparison 11

3.1 ADCS mass 28
3.2 ADCS power consumption 29
3.3 ADCS parameter comparison 29

4.1 Reaction wheel parameters 40
4.2 Reaction wheel power usage 41
4.3 Magnetorquer parameters 44
4.4 Rate sensor properties 53

6.1 Magnetometer baises and sensitivities 82
6.2 Magnetometer errors 83
6.3 Rollover correction 84

Nomenclature

Abbreviations and Acronyms

1-U	1-Unit
2-U	2-Unit
3-U	3-Unit
ADC	Analog-to-Digital Converter
ADCS	Attitude Determination and Control System
AMR	Anisotropic Magnetoresistive
BLDC	Brushless Direct Current
CCD	Charge-Coupled Device
CMG	Control Moment Gyros
CMOS	Complementary Metal-Oxide-Semiconductor
COTS	Commercial Off The Shelf
CPUT	Cape Peninsula University of Technology
DC	Direct Current
DCM	Direction Cosine Matrix
DMIPS	Dhrystone Million Instructions Per Second
DMOS	Double-diffused Metal-Oxide-Semiconductor
EDAC	Error Detection and Correction
EMF	Electromotive Force
EOM	End-Of-Mission

ESL	Electronic Systems Laboratory
FOV	Field Of View
GMR	Giant Magneto-Resitance
GNB	Generic Nanosatellite Bus
GPS	Global Positioning System
GUI	Graphical User Interface
I2C	Inter-Integrated Circuit
IC	Integrated Circuit
IGRF	International Geomagnetic Reference Field
ISR	Interrupt Service Routine
LEO	Low Earth Orbit
MCU	Microcontroller
MEKF	Multiplicative Extended Kalman Filter
MEMS	Micro-Electro-Mechanical Systems
MFB	Multiple Feedback
MI	Magneto-Inductive
NAND	Negative And
NMOS	N-type Metal-Oxide-Semiconductor
OBC	On-Board Computer
PCB	Printed Circuit Board
PMOS	P-type Metal-Oxide-Semiconductor
P-POD	Poly Picosatellite Orbital Deployer
PWM	Pulse Width Modulation
RMS	Root Mean Squared
RW	Reaction Wheel

SDT	Spin Dependent Tunnelling
SEE	Single Event Effects
SEL	Single Event Latchup
SEU	Single Event Upset
SPI	Serial Peripheral Interface
SRAM	Static Random Access Memory
SSDL	Space Systems Development Laboratory
TC	Telecommand
TID	Total Ionizing Dose
TLM	Telemetry
UART	Universal Asynchronous Receiver/Transmitter
UHF	Ultra High Frequency
USB	Universal Serial Bus
XOR	Exclusive Or

Uppercase Letters

X_O, Y_O, Z_O	Orbit coordinate axes
X_B, Y_B, Z_B	Satellite body coordinate axes
X_I, Y_I, Z_I	Inertially fixed coordinate axes
$\vec{\mathbf{F}}$	Force vector
$\vec{\mathbf{N}}$	Torque vector
$\mathbf{M}$	Magnetic dipole vector
$\mathbf{B}$	Geomagnetic vector
$\mathbf{I}$	Moment of inertia tensor
K	Constant gain

R_e	Earth's radius
T_s	Sampling time
P_t	Total power
A	Area

Lowercase Letters

a	Semimajor axis
e	Eccentricity
f_c	-3dB Cutoff frequency
i	Inclination
v	True anomaly
n	Number of windings
n_{ppr}	Number of pulses per revolution
m	Satellite mass
$\vec{\mathbf{a}}$	Acceleration vector
$\vec{\mathbf{h}}$	Angular momentum in momentum exchange devices
$\vec{\mathbf{r}}$	Position vector
f_{osc}	Internal clock frequency
l	Length

Greek Letters

Ω	Longitude of ascending node
ω	Angular rate
ω_p	Argument of periapsis
$\vec{\omega}^{B/I}$	Inertially referenced body angular rates
μ	Earth's gravitational constant

μ_t	Magnetic permeability of magnetorquers
α	Angular acceleration
τ	Torque

Chapter 1

Introduction

1.1 Background

Satellite technology has many applications, ranging from global telecommunication, earth observation and navigation to the advancement of various fields of science and our understanding of the solar system and the universe. The development of space technology is, however, hampered by high manufacturing and operational costs. These high costs are due, in part, to the long design time required for large, complex satellites and launching of heavy objects into space.

The advances in electronics have facilitated the miniaturization of satellite subsystems, allowing for smaller satellites, which are far less expensive to design, manufacture and launch. These lowered costs have made it feasible for universities to engage in satellite research and satellite missions. The CubeSat standard for nano-satellites has been especially popular.

One such university driven mission, ZACUBE-2, is being undertaken by the Cape Peninsula University of Technology (CPUT), working in collaboration with Stellenbosch University. The objective of this mission is to calibrate the radar antenna patterns of an antenna at the South African National Antarctic Program's SANAE base in Antarctica. Another CubeSat mission, DeOrbitSail, headed by the University of Surrey, aims to examine the effect of the aerodynamic forces acting on a large sail and proposes using it to rapidly deorbit a satellite. A larger project, the QB50 mission, will employ 50 CubeSats which will all be launched together. These satellites will study, in-situ, the temporal and spatial variations of a number of key constituents and parameters in the lower thermosphere. [15]

The satellite research group of the Electronic System Laboratory (ESL) at Stellenbosch University is focusing on developing attitude determination and control systems (ADCS) for nano-satellites and, in particular, for the aforementioned CubeSat missions. The system must include all the sensors required to accurately estimate the satellite orientation, the actuators required for pointing control, and the processing unit capable of executing the estimator and controller algorithms.

Jacoba Auret investigated the attitude control for ZACUBE-2, a 3-U CubeSat, within a simulation environment and designed control algorithms which satisfied the pointing accuracy criteria of the mission [14]. An On-Board-Computer (OBC) capable of executing the algorithms has been developed by Pieter Botma [16]. A fine sun sensor and nadir sensor module has also been developed by Hanco Loubser [17]. Research on driving electronics for magnetorquer rods, stepper motors and a magnetometer has been done by Philip May [18].

1.2 Study Objectives

This thesis focuses on the design, development and testing of a system capable of interfacing with all the sensors and actuators required for the ADCS of a CubeSat. The system needs to fit onto one CubeSat sized PCB (10 cm × 10 cm). Consideration must be given to the research already done and the hardware already developed. The PCB must complete the ADCS suite and meet all remaining requirements with regard to sensors and actuators. Development of the module will include the following steps:

- Research the attitude control performed on previous CubeSat missions
- Investigate the performance of current sensors and actuators commercially available for CubeSats
- Establish the requirements of the ADCS and decide on what control hardware to use
- Do the schematic and PCB design of the module
- Write microcontroller firmware and interfacing programs for the module
- Test the module via a computer and the OBC
- Take sensor measurements to determine performance results
- Test hardware in conjunction with other ADCS modules

As the requirements of missions vary, the design must be adjustable to meet the specific needs of each mission.

1.3 Literature Review

In this section the CubeSat standard is defined and general CubeSat trends are given. Recent CubeSat missions, relevant to ADCS, are then discussed, followed with a comparison of reaction wheels currently available.

1.3.1 The CubeSat Standard

The CubeSat Project was started in 1999 by Prof. Jordi Puig-Suari at California Polytechnic State University (Cal Poly), San Luis Obispo, and Prof. Bob Twiggs at Stanford University's Space Systems Development Laboratory (SSDL) as an attempt to reduce the cost and development time of satellites, increase accessibility to space and sustain frequent launches. [1] This was specifically done to facilitate student satellite projects, but CubeSats can also serve as facilities for in-space experimentation and space-qualifying future small-satellite hardware. [19]

A 1-U CubeSat is a 10 cm × 10 cm × 10 cm cube with a mass of less than 1.33 kg. CubeSats can also be classified as 2-U (20 cm × 10 cm × 10 cm) or 3-U (30 cm × 10 cm × 10 cm). Cal Poly has set specific mechanical, electrical, operational and testing requirements to which the satellite must conform. A deployment system for CubeSats has also been developed by Cal Poly. The Poly Picosatellite Orbital Deployer (P-POD) can carry up to three CubeSat units. Using the P-POD simplifies the integration of the CubeSats with the launch vehicle. The P-POD is shown in figure 1.1.

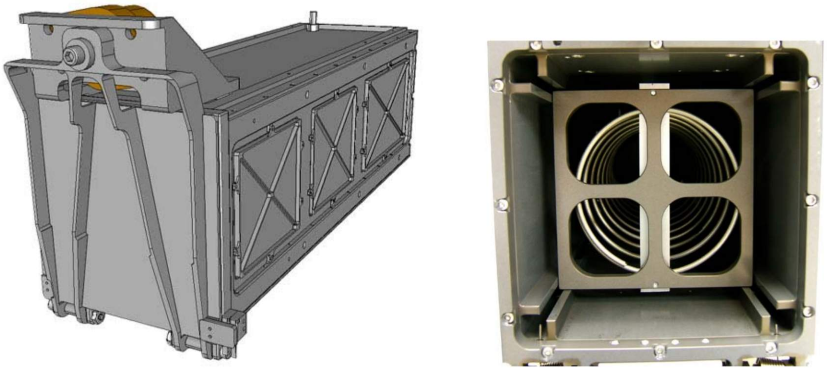

Figure 1.1: Poly Picosatellite Orbital Deployer and cross section [1]

At the moment of deployment the launch vehicle will activate the release mechanism of the P-POD. A set of torsion springs at the door hinge forces the door open, and the CubeSats, gliding on the P-POD rails, are deployed by the main spring.

The first six CubeSats, one commercial and 5 university CubeSats, were launched on 30 June 2003 from Plesetsk, Russia. The CubeSats were CUTE-I, a single CubeSat built by the Tokyo Institute of technology, XI-IV, built by University of Tokyo, QuakeSat, a 3-U by Stanford University, AAUsat by Alborg University, DTUsat by Technical University of Denmark and CanX-1 by the University of Toronto. CUTE-I used piezoelectric vibrating gyroscopes, a dual axis accelerometer and a complementary metal-oxide-semiconductor (CMOS) sun sensor for attitude determination [20]. The satellite did not control its attitude. XI-IV used a permanent magnet and hysteresis rods for passive attitude control. CanX-1, DTUsat and AAUsat attempted ADCS using sun sensors, magnetometers and magnetorquers, but proper communication was never established [21]. QuakeSat also used a permanent magnet and hysteresis rods. Since then over 200 Cubesats have been launched [22].

1.3.2 Cubesat Trends

The most common CubeSat objective is technology demonstration, although only 14% of CubeSats have technology demonstration as its sole objective [2]. More than half of CubeSats are also built with an educational objective. About half of CubeSats have operational objectives such as radio communications or taking scientific measurements.

CubeSats are typically launched into low Earth orbit (LEO) where the radiation exposure to the satellite is relatively low due to the shielding of the earth's magnetosphere. As commercial-off-the-shelf (COTS) components, which are less expensive than radiation hardened components, are often used on CubeSats, higher orbits are not sustainable. Space debris guidelines also specify a required deorbiting time for CubeSats, which is difficult to achieve for high altitude missions. De-orbiting concepts that exploit atmospheric drag by increasing the satellite surface area have been demonstrated by AeroCube 2 and 3. Propulsion systems that have been developed for CubeSats include vacuum arc thrusters, colliod thrusters, pulsed-plasma thrusters, and MEMS cold-gas thrusters [23].

The ADCS capabilities of nano-satellites are, in general, still in early development phase and does not allow for precise remote sensing or ground station tracking [2]. In figure 1.2 and figure 1.3 the distributions of the various attitude control techniques and hardware used by pico- and nano-satellites as of 2010 as found in a survey done by Bouwmeester and Guo [2].

We can see that most CubeSats only do rotational damping, which is important for reliable power generation and communication [2]. The best control accuracy as of 2012 was achieved by CanX-2, which could control the satellite to overall control accuracies

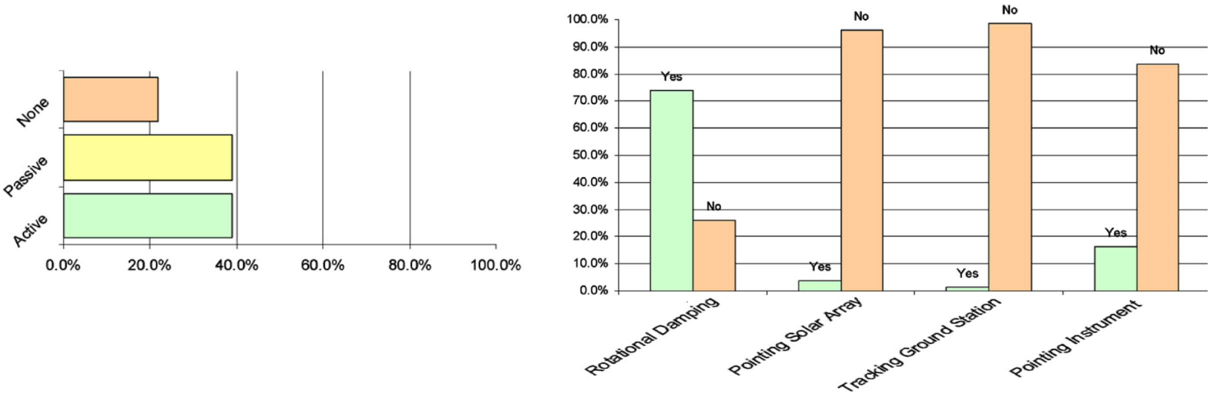

Figure 1.2: ADCS distributions [2]

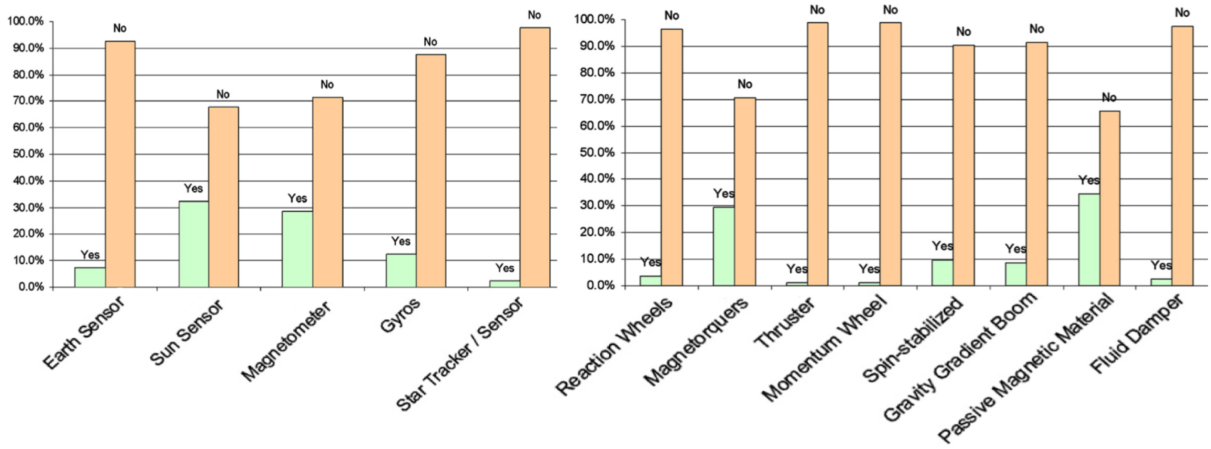

Figure 1.3: ADCS sensors and actuators [2]

better than 2^o [24]. More recently the RAX satellites, which uses passive magnetic control, achieved 1 σ estimation accuracies of better than 0.5^o [4].

1.3.3 Previous CubeSat Missions

In this section a few CubeSat and nano-satellite missions of interest with regard to ADCS are discussed. These missions include CanX-2, the RAX satellites, the Flock-1 constellation, BEESAT and the BRITE satellites.

1.3.3.1 CanX-2

CanX-2, a 3-U CubeSat developed by the University of Toronto's Space Laboratory, was launched in April 2008 into a 635km sun synchronous orbit with a 9:30 am descending node [3]. The mission objectives for CanX-2 include testing hardware which will be used on the CanX-4 and CanX-5 formation flying missions, and providing access to space for the research and development community in Canada. Its payloads include an atmospheric spectrometer and a GPS atmospheric occultation experiment [25].

The satellite features an ARM7-based processor with 3 MB of SRAM which implements EDAC protection [26]. GaAs solar cells generate the electrical power which is stored in a lithium-ion battery. A UHF custom full-duplex radio, which operates at 4000 bps, is used for the uplink while a SFL-developed S-band transmitter, which operates between 32 kbps and 1 Mbps, is used for the downlink [3]. A liquid fueled cold-gas propulsion system, necessary for the formation flying, was also flown.

The ADCS consists of a set of sun sensors, a magnetometer, three orthogonal reaction wheels and magnetorquer coils. The wheels have a maximum torque capability of 3 mNm and maximum momentum storage of 30 mNms.

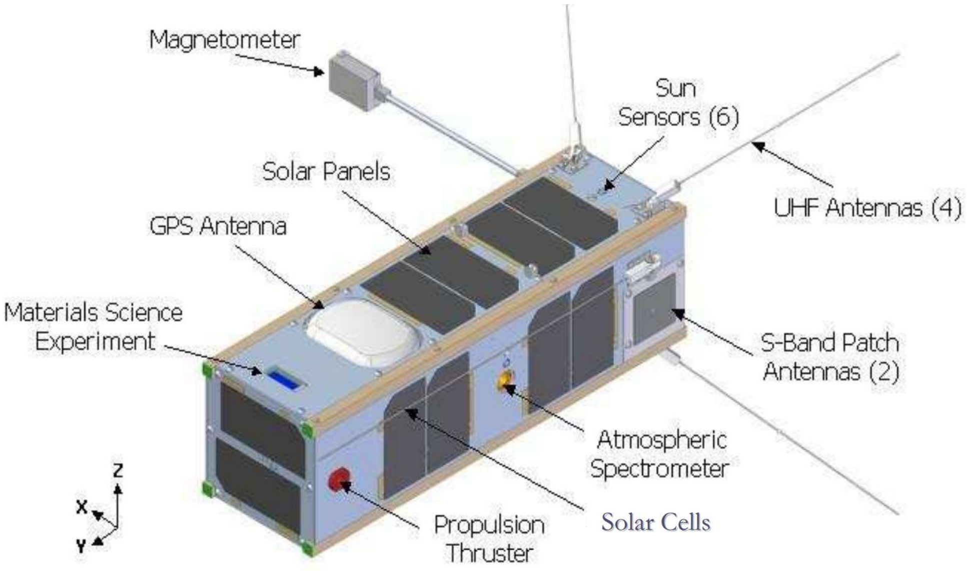
Magnetometer
Sun Sensors (6)
UHF Antennas (4)
Solar Panels
GPS Antenna
Materials Science Experiment
S-Band Patch Antennas (2)
Atmospheric Spectrometer
Solar Cells
Propulsion Thruster
Z
X
Y

Figure 1.4: CanX-2 bus overview [3]

The satellite achieved an attitude determination accuracy of about $\pm 1.5^o$ and a pitch control accuracy of about 2^o, which was derived by comparing the flight telemetry with the modeled performance. The nominal alignment mode for CanX-2 is orbit-normal, with a bias in the wheel. One issue that arose was a parasitic dipole on the wheel, but this was compensated for using the magnetorquers. An ongoing issue is that the coarse sun sensors periodically select the incorrect fine sun sensor due to higher than expected albedo influence and sensor filter effects [25].

1.3.3.2 RAX-1 and RAX-2

The Radio Aurora Explorer (RAX) satellites are 3-U CubeSats launched in November 2010 (RAX-1) and October 2011 (RAX-2) [4]. They were designed to study the magnetic field-aligned irregularities in the electron density of the Earth's ionosphere, which is an aspect of space weather. The mission has a 5^o attitude determination requirement. The satellites use permanent magnets which aligns the spacecraft with the Earth's magnetic field. Hysteresis rods are used to dissipate rotational kinetic energy. Springmann and Cutler [4] reports oscillations of approximately $\pm 20^o$ about the magnetic field vector and a $1 - 2^o$/s spin around the magnetic field vector during steady state.

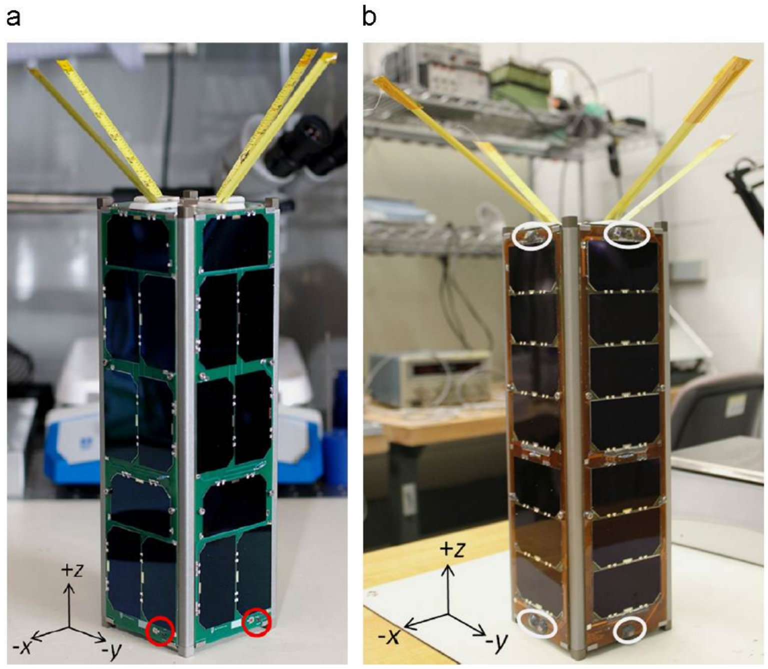

Figure 1.5: RAX satellites with the photodiodes circled. (a) RAX-1 (b) RAX-2 [4]

The ADS on the RAX satellites include Osram SFH430 photodiodes that act as coarse sun sensors, a PNI MicroMag3 magnetometer and an ADIS16405 inertial measurement unit, which includes a three-axis MEMS rate gyroscope and another magnetometer [4]. On the RAX-1 satellite a photodiode is mounted on each x/y facet, two on the -z facet and three on the +z facet. The redundant sensors were added because of possible shadowing by the antennas. As the photodiodes did not have a full 180^o FOV, the sun sensor did not provide coverage over the entire body-fixed frame. On the RAX-2 satellite extra photodiodes were added at offset angles to the satellites facets to provide better coverage and to verify sensor parameters and performance. Another change made to the photodiodes from RAX-1 to RAX-2 was the addition of coverglass, which prevented degradation due to radiation.

After in-orbit calibration methods, including the multiplicative extended Kalman filter (MEKF), was developed and used to estimate and compensate for various sensor errors, attitude estimation accuracies better than 0.5^o 1-sigma was demonstrated with the RAX flight data [4].

1.3.3.3 Flock-1 constellation

A recent commercial CubeSat venture is Planet Labs' Flock 1 constellation. It is currently made up of 28 3-U earth-imaging CubeSats, with an imagery ground resolution of 3 to 5 meters. The satellites, called Doves, were all deployed on February 2014 into a 400 km orbit with an inclination of 52^o [5, 27]. Planet Labs announced that it plans on bringing the total number of satellites to 131 within a year, making it possible to create a daily photo mosaic of most of Earth [28].

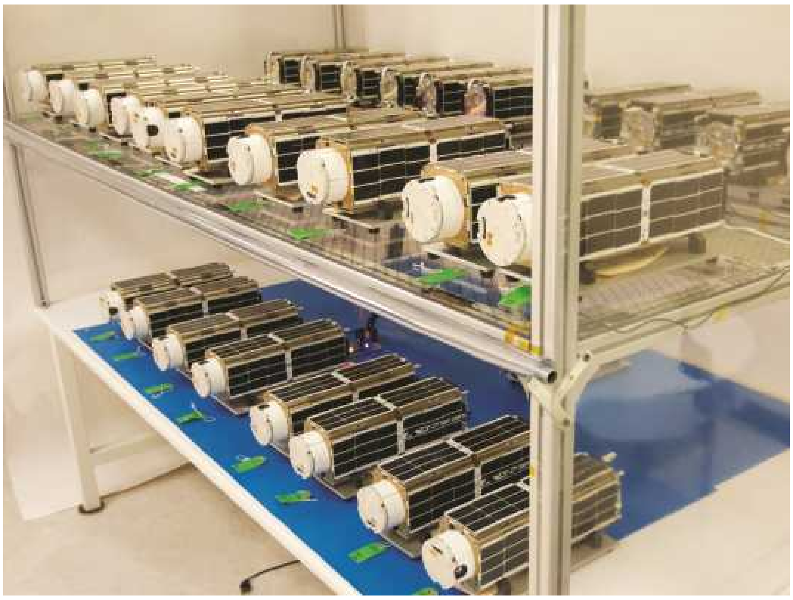

Figure 1.6: Dove CubeSats [5]

The Dove-1 CubeSat was launched in April 2013, into a 241 km × 257 km orbit [29]. Within the 6-day mission period the satellite successfully stabilized and downloaded pictures. It also performed fine attitude pointing using reaction wheels. The Dove-2 CubeSat, launched in April 2013 in an 300 km × 575 km orbit was also sucsessful in downloaded pictures, but only used magnetorquers for stabilization.

The Dove-3 and Dove-4 satellites were launched in November 2013 into an 800 km × 597 km and a 700 km circular orbit respectively, at an inclination of 97.8^o [27].

Dove-3 uses 3 coil magnetorquers as attitude control actuator. After the despinning of the satellite the magnetorquers locks it to the magnetic field and performs 3-axis control [6].

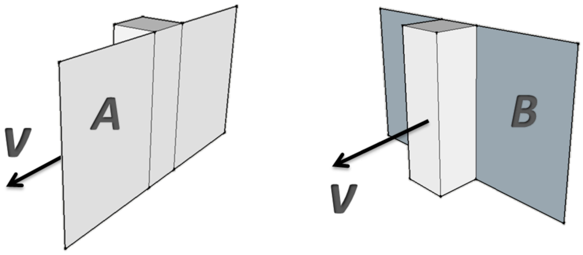

Figure 1.7: Orientations: a) during operations, b) max drag at EOM [6]

The nominal operation attitude is shown in figure 1.7, with **V** pointing in the satellite velocity vector and the **A** plane facing the sun. The 30 cm bus axis is nadir pointing. At end-of-mission (EOM) the satellites assumes the orientation shown in figure 1.7b, which is dynamically stable due to gravity gradient and aerodynamic torques [6].

1.3.3.4 BEESAT

BEESAT-1, a 1-U CubeSat developed by the Technical University of Berlin, was launched in September 2009 into a sun-synchronous, near-circular orbit with an altitude of 720 km and an inclination of 98°. The main goal of BEESAT-1 was to flight test a microwheel system, shown in figure 1.8.

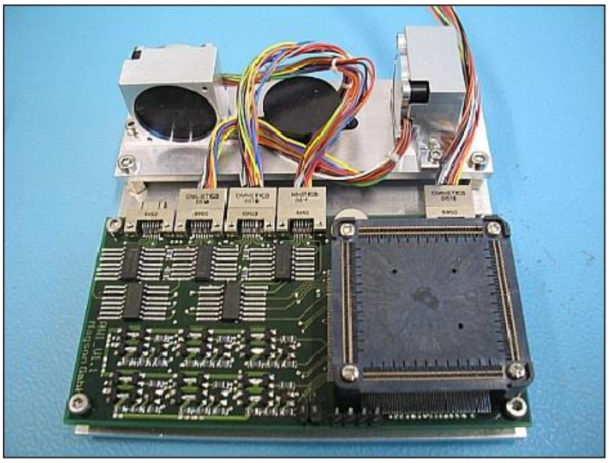

Figure 1.8: Engineering model of microwheel assembly [7]

The ADCS consists of 6 sun sensors, a HMC 1053 3-axis magnetometer, 3 gyros, 6 magnetic coils and 3 microwheels [7,30]. The overall rotational speed was stabilised at around 2°/s since deployment [8]. The microwheel system was tested periodically and it functioned as expected. Below, in figure 1.9, the variation in the wheel speed is shown. The standard deviation is 9.3 rpm [8].

BEESAT-2 was launched in April 2013. It will further test the reaction wheels and three axis attitude stabilisation.

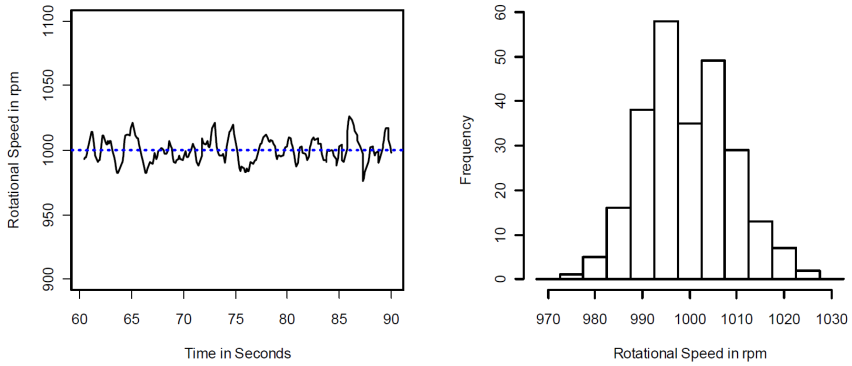

Figure 1.9: Typical rotational wheel speed variation [8]

1.3.3.5 BRITE

The BRIght Target Explorer (BRITE) is a mission which plans to use 6 nano-satellites to make photometric observation of some of the most luminous stars using a CCD imager with a 3-cm aperture telescope [9]. This mission aims to improve on ground-based stellar photometry which is impeded by the absorption of light by the atmosphere and the fact that measurements can only be made intermittently due to the stars setting below the horizon and the presence of sun- and moonlight [31]. The satellites use the Generic Nanosatellite Bus (GNB) which was developed by SFL and used for the first time on the AISSat-1 mission. The GNB is a 20 cm × 20 cm × 20cm cube shown in figure 1.10 with the BRITE telescope and star tracker in the payload bay.

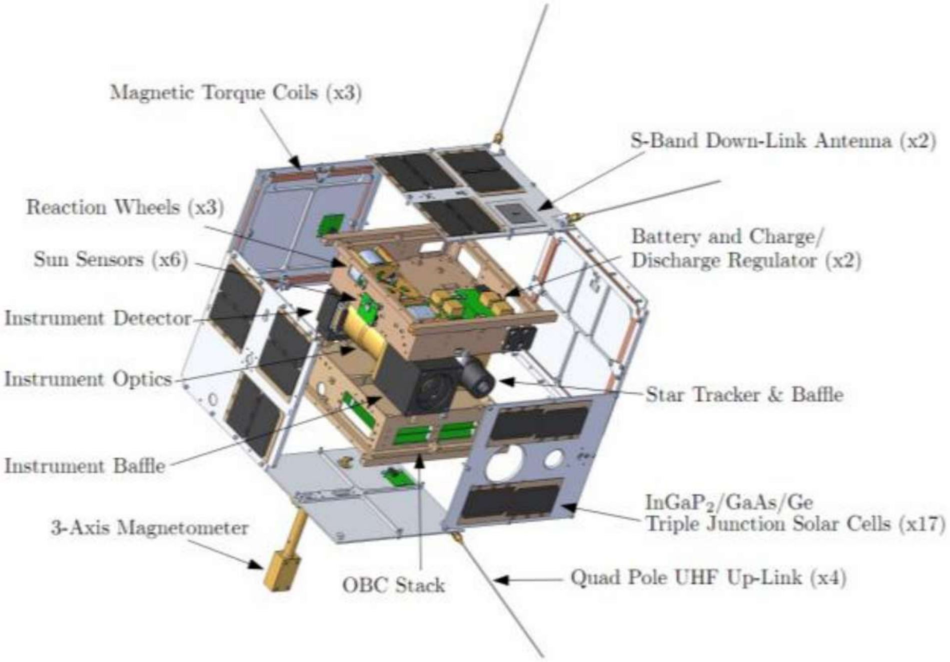
Magnetic Torque Coils (x3)
S-Band Down-Link Antenna (x2)
Reaction Wheels (x3)
Battery and Charge/
Discharge Regulator (x2)
Sun Sensors (x6)
Instrument Detector
Instrument Optics
Star Tracker & Baffle
Instrument Baffle
InGaP2/GaAs/Ge
Triple Junction Solar Cells (x17)
3-Axis Magnetometer
OBC Stack
Quad Pole UHF Up-Link (x4)

Figure 1.10: BRITE satellite [9]

In order to perform photometry, the BRITE satellites need to be stabilised to 1 arcminute or 0.0167 degrees. To meet these stringent requirements, star trackers and reaction wheels will be used. Star trackers used will include the ComTech Aero Astro Miniature Star Tracker (MST) and the Sinclair-SAIL-SFL Star Tracker (S3S). The Sinclair-SFL 30 mNms reaction wheels will be used.

Three BRITE satellites have been launched to date, including UniBRITE and BRITE-Austria, launched in February 2013, and BRITE-PL, launched in November 2013 [27].

1.3.4 Reaction Wheel Comparison

Reaction wheels are critical for an ADCS which attempts to perform three axis pointing control. Below is a summary of the reaction wheels currently commercially available or used in nano-satellites. Key parameters, namely the supply voltage required, the reaction wheel size and mass, the maximum torque and angular momentum the reaction wheel can deliver and its power consumption, is given.

Part	**Supply Voltage (V)**	**Size (mm)**	**Mass (g)**	**Torque (mNm)**	**Angular Momentum (mNms @ rpm)**	**Power (W @ rpm)**
RW 0.007-4	3.5 to 6	50×40×27	90	1	7 @ 4460	0.7 max 0.2 @ 4460 0.1 @ 2000
RW 0.01-4	3.5 to 6	50×50×30	120	1	10 @ 3410	0.7 max 0.16 @ 3410 0.1 @ 2000
RW 0.03-4	3.4 to 6	50×50×40	185	2	30 @ 5600	1.5 max 0.4 @ 6000 0.1 @ 2000
Micro-Wheel	5 to 15	43×43×18	150	0.6	18 @ 6000	1.0 max 0.1 nominal
RW 1 A	5	21×21×12 (WDE* 95×50×15)	20 (WDE* 45)	0.023	0.58 @ 8000 (max 16000)	0.72 max 0.62 @ 8000 0.4 Standby (WDE only)
RW 1 B	5	21×21×12 (WDE* 95×50×15)	12 (WDE* 45)	0.004	0.1 @ 8000 (max 16000)	0.72 max 0.62 @ 8000 0.4 Standby (WDE only)
Delfi-n3Xt	-	40×40×27	82	0.0055	1.6 @ unknown	0.53 to 0.71
IMI-101 (3 wheels)	12 to 28	76×76×70	640	0.635	1.1 @ unknown	4.32 max 2.4 typical

*Wheel Drive Electronics

Table 1.1: Reaction wheel comparison

The RW 0.007-4, RW 0.01-4 and RW 0.03-4 are manufactured by Sinclair Interplanetary. The Micro-Wheel system is from Blue Canyon Technologies. The RW 1 A and RW 1 B are variations of the reaction wheel flown on BEESAT, and is made by Astro und Feinwerktechnik Adlershof GmbH. The data on the reaction wheels flown on the Delfi-n3Xt mission is also given. The IMI-101 is a three reaction wheel system made by Maryland Aerospace.

1.4 Thesis Overview

This thesis firstly gives an overview of the theory relating to the ADCS of a satellite. The parameters of an orbit, coordinate frames used for describing satellite attitude, relevant aspects of the space environment and some types of attitude sensors and actuators are discussed in chapter 2.

Chapter 3 describes the ZACUBE-2 mission and its requirements. An overview of a complete ADCS is given as well as an overview of a sensor and actuator interface module, named CubeControl. The power consumption and mass of the system is then investigated. Chapter 4 continues to give a detailed description of the design of all the subsystems on the CubeControl module.

In chapter 5 the software design of the CubeControl module variant used on the QB50 mission satellites is given. Attention is given to the scheduling of the subroutines. The setup used for interfacing with the CubeControl module is discussed in chapter 6. The calibration of the magnetometer and test results of the reaction wheels are also discussed in this chapter. Chapter 7 concludes this thesis with a summary of the project and recommendations for further development.

Chapter 2

Satellite Control Theory

In this chapter a brief overview is given of orbital parameters and the coordinate frames used to define the satellite attitude. Some relevant aspects of the space environment will then be discussed. Lastly, an overview is given of some of the sensors and actuators used for ADCS.

2.1 Orbit

The orbit of a satellite can be defined by its orbital elements, namely the semimajor axis a, the eccentricity e, the inclination i, the longitude of ascending node Ω, the argument of periapsis ω_p, and the true anomaly v [32]. The orbital parameters will determine the length of the sun exposure, the magnetic field variation, the aerodynamic disturbances and the radiation exposure levels on the satellite.

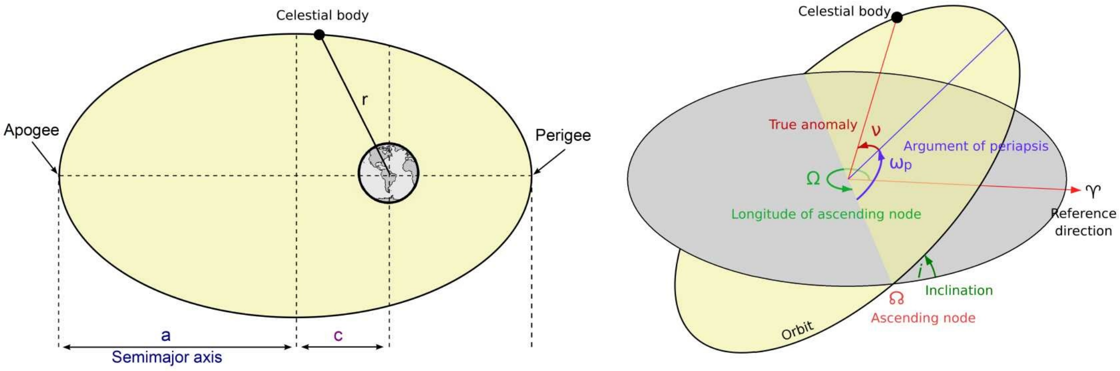
Celestial body
r
Apogee
Perigee
a
Semimajor axis
c
Celestial body
True anomaly
ν
Argument of periapsis
ωp
Ω
Longitude of ascending node
♈
Reference direction
i
Inclination
☊
Ascending node
Orbit

Figure 2.1: Orbital elements [10]

The equations governing the motion of a satellite in orbit are Newton's second law of motion, equation 2.1.1, and Newton's law of Universal gravity, equation 2.1.2, with m

the mass of the satellite, $\mu = GM$ the Earth's gravitational constant, and $\mathbf{r}$ the position vector of the satellite relative to the Earth's centre.

$$\vec{\mathbf{F}} = m \cdot \vec{\mathbf{a}} \tag{2.1.1}$$

$$\vec{\mathbf{F}} = \frac{-GMm}{r^2} \cdot \frac{\vec{\mathbf{r}}}{r} \tag{2.1.2}$$

From these two equations the two body equation of motion, 2.1.3, is obtained, assuming that gravity is the only force on the body, the Earth is spherically symmetric and the Earth has a much greater mass than the satellite body.

$$\ddot{\vec{\mathbf{r}}} + \frac{\mu}{r^3} \cdot \vec{\mathbf{r}} = \vec{\mathbf{0}} \tag{2.1.3}$$

A solution to the two-body equation of motion is the polar equation of a conic section [32]. All orbits are thus, with the assumptions made above, conic sections. Any non-escape orbit will be an eclipse with its eccentricity equating to c/a.

2.2 Coordinate Frames and Satellite Attitude

The attitude of a satellite can be described with relation to reference frames centred on the satellite's centre of mass. The three reference frames often used in ADCS are the orbit reference frame, the inertial reference frame and the body reference frame. The orbit reference frame is fixed to the orbit position with the X_O and Z_O axes within the orbital plane. The Z_O axis is always nadir pointing, and the Y_O axis points in the orbit anti-normal direction, completing the right hand set. The inertial reference frame is functionally fixed in inertial space. The X_I and Z_I axes are in the orbital plane with the Z_I axis pointing toward the orbit apogee. The Y_I axis points in the orbit anti-normal direction. The body reference frame is fixed to the spacecraft body and is usually chosen to coincide with the orbit reference frame when the satellite is in its normal attitude.

The attitude of the satellite can, for example, be described by three consecutive rotations that will transform the body reference frame to the orbit reference frame. These three angles, called the Euler angles, can also be used to deduce the Direction Cosine Matrix (DCM) or the Quaternions which are methods to represent the satellite attitude.

The dynamic behaviour for the satellite's attitude can be expressed by Euler dynamic equation of motion,

$$\mathbf{I}\dot{\vec{\omega}}^{B/I} = \vec{\mathbf{N}} - \vec{\omega}^{B/I} \times \left(\mathbf{I}\,\vec{\omega}^{B/I} + \vec{\mathbf{h}}\right) - \dot{\vec{\mathbf{h}}} \tag{2.2.1}$$

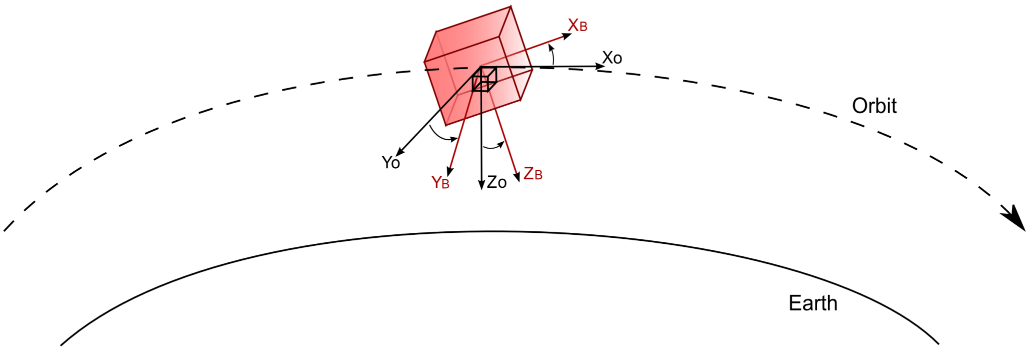

Figure 2.2: Body- and orbit reference frames

where **I** is the moment of inertia tensor, $\omega^{B/I}$ is the inertially referenced body angular rates, $\vec{\mathbf{N}}$ is the torques acting on the satellite and **h** is the angular momentum in the momentum exchange device [33]. The torques acting on the satellite includes the gravity gradient torque, magnetic torque and disturbance torques.

2.3 Space Environment

The satellite will experience solar radiation pressure disturbances and aerodynamic disturbances due to the earth's atmosphere. The satellite will also be under the influence of the geomagnetic field and space radiation.

2.3.1 Geomagnetic Field

The earth has a magnetic field surrounding it due to its active core. The intensity of the B-field is measured in Tesla (T) or Gauss (G), with 1 G = 100 μT. The magnetic field intensity varies between 20 μT and 65 μT as shown in figure 2.3.

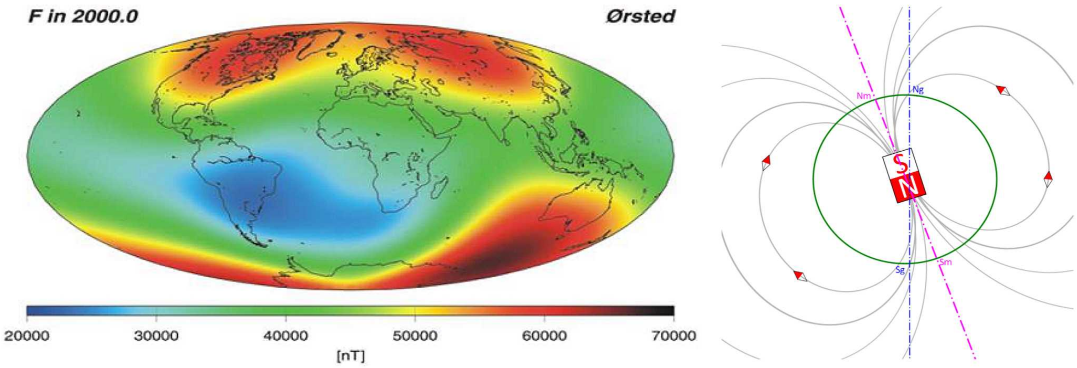

Figure 2.3: Geomagnetic field intensity and direction [9]

When determining the field strength at various altitudes the geomagnetic field can be approximated as a dipole at the earth's centre. The strength then scales from its value at the earth's surface with the factor $(R_e/r)^3$, so that, at an altitude of 10000 km ($r = R_e + 10000$ km), the strength drops to around 6% its strength on the earth's surface. The International Geomagnetic Reference Field (IGRF) provides a model for the expected geomagnetic field strength at any point in space.

2.3.2 Radiation

Space radiation can be divided into three types: particles that are trapped within the earth's magnetic field, such as the Van Allan belts; particles emitted by the sun during solar events; and galactic cosmic rays, which originate from outside our solar system [34]. There are two Van Allan belts. The outer belt extends from about 10000 km to 60000 km with the greatest intensity between 25500 km and 32000 km. The inner belt is generally between 1000 km and 6000 km although it can go down as low as 200 km at the South Atlantic Anomaly.

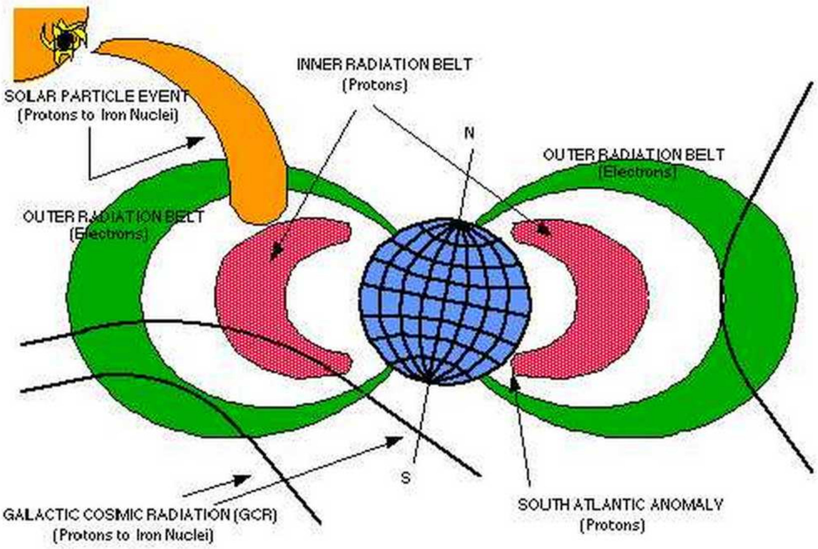
SOLAR PARTICLE EVENT
(Protons to Iron Nuclei)
INNER RADIATION BELT
(Protons)
N
OUTER RADIATION BELT
(Electrons)
OUTER RADIATION BELT
(Electrons)
S
GALACTIC COSMIC RADIATION (GCR)
(Protons to Iron Nuclei)
SOUTH ATLANTIC ANOMALY
(Protons)

Figure 2.4: The space radiation environment [11]

Radiation can cause errors in, or damage to electronic components, compromising the reliability of the system. The radiation effects can be categorized as total ionizing dose (TID) effects, which causes degradation of a component over a long time period, or single event effects (SEE), which is caused by the passage of a high energy particle through the active region of the device [35]. Two types of SEE's prevalent in COTS components are single event upsets (SEU), events which changes the data stored in memory, and single event latchups (SEL), which creates a regenerative forward bias in a CMOS p-n-p-n structure, effectively shorting the power to ground. SEL's can cause damage due to overheating if the device is not power-cycled immediately. Flash memory is susceptible to SEE's when being written to, while SRAM is susceptible to SEE's during both read and write operations [16].

2.4 Sensors

Various sensors can provide information regarding the attitude of a spacecraft, including star sensors, fine and coarse sun sensors, nadir sensors, magnetometers and rate sensors. Star sensors takes an image of the stars and matches it to an internal star catalogue, giving full 3-axis information. They are generally the most accurate attitude sensor. Fine sun sensors and nadir sensors determine the sun or nadir vector, each providing 2-axis information, using a camera and image processing. Coarse sun sensors use photodiodes which measures the light intensity on the different facets of the satellite to determine the sun vector.

2.4.1 Magnetometers

Magnetometers are used to measure the magnetic field vector relative to the satellite body coordinate frame. Using the IGFR model for the geomagnetic field, 2-axis attitude information can be deduced. As the model is not perfect the accuracy of this data is limited, generally to between 1^o and 5^o [32]. Magnetometers are generally only effective at altitudes lower than 6000 km due to residual spacecraft magnetic dipoles dominating the weakening geomagnetic field [32, 36].

A magnetometer is comprised of a magnetic sensor and an electronic unit that transforms the measurement into a usable format [37]. Various technologies can be used for a magnetic sensor. Fluxgate magnetometers have been established as a viable type of magnetic sensor for satellites, providing a good trade-off between accuracy, power consumption, size and weight [38]. Fluxgates consist of a piece of easily saturable ferrous material around which two coils are wound. An alternating current is passed through one coil, inducing current in the second coil which is measured. The ambient magnetic field will cause the core to be more easily saturated in one direction than the other, causing a mismatch in the input and output current. Fluxgate magnetometers are generally too heavy and require too much power for use in nano-satellites, although some fluxgate magnetometers have been deemed feasible for use on CubeSats [39].

Anisotropic Magnetoresistive (AMR) technology is another mature magnetometer type, which uses the change in the resistance of a conductor in the presence of a magnetic field. Honeywell uses AMR in their HMC series of COTS magnetometers. The AMR sensors are designed in a wheatstone bridge configuration with four magneto-resistive elements that will stay electrically identical if they are not subjected to a magnetic field [12], as shown in figure 2.5.

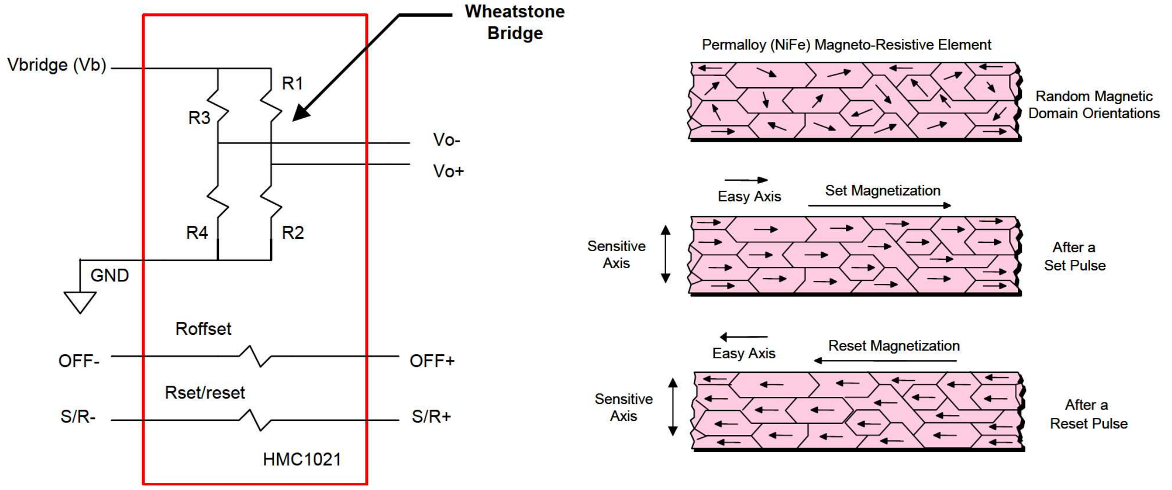
Wheatstone Bridge
Vbridge (Vb)
R1
R3
Vo-
Vo+
R4
R2
GND
Roffset
OFF-
OFF+
Rset/reset
S/R-
S/R+
HMC1021
Permalloy (NiFe) Magneto-Resistive Element
Random Magnetic Domain Orientations
Easy Axis
Set Magnetization
Sensitive Axis
After a Set Pulse
Easy Axis
Reset Magnetization
Sensitive Axis
After a Reset Pulse

Figure 2.5: Wheatstone bridge and magnetic orientations of Magnetoresistive element [12, 13]

When a magnetic field within the sensor operating range is applied to the sensor, the field will rotate the magnetic moment, causing a change in the resistance of the element. When the external field is removed the magnetic moments will return to their initial state. External magnetic fields outside the sensor operating range can however re-magnetize the sensor in an undesired orientation. To recover from this eventuality and to optimize the sensor for sensitivity and remove biases, set and reset pulses are used to magnetically restore the sensor. Figure 2.5 shows the magnetic orientations of a magneto-resistive element.

Giant Magneto-Resitance (GMR) sensors use a structure with two or more magnetic layers separated by a non-magnetic layer. Spin-dependent scattering of the conduction electrons causes the resistance to be at a maximum when the magnetic moments of the layers are antiparallel and minimum when they are parallel [38]. Spin Dependent Tunnelling (SDT) technology uses an insulating instead of the conductive layers used in GMR. Conduction between the magnetic layer is possible through quantum tunnelling through the insulator, which is also dependent on the relative magnetization of the two magnetic layers.

Another technology used in magnetometers is Magneto-Inductive (MI) sensors. The alternating current impedance of ferromagnetic materials is highly dependent on the bias magnetic field at high frequencies [40]. An example of a sensor which uses this technology is the MicroMag3 from PNI, which was flown on the RAX mission as mentioned in section 1.3.3.2.

2.4.2 Rate Gyroscopes

Satellite body angular rates relative to the inertial reference frame, $\vec{\omega}^{B/I}$, can be measured using three orthogonal gyroscopes. The extent to which angular rate sensors are useful for attitude control depends on their noise levels. While they can easily provide useful data when measuring high angular rates present in detumbling or slew manoeuvres, they require very low noise levels to be useful when the satellite is three-axis stabilized. Very accurate rate gyroscopes typically require too much power to be viable for use on CubeSats, but there are COTS Micro-Electro-Mechanical System (MEMS) rate gyroscopes with reduced accuracy which are suitable for CubeSats. A MEMS rate sensor consists of a micro-mechanical structure in which a vibration is established. The velocity of the resonator, when subjected to rotation about an axis perpendicular to that plane, generates a Coriolis acceleration, which is measured in order to deduce the angular rate [41]. MEMS-based angular rate sensors are low power, small in size, and low cost [42] making them ideal for use on nano-satellites.

2.5 Actuators

The attitude of a satellite can be controlled using actuators. Satellite actuators include magnetorquers, momentum exchange devices and thrusters, although thrusters are generally not viable for ADCS on CubeSats due to the limited available volume.

2.5.1 Magnetorquers

Electromagnets, known as torquer rods or magnetorquers, are used on spacecraft as an attitude actuator. The magnetorquers generate magnetic dipole moments, $\mathbf{M}$, which interacts with the earth's geomagnetic field, $\mathbf{B}$, to induce a torque acting on the satellite $\mathbf{N_m}$.

$$\mathbf{N_m} = \mathbf{M} \times \mathbf{B} \tag{2.5.1}$$

From equation 2.5.1 we can see that the direction of the torque cannot have a component in the direction of the geomagnetic field, limiting the control. The torques generated by magnetorquers are also small. They are, however, very reliable and have a long operational lifetime due to the fact that they have no moving parts and only require electrical power [33].

The two main types of magnetorquers are air core wire loops, which can be imbedded round the edges of a solar panel for example, and torquer rods, which use a ferromagnetic rod core around which a conductor is wound. The magnetic moment generated by magnetorquer is:

$$\mathbf{M} = \mu_t n I A \tag{2.5.2}$$

where the unit of $\mathbf{M}$ is Am^2, n is the number of windings, I is the current in the coil and A is the area enclosed by the coil. For torquer rods $\mu_t = 1.66 \times (\text{length/diameter})^{1.5}$ typically. For air core magnetorquers $\mu_t = 1$.

2.5.2 Momentum Exchange Devices

A momentum exchange device consists of a rotating mass of which the angular momentum is controlled. As the total angular momentum of the satellite stays constant when no external torques are applied, the satellite body will experience an equal and opposite change in angular momentum than the angular momentum change generated in the momentum exchange device. The three types of momentum exchange devices include reaction wheels, momentum wheels and control moment gyros (CMG).

Reaction wheels controls the speed of a flywheel with an electric motor. They can provide high torques necessary for pointing manoeuvres. For 3-axis pointing control, three orthogonal reaction wheels are required, although a forth can be added for redundancy as reaction wheels are susceptible to wear, having mechanical moving parts. Momentum build-up can occur in reaction wheels due to external disturbance torques in which case magnetorquers are needed to slowly reduce the momentum within the wheels. Momentum wheels are reaction wheels which operate at a momentum bias. They are used to provide the satellite with gyroscopic stiffness, which makes the satellite more immune to disturbance torques. CMGs use wheels spinning within gimbals. The axis of the flywheel's rotation can be changed by controlling the gimbals. CMGs are capable of producing higher torques than reaction wheels, but are more complex.

Chapter 3

Design Overview

In this chapter an overview of the ZACUBE-2 ADCS module is given. Firstly, the satellite mission and its requirements are discussed. The ADCS hardware necessary for the mission is then briefly described, followed by a look at the interaction between the components. The requirements of an additional actuator and sensor interface module are also discussed. Finally, consideration is given to the layout of the components within the 1-U allocated for the ADCS and to the power and mass of the system.

3.1 Mission Description

The satellite for which the ADCS module is designed is ZACUBE-2. The satellite's mission is to assist with the calibration of the radar antenna patterns of an antenna at the South African National Antarctic Program's SANAE base in Antarctica. The calibration payload will require that the satellite is in a low earth polar orbit and three-axis stabilised to within $\pm 5^\circ$. The secondary payload of the satellite will be a camera used for earth imaging. This payload will require a pointing accuracy of 1°.

The satellite will be a 3 kg, 3-U CubeSat, as shown in figure 3.1. The front 1-U will contain all the ADCS hardware. The rest of the satellite will contain the other subsystems and the payloads. The satellite will employ aerodynamic feathers which will passively stabilize the pitch and yaw angles of the satellite. Aerodynamic paddles will provide roll actuation. The final orbit of the satellite has not yet been determined, but it is assumed that it will be a 500 km, 9am/pm, sun-synchronous orbit.

The mission can be divided into four phases with regard to attitude control. Firstly, the satellite will be released from a P-POD deployer whereafter the paddles, feathers and magnetometer boom will be deployed. The satellite will then experience a random tumble. The second phase will be detumbling, in which the satellite is put into a stable

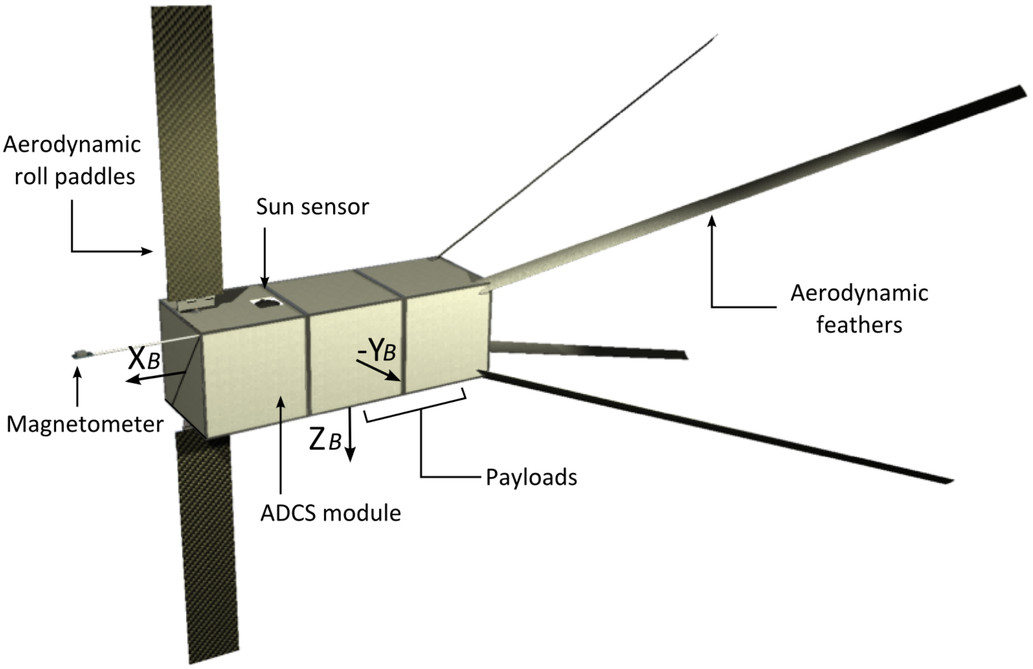

Figure 3.1: ZACUBE-2 satellite model

Y-Thomson spin using a B-dot and Y-spin controller. The Y-rate can then be brought to zero, either by using the same controller with a zero Y-spin reference, or by transferring the Y-axis momentum to a momentum wheel. The momentum wheel will then provide gyroscopic stiffness in the Y-axis for the following control modes. In the third stage, the satellite is controlled to be three-axis stabilized within ±5° with zero pitch, roll and yaw angles. Lastly, the satellite can be put into a pointing control mode when earth images are to be taken with the secondary payload camera. Different control algorithms were analysed by Auret [14] for each of the mentioned phases, and it was concluded that the desired accuracy could be achieved with the satellite design shown in figure 3.1.

3.2 Hardware Requirements

The ADCS must be able to execute the three control modes described in section 3.1, namely detumbling control, three axis stabilisation and pointing control. Magnetic control will be used in all control modes, either as the sole actuator or to desaturate reaction wheels. In order to implement magnetic control a magnetometer and three magnetorquers, mounted on the body axes of the satellite, are necessary. The magnetometer is mounted on a deployable boom in order to reduce noise from the satellite electronics. To achieve a pointing accuracy of 1° and in order to perform roll off-pointing during the pointing control mode, reaction wheels are required in all three axes.

The aerodynamic paddles shown in figure 3.1 will provide roll actuation by changing their rotation in the Z_B axis. The working of the aerodynamic paddles is explained in figure 3.2. By having the top and bottom paddle rotate in opposite directions, a roll torque will be generated by the aerodynamic pressure. The magnitude of the torque generated will be dependent on the angle of rotation. It will therefore be necessary to control the rotation angle of the paddles precisely. Using stepper motors is a simple low power solution for this problem, as the motor will retain its position when switched off.

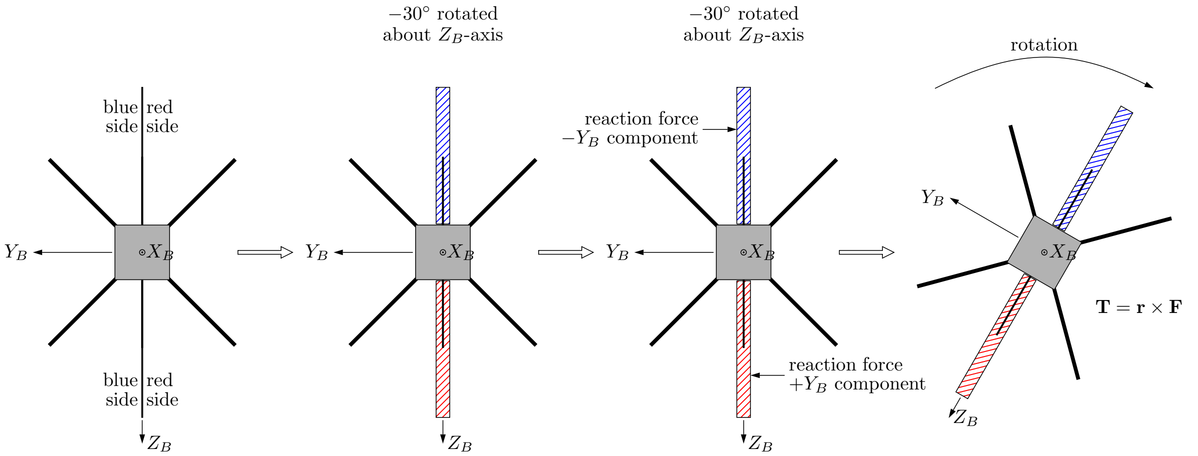
$-30°$ rotated about Z_B-axis
$-30°$ rotated about Z_B-axis
rotation
blue side
red side
reaction force $-Y_B$ component
Y_B
Y_B
$\odot X_B$
Y_B
$\odot X_B$
Y_B
$\odot X_B$
Y_B
$\odot X_B$
$\mathbf{T} = \mathbf{r} \times \mathbf{F}$
blue side
red side
reaction force $+Y_B$ component
Z_B
Z_B
Z_B
Z_B

normal position with largest surface area in $X_B Z_B$-plane

$+30°$ rotated about Z_B-axis

$+30°$ rotated about Z_B-axis

Satellite rotates about X_B-axis due to negative aerodynamic roll torque

Figure 3.2: Aerodynamic paddle roll actuation [14]

A nadir and fine sun sensor will be necessary to provide accurate attitude feedback. These sensors have a limited field-of-view (FOV). This can render them unusable for certain parts of the orbit, other than eclipse, if the satellite is not in a sun-synchronous orbit or if the satellite attitude is not controlled with the nadir sensor nadir pointing. A coarse sun sensor with a full spherical FOV, but reduced accuracy, can be used to ensure a sun vector is always available and to provide redundancy.

Angular rate sensors can also provide helpful data, especially during high angular rates present in detumbling or slew manoeuvres, in order to achieve better attitude and rate estimations.

A processor capable of running the control algorithms and orbital models is also needed. It must be able to receive all the sensor data, calculate and send the control signals and communicate with the satellite's main on-board computer (OBC).

As with all CubeSats, power, space and mass is limited. The entire ADCS module must fit within a 1-U, weigh less than 1 kg and use less than 1 W power.

3.3 ADCS Composition

The ADCS consists of three PC104 form factor modules. The interaction between these subsystems is shown diagrammatically in figure 3.3.

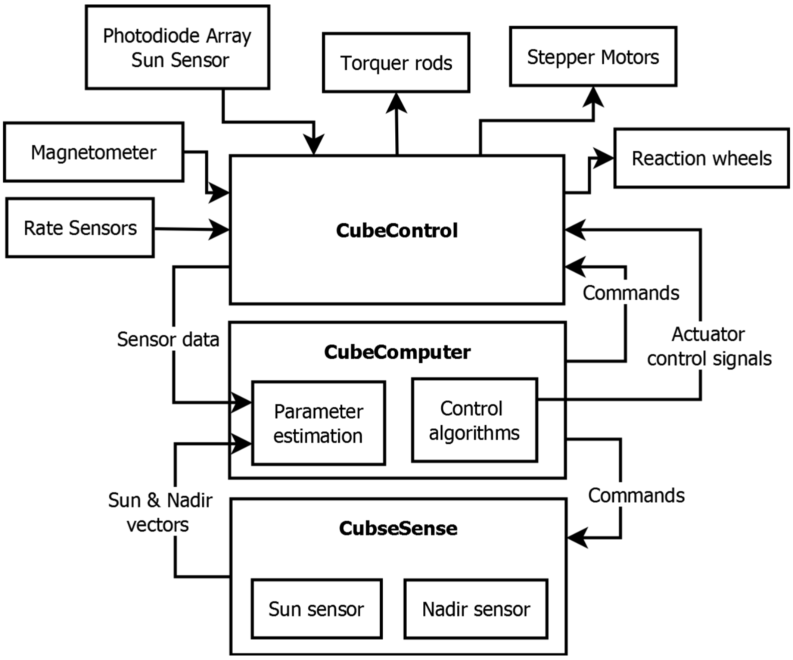
Photodiode Array Sun Sensor
Torquer rods
Stepper Motors
Magnetometer
Reaction wheels
Rate Sensors
CubeControl
Commands
Sensor data
Actuator control signals
CubeComputer
Parameter estimation
Control algorithms
Sun & Nadir vectors
Commands
CubseSense
Sun sensor
Nadir sensor

Figure 3.3: ADCS subsystems

CubeSense, the fine sun and nadir sensor, will be used to provide accurate attitude information. This module has two CMOS cameras. One will point in the positive Z_B direction and image the earth. An edge detection algorithm determines the horizon of the earth from which the nadir vector is calculated. The RMS error of the nadir sensor measurement is less than 0.1° when the full earth is in the FOV (about ± 30° roll/pitch from nadir in LEO). The RMS error of the measurements increase to 1° when the nadir vector moves to 60° from the boresight. The second camera points in the negative Z_B direction and images the sun. The sun vector is estimated with a RMS error of less than 0.3° over the full ±90° FOV ($<$ 0.1° over ±40° FOV). CubeSense uses $<$100 mW on average and 360 mW peak. The mass of CubeSense is 87 g.

CubeComputer is an on-board computer capable of running the ADCS algorithms. It features a high performance, low power 32-bit ARM Cortex-M3 based microcontroller which runs at 48 MHz at 1.25 DMIPS/MHz [16]. CubeComputer was designed with robustness in mind and protects against SEUs by implementing an EDAC module, and against SELs with a robust power system. The average power consumption of CubeComputer is 120 mW, and its mass is 65 g.

The third module, named CubeControl, will control all the actuators and additional sensors. The actuators include three reaction wheels, three magnetorquers and two stepper motors. The sensors include three rate sensors, a three-axis magnetometer and a photodiode array sun sensor. The design, manufacturing and testing of this module is the focus of this thesis.

3.4 CubeControl Module Overview

The sensor and actuator interface module is divided into two sections, each with its own microcontroller (MCU), in order to reduce the computational load. The one section, using a PIC18F47J13 MCU, implements speed control on the three reaction wheels. The other section, using a PIC18F45K22 MCU, controls the stepper motors and reads sensor data from the rate sensors, coarse sun sensor and photo-transistors. Both sections are able to control the torquer rods and read magnetomenter measurements. This makes magnetic control possible even if any one of the microcontrollers fails, providing redundancy for the most crucial attitude sensor and actuator.

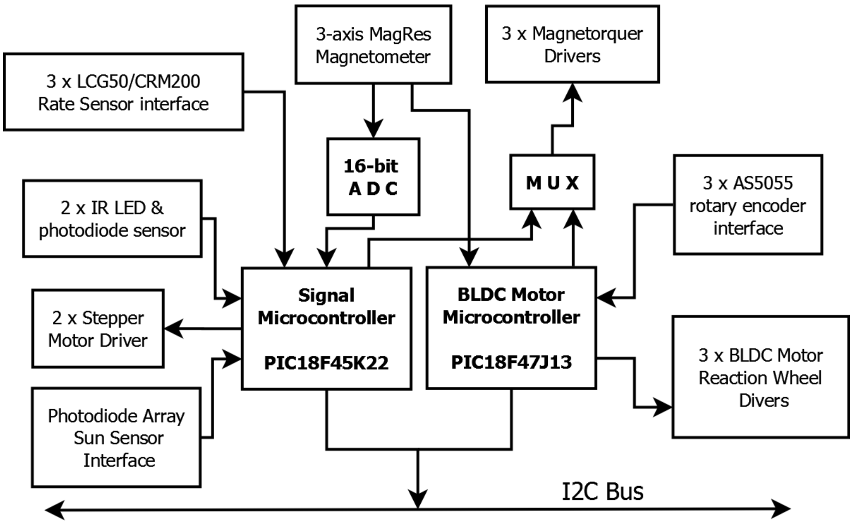
3-axis MagRes Magnetometer
3 x Magnetorquer Drivers
3 x LCG50/CRM200 Rate Sensor interface
16-bit ADC
MUX
3 x AS5055 rotary encoder interface
2 x IR LED & photodiode sensor
2 x Stepper Motor Driver
Signal Microcontroller PIC18F45K22
BLDC Motor Microcontroller PIC18F47J13
3 x BLDC Motor Reaction Wheel Divers
Photodiode Array Sun Sensor Interface
I2C Bus

Figure 3.4: CubeControl block diagram

The module communicates with CubeComputer, or any other device, via the main I2C bus on the PC104 header. The module also has an UART interface, which was used to communicate with a PC during testing. The board requires power sources of 3.3 V, 5 V and the standard battery voltage of a CubeSat, which is around 8 V. Power switches are used on all power lines, which allows the main OBC to power the device on or off in case of component failure. A brief summary of the final parameters of the sensors and actuators is given in the next section. The detailed design process is described in the next chapter.

3.4.1 Reaction Wheels

The reaction wheels offer high torque actuation. This enables faster and more accurate attitude control. A reaction wheel can also be used as a momentum wheel, which provide rigidity against disturbance torques.

The flywheel of the reaction wheel has an inertia of $I = 1.98 \times 10^{-6}$ kgm^2 around its axis of rotation. The material used is brass, which has a density of about 8390 kgm^{-3}. The mass of the flywheel is 21.6 g.

A FAULHABER Series 1509 006 B BLDC Micromotor was used. These motors are very power efficient and compact, making them highly suitable for this application. They are capable of delivering torques up to 0.52 mNm, although in the final design the torque was limited to 0.23 mNm to improve the control signal resolution. The motor has a mass of 6.9 g. The motor has a top speed of 11000 rpm, which gives the reaction wheel a maximum momentum storage of 2.28 mNms.

The mechanical drawings of the assembly of the reaction wheel are shown in Appendix A. Adding the mass of the reaction wheel mounting structure, the total mass of the reaction wheel is 45.5 g.

3.4.2 Magnetic Torquer Rods

Magnetorquers are electro-magnets which create a magnetic dipole in one axis. By controlling the current through three orthogonal magnetorquers, a torque can be generated orthogonal to the geomagnetic field. Two CubeTorquer torquer rods are used in the ADCS module. They have a nominal magnetic moment of ±0.2 Am^2 to ±0.24 Am^2 from 2.5 V supply. The mass of each torquer rod is 22 g. A magnetorquer coil with a magnetic moment of ±0.24 Am^2 will also be used to complete the 3-axis set.

3.4.3 Aerodynamic Paddles

AM0820 Stepper motors are used in combination with a 64:1 gearhead to control the angles of the aerodynamic paddles. The mass of each motor is 7.9 g. An infra-red LED and phototransistor will be used on each paddle to provide an indication of where the paddle is centred.

3.4.4 Magnetometer

An HMC1053 three-axis magnetometer is used to measure the earth's magnetic field. The geomagnetic vector is used to estimate the satellite attitude. It is also required to calculate the duty cycle of each torquer rod to produce the desired torque. The resolution of this sensor is 12 nT, and its power consumption is 64 mW.

3.4.5 Coarse Sun Sensor

A coarse sun sensor was developed using photodiodes. By measuring the light intensity from all facets of the satellite, the vector to the light source can be determined with a full spherical FOV. Its mass and power consumption are negligible.

3.4.6 Rate Sensors

Either LCG50 or CRM200 MEMS angular rate sensors will be used to provide the system with angular rate data. The RMS noise of the LCG50 is 0.018°/s. Its power consumption is 40 mW, its mass is 12 g and its dimensions are 29.4 mm × 29.4 mm × 11.7 mm. The noise of the CRM is 0.011°/s. Its power consumption is 16.5 mW and its size and mass are negligible.

3.5 Preliminary Structural Layout

Figure 3.5 shows a preliminary layout of the ADCS 1-U with all the major components.

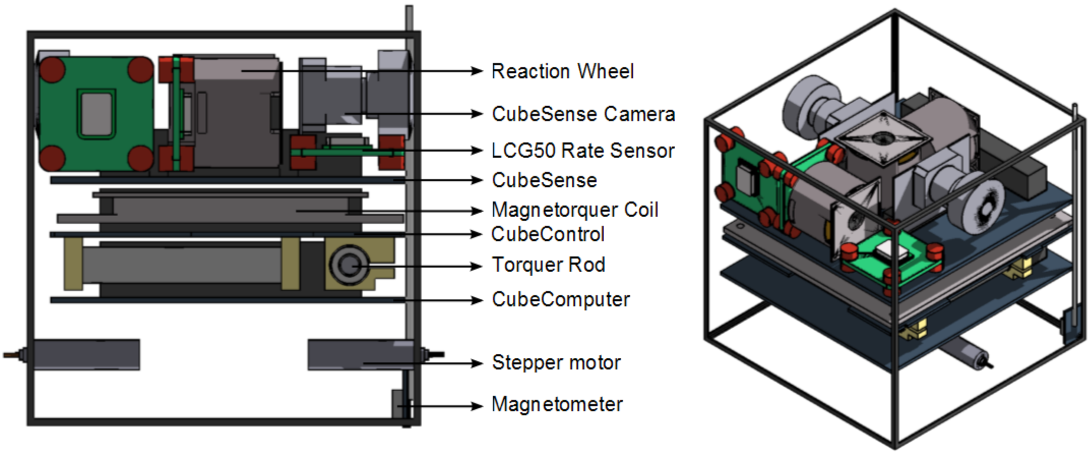
Reaction Wheel
CubeSense Camera
LCG50 Rate Sensor
CubeSense
Magnetorquer Coil
CubeControl
Torquer Rod
CubeComputer
Stepper motor
Magnetometer

Figure 3.5: ADCS layout

The top PC104 module, with the two cameras, is CubeSense. Between the two cameras are the three reaction wheels, each aligned to one of the principle body axes. The three LCG50 rate sensors (green PCBs) are also mounted orthogonally above CubeSense. Directly below CubeSense, the magnetorquer coil is stacked between the PC104 modules. Below the magnetorquer coil is CubeControl. The torquer rods are mounted to the bottom of the CubeControl module in a T-formation. Below CubeControl in the stack is CubeComputer. The rest of the 1-U can be used for the aerodynamic paddle deployment structure and stepper motors. The magnetometer, mounted on a deployable telescopic boom, is shown along the one edge of the 1-U. In this configuration the total height of the stack, excluding the magnetometer and stepper motors, is 65 mm, meeting the size constraint. The mounting brackets can only be manufactured when the design has been finalized.

3.6 Mass and Power Budget

The total mass of all the modules are listed in table 3.1. The total mass of the CubeControl module is 351 g and the mass of the entire ADCS module will be 503 g. Considering that the total mass for a 1-U is typically 1 kg and the volume of the ADCS module is 65 mm × 90 mm × 95 mm, the mass correlates with the restrictions of CubeSats.

Table 3.1: ADCS mass

Module	**Condition**	**Mass (g)**
CubeComputer		**65**
CubeSense		**87**
CubeControl		**350.8**
PCB		62
Reaction Wheels	3 RWs	136.5
Torquer rods	2 rods	54.6
Magnetorquer coil		67.6
Magnetometer		5.3
CSS		5.5
Stepper motors	2 motors	19.3
Total		**502.8**

The total power consumption of the modules are listed in table 3.2. The mean power is with both the MCUs and the reaction wheels powered on, but with zero actuation. The peak power is with all the actuators at their maximum power consumption. The total mean power consumption of the CubeControl module is 523 mW, and its peak power consumption is 2.58 W. The total mean power of the entire ADCS module is 753 mW.

Table 3.2: ADCS power consumption

Module	**Condition**	**Mean (mW)**	**Peak (mW)**
CubeComputer		**120**	**330**
CubeSense		**110**	**360**
CubeControl	MCUs and RWs on	**523**	**2580**
PIC18F45K22		40	-
PIC18F47J13		45	-
Magnetometer		33	-
IR LEDs		13.2	-
CRM200	3 rate sensors	49.5	-
Hall sensors	3 RWs	126	-
AS5055	3 RWs	49.5	-
L6235	3 RWs	135	-
Miscellaneous		32	-
Actuators		-	**2057**
Magnetorquers	2 rods, 1 coil	-	1400
Reaction wheels	3 RWs	-	528
Stepper motors	2 steppers on	-	130
Total		**753**	**3270**

Two similar ADCS modules, to which the designed module can be compared to, are the MAI-100 ADACS and the iADCS-100. Both modules are complete 3-axis ADCS which contain magnetorquers, a magnetometer, three reaction wheels and an ADCS computer. The parameters these modules are compared to that of the designed module, named CubeADCS, in table 3.3.

Table 3.3: ADCS parameter comparison

Parameter	**CubeADCS**	**MAI-100**	**iADCS-100**
Volume	556 cm^3	790 cm^3	274 cm^3
Mass	526 g	865 g	250 g
Typical power	0.753 W	2.4 W	0.5 W
Peak power	3.27 W	4.23 W	1.8 W
Momentum storage	2.28 mNms	1.1 mNms	1.5 mNms

We see that the volume, mass and power requirements of the CubeADCS module are within acceptable bounds, being less than the MAI-100, but more than the iADCS-100.

Chapter 4

Hardware Implementation

This chapter describes in detail the design of all the hardware components on the CubeControl module. The requirements of each of the subsystems are stated and all the integrated circuits and component design choices are discussed.

4.1 Reaction Wheels

The reaction wheel subsystem is comprised of a motor, flywheel, angular encoder, driving electronics and a mounting structure. The motor control signal is calculated by the microcontroller unit (MCU) and sent to the motor driver, which controls the motor torque. The motor speed is measured by the angular encoder and fed back to the MCU. The interaction between the components is shown in figure 4.1.

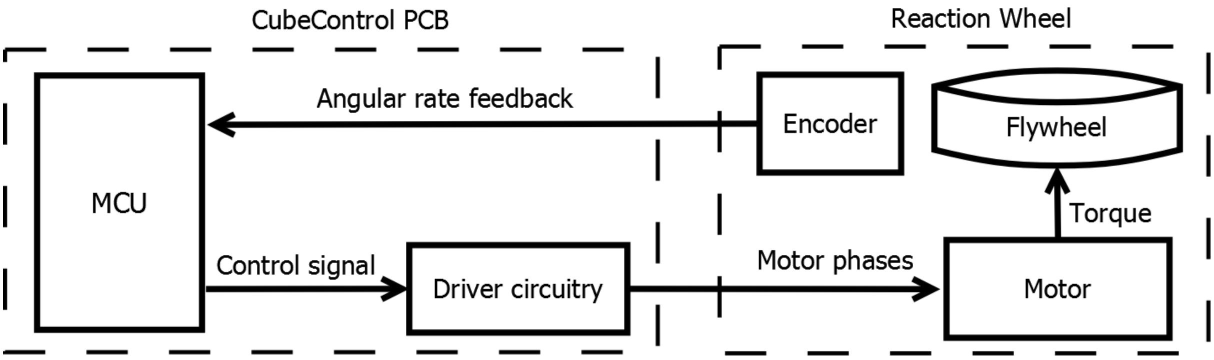
CubeControl PCB
Reaction Wheel
Angular rate feedback
Encoder
Flywheel
MCU
Torque
Control signal
Driver circuitry
Motor phases
Motor

Figure 4.1: Reaction wheel system

The key performance parameters of the reaction wheel are the following:

- The total momentum storage capability
- The torque capabilities of the motor

- The power consumption of the system
- The weight of the system
- The physical size of the system
- The accuracy to which the speed, or angular momentum, can be controlled

4.1.1 Motor

A motor used in space applications is required to have low mechanical wear to ensure a long operational lifetime and should have a high efficiency because of power limitations. Conventional DC motors suffer from disadvantages such as sparking and brush wear, especially in a low-pressure environment, which makes them unsuitable for use in space. Brushless direct current (BLDC) motors on the other hand have high efficiency, long life, high reliability and can function at high speeds [43], making them ideal for use in a reaction wheel.

Performance parameters of importance relating to the motor are its torque capability, maximum speed, supply voltage, efficiency and size. The maximum torque requirement, set by Auret [14], is 0.1 mNm. It is also desired to detumble a 3-U CubeSat from an angular rate of 5°/s with a single step command to the reaction wheel. Assuming the 3-U CubeSat has a mass of 3 kg, equally distributed, the largest moment of inertia will be 25×10^{-3} kgm^2. To detumble such a satellite from 5°/s a maximum angular momentum of 2.18 mNms is needed. For this requirement a maximum motor speed, with the flywheel described in section 4.1.2, of 10500 rpm is needed. The motor must also run from the CubeSat battery voltage, which is around 8 V.

Motors that meet these requirements include the FAULHABER 1509 006 B BLDC Micromotor, the EC 10 flat Maxon motor and the EC 14 flat Maxon motor. The EC 10 flat Maxon motor was not used because its efficiency was the lowest of the three motors. The FAULHABER Micromotor was chosen over the EC 14 flat Maxon motor because its total height was only 13.8 mm, compared to the 19.1 mm of the Maxon motor.

Another factor that must be taken into consideration is the shaft loads that the motor is capable of handling. At launch the satellite can experience forces up to 9 G. A flywheel with a mass of 21.6 g will generate a force of 1.9 N. The FAULHABER motor is rated for 2 N radial load at 3000 rpm and 15 N axial load at standstill, which is sufficient to withstand the vibrations during launch.

4.1.2 Flywheel

The total momentum storage of the reaction wheel is dependent on the motor speed and the inertia of the flywheel. Brass was used to manufacture the flywheel because of its high density. Brass is also non-magnetic, which means that it will not interfere with the rotary encoder, magnetometer or magnetorquers. A flywheel with an inertia of 1.98 kg mm^2 was designed, which produces an angular momentum of 2.28 mNm at 11000 rpm, meeting the satellite angular rate requirement of 2.18 mNms. The dimensions of the flywheel is shown in figure 4.2.

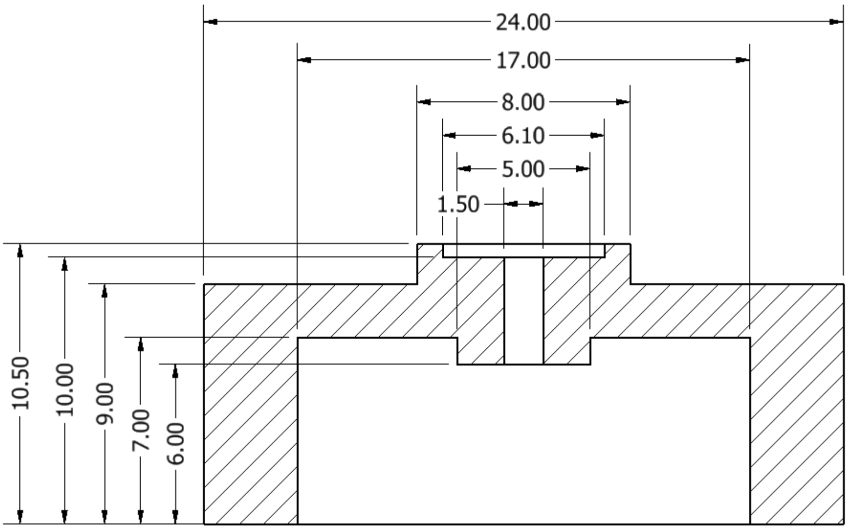

Figure 4.2: Flywheel dimensions (mm)

4.1.3 BLDC Motor Drivers

A three-phase BLDC motor requires a driver capable of handling the commutation of the phases, which is the switching of the correct motor phases based on the rotor position. One way to do this is to let the MCU sense the rotor position using the motor's Hall sensors, calculate which phases should be active, and switch external transistor bridges which drive the motor phases. This, however, requires a lot of pins on the MCU, a lot of computations by the MCU and a lot of space on the PCB. As three BLDC motors will be controlled, this option was not viable. Instead, the use of a dedicated BLDC control integrated circuit (IC) was investigated.

The use of a sensorless BLDC driver, like the Microchip MTD6501, was considered. A sensorless BLDC driver, however, requires the motor to run at a minimum speed in order to generate sufficient back-EMF to sense the rotor position. The reaction wheel will operate in both directions; therefore the motor cannot have a large dead-band at low speeds.

The L6235, a DMOS fully integrated three-phase motor driver, was chosen to drive the motors. The device includes all the circuitry needed to drive a three-phase BLDC motor including a three-phase DMOS bridge, a constant off time PWM current controller and the decoding logic for the Hall sensors that generates the required sequence for the power stage [44]. Using this integrated solution saves space on the PCB, which is very limited, and reduces the load on the microcontroller.

The MCU sends the L6235 a reference voltage which equates to a reference motor current. The actual motor current is measured by sensing the voltage drop, V_{sense}, over an external sense resistor through which the motor current flows. The motor current is then controlled to match the reference current. The bridge switches on when the voltage on the reference pin is larger than the voltage on the sense pin, and off otherwise. When the bridge is switched off the L6235 enters a "slow decay mode" for a set period of time, in which the current recirculates though the upper half of the bridge. The length of this "off-time" is set using an external resistor and capacitor, R_{off} and C_{off}.

Due to a "minimum on-time", for which the bridge must be switched on, the L6235 has a minimum torque, making it impossible to control the motor at low speed using a continuous analogue voltage reference. This problem is discussed in [45] and several solutions, such as increasing the "off-time", adding extra inductance to the motor phases and driving the IC with a PWM signal were investigated. It was found that using PWM to provide an average reference current produced the best results.

One problem with this technique is that the current is non-linear to the PWM duty-cycle due to the switching characteristics of the L6235, especially at low speeds. This caused the motor to be uncontrollable at very low speeds. To compensate for this a MATLAB simulation of the switching characteristics of the L6235 was written so that a transformation graph could be extracted to compensate for this non-linearity.

The values of R_{off} and C_{off} where changed to 20 kΩ and 470 pF respectively. This shortened the off-time, t_{off}, to 6.6μ s which reduced non-linearity and resulted in a switching frequency of 100 kHz.

The 3.3 V PWM control signal is voltage divided by a 270 kΩ and 27 kΩ resistor to 0.3 V. The PWM signal has a frequency of 2.7 kHz. The value of the sense resistor was chosen as 4.7 Ω. The maximum motor current and motor torque is thus:

$$\begin{aligned} I_{max} &= \frac{V_{sense}}{R_{sense}} \\ &= 3.3\ \text{V} \times \frac{27\ \text{k}\Omega}{270\ \text{k}\Omega + 27\ \text{k}\Omega} \times \frac{1}{4.7\ \Omega} \\ &= 63.8\ \text{mA}, \end{aligned} \tag{4.1.1}$$

and

$$\begin{aligned} N_{r(max)} &= I_{max} \times K_M \\ &= 63.8\ \text{mA} \times 3.64\ \text{mNm/A} \\ &= 0.232\ \text{mNm}, \end{aligned} \tag{4.1.2}$$

with V_{sense} the voltage on the L6235 sense pin and K_M the torque constant of the motor.

When a zero reference voltage was applied, the driver bridges occasionally switched on incorrectly on some L6235 drivers. This was attributed to an offset voltage on the driver sense comparator. To eliminate this, a 5.1 kΩ resistor was connected between 5 V and V_{sense}. This had the result of lifting the V_{sense} voltage with 4.6 mV which stopped the incorrect triggering of the bridge. The added power consumption is 4.9 mW. The typical quiescent supply current of the L6235 is 5 mA, which will result in a power consumption of 40 mW from a 8 V source.

4.1.4 Current Measurement

A measurement of the motor current can provide confirmation that the reaction wheel is functioning properly and can also indicate whether the friction of the motor changes during its lifetime. The measurement can be made using a non-inverting operational amplifier filter with its input connected through a 33 kΩ resistor to V_{sense}. The cut-off frequency of the circuit is:

$$\begin{aligned} f_c &= \frac{1}{2\pi RC} \\ &= \frac{1}{2\pi \cdot 33\ \text{k}\Omega \cdot 10\ \mu\text{F}} \\ &= 0.48\ \text{Hz}. \end{aligned} \tag{4.1.3}$$

This filter has a 95% settling time of 1 s, which coincides with the module control period as stated in section 5.3. The operational amplifier circuit gain is:

$$\begin{aligned} K &= 1 + (100\ \text{k}\Omega/33\ \text{k}\Omega) \\ &= 4.03, \end{aligned} \tag{4.1.4}$$

allowing for motor current measurements up to 174 mA, the maximum allowable motor current, on the 3.3 V MCU analogue-to-digital conversion (ADC) lines.

4.1.5 Angular Encoders

Accurate speed measurements are required for the controller to be able to run the motor at low speeds. A finer angular resolution will also mean that the controller will be able to run at higher sample rates, resulting in a faster transient response. The Hall sensors of the motor only provide 12 edges per revolution when multiplexed. This is insufficient for accurate and fast control as shown in [45].

The encoder is required to be small, low power and have a fine angular resolution. In the first prototype an AS5304 linear encoder from Austria Micro Systems was used in conjunction with a MR20-44 magnetic multipole ring. A magnetic ring was fitted to the flywheel of the motor, with the AS5304 mounted below. The AS5304 produces quadrature outputs. When the A and B signals are sent through an XOR gate the output signal has 80 pulses per pole pair. The MR20-44 has 22 pole pairs, which means the signal sent to the microcontroller has 1760 pulses per revolution (n_{ppr}). The MCU counts the number of pulses within a specified sampling time, T_s, giving a speed resolution of:

$$\begin{aligned}\Delta\omega &= \frac{1}{n_{ppr}T_s} \text{ rps} \\ &= \frac{1}{n_{ppr}T_s}\frac{60 \text{ s}}{1 \text{ min}} \text{ rps} \\ &= 0.341 \text{ rpm}\end{aligned} \tag{4.1.5}$$

for a 100 ms sampling time. The AS5304 can measure rotations of up to 13636 rpm, which is sufficient for the reaction wheel design. The quadrature A and B outputs are also passed through a d-type flip flop, the output of which will reflect the direction of the motor and is fed to the MCU. The AS5304 operates from a 5 V source, and the measured input current during operation is 18.5 mA. Although this design proved very effective at enabling accurate speed control with quick response times, the conclusion was that the 92.5 mW power consumption of the AS5304 was too high.

The AEDR-850x optical encoder from Avago Technologies was also considered. This encoder is very small (4 mm × 3.4 mm × 1 mm) and gives very accurate position readings. Unfortunately the power consumption of this encoder is 75 mW, which is also too high. Another encoder considered was the AEDR-8400. It is also capable of providing good accuracy position feedback and its power consumption is only 20 mW. However, due to a limited count frequency, the maximum motor speed this encoder can measure is only 3500 rpm, which is not sufficient.

The AS5055 Integrated Hall IC was the chosen encoder. It uses a diametrically magnetized disc to determine the rotor angle. It is capable of proving angular feedback with an accuracy of 1 degree. The power consumption of the AS5055 is only 1.65 mW for an angular readout rate of 10 ms. The encoder interfaces with the MCU via SPI. A disadvantage of this encoder is the fact that its magnet is stronger than the multipole ring used by the AS5304. Magnetic shielding will be necessary in order to prevent it from affecting other components such as the magnetometer, as is further discussed in section 4.1.7.

4.1.6 Mounting

When designing the mounting structure for the reaction wheel, consideration was given to the total size and weight of the system. The mounting should also be able to withstand the forces present during launch. There are two mounting parts: a bottom plate, to which the motor is attached and which is mounted on the satellite, and a top part, to which the encoder PCB is attached.

The bottom plate has ridges into which the motor snugly fits. These ridges provide support to the motor and increase the surface area for the space grade epoxy, which is used to attach the motor to the plate. A second ridge on the bottom plate serves the same function, but for the top part. The bottom plate also has four M2 holes for mounting the reaction wheel to the satellite. The top part is a cylindrical cap with three holes in the top for the centering of the encoder PCB and slits in the side for the wire routing.

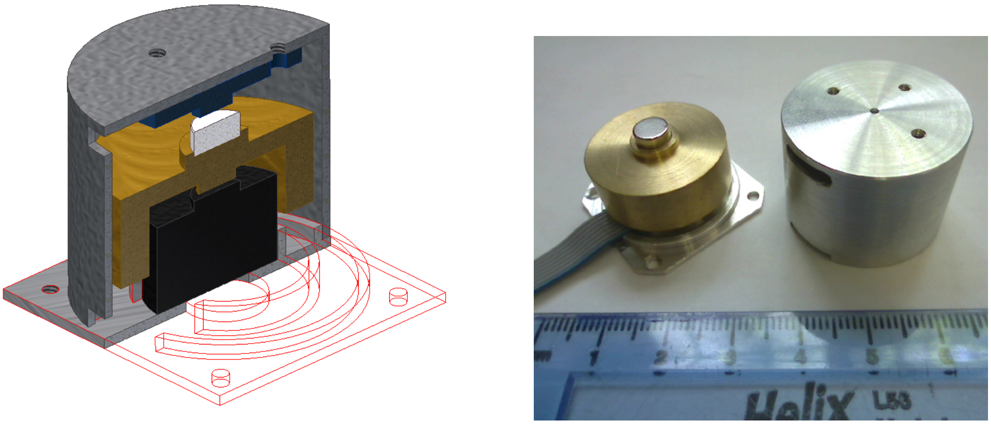

(a) Reaction wheel section view (b) Reaction wheel

Figure 4.3: Reaction wheel

4.1.7 Magnetic Shielding

In order to accurately measure the earth's magnetic field vector, the magnetic influence of the motors needs to be mitigated. This is achieved by deploying the magnetometer to increase the distance between the magnetometer and the motor, and by using a magnetic material to shield the motor.

Mu-metal is a material with high magnetic permeability, making it well suited for magnetic shielding. Considering the mounting of the motor, a few options for shielding were possible using a 0.1mm sheet of Mu-metal. Mu-metal can be fitted to the cylindrical cap along its inside and outside facets, and to the bottom plate on its bottom facet.

A magnetometer was used to measure the magnetic field disturbances when the distance between the magnetometer and the motor, with various amounts of shielding, was changed, in order to test the shielding efficiency. The largest deviation in the magnetic field occurs at low speeds. This is because at high speeds the filtering of the magnetometer reduces the high frequency noise. During testing the motor was run at 30 rpm to represent a worst case scenario. The standard deviation and bias of the magnetic field measurements are shown in figure 4.4 and figure 4.5 respectively.

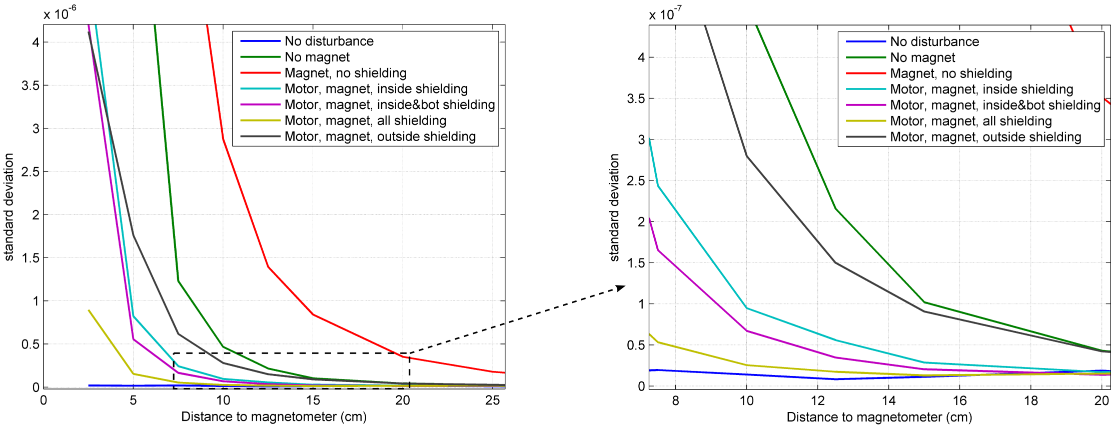

Figure 4.4: Magnetic field standard deviation (Tesla)

From figure 4.4 we can clearly see the significant effect the distance between the magnetometer and the motor has on the noise level. If we compare the standard deviation of the motor without the encoder magnet with that of the motor with the encoder magnet, we see that the magnet does have a considerable effect. When any shielding is added the noise drops substantially. The most effective shielding was achieved when shielding was added to all the facets mentioned previously, which resulted in very low noise levels, even at very close distances. The second most effective shielding was achieved with shielding placed on the inside of the cylindrical cap and on the bottom plate. Shielding on only the outside facets of the cylindrical cap was the least effective.

The effect of the noise can further be reduced by filtering. A bias shift, however, cannot be mitigated. Figure 4.5 shows the shift of the mean value of a 100 samples for the same

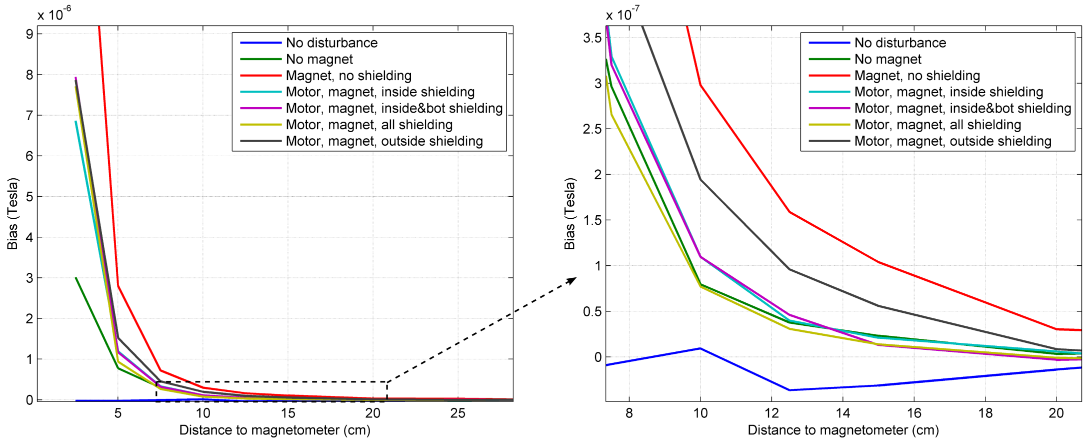

Figure 4.5: Magnetic field bias

experiment. From figure 4.5 we can see that the bias is less dependent on the type of shielding than the standard deviation.

The choice of which shielding to use dependents on how far the magnetometer can be deployed from the motors, and how important low noise on the magnetic field readings are, considering the added complexity to the manufacturing of the wheels and shielding. The suggested distance is a minimum of 12 cm and only the shielding on the inside of the cylindrical cap is to be used.

4.1.8 Momentum Wheel

The hardware of the reaction wheel can, with a few changes, also be used to drive a momentum wheel. As a momentum wheel does not operate at low speeds or with fast transients, the angular encoder might not be necessary. In such a case a motor speed measurement can be acquired using a SN74LVC1G386 3-input positive-XOR gate through which the Hall sensor outputs are fed. A 100 kΩ resistor and 180 kΩ resistor is used to voltage divide the 5 V to 3.21 V, well above the MCU Output High Voltage, V_{OH}. When counting the total edges in a 1 s control period, a speed resolution of 10 rpm can be deduced.

The DeOrbitSail mission requires a large momentum wheel to stabilize the satellite. For this momentum wheel a FAULHABER 2610 006 B BLDC Micromotor was used. The angular encoder was not necessary and only the Hall sensor outputs was used as described above. A flywheel with an inertia of 47.3 kg mm^2 is used, which produces an angular momentum of 34.6 mNms at 7000 rpm. The sense resistor value is changed to 1.3 Ω, increasing the maximum current to 231 mA. The motor has a torque constant of 9.05 mNm/A resulting in a maximum torque of 2.09 mNm.

The QB50 mission also requires a single momentum wheel. For this momentum wheel the smaller motor and flywheel is used and only the Hall sensor outputs are used for angular feedback.

4.1.9 Final Parameters

The final parameters and power usage of the reaction wheel are summarized in the table 4.1 and table 4.2 below.

Table 4.1: Reaction wheel parameters

Parameter	**Condition**	**Value**	**Unit**
Performance			
Small wheel			
Small Flywheel inertia		1.98	kg mm^2
Maximum speed		11000	rpm
Momentum storage	@11000 rpm	2.28	mNms
Torque		0.23	mNm
Large wheel			
Large Flywheel inertia		47.3	kg mm^2
Maximum speed		7000	rpm
Momentum storage	@7000 rpm	34.6	mNms
Torque		2.09	mNm
Physical			
Small wheel			
Height		22.5	mm
Width		28	mm
Motor		6.9	g
Small Flywheel		21.6	g
Mounting		8	g
Shielding		6	g
Encoder and cable		3	g
Total mass		45.5	g

Table 4.2: Reaction wheel power usage

Parameter	**Voltage (V)**	**Current (mA)**	**Power (mW)**
Small wheel			
Hall sensors	5	8.3	42
AS5055	3.3	<5	<16.5
L6235	8	5.6	45
Motor (@ 500 rpm)	8	3	24
Motor (@ 1000 rpm)	8	5.4	43
Motor (@ 2000 rpm)	8	9.1	73
Motor (@ 4000 rpm)	8	13.9	111
Motor (@ 8000 rpm)	8	19.5	156
Motor Peak power	8	22	176

4.2 Magnetorquers

In order to utilize magnetorquers, the direction and magnitude of the current through the magnetorquers need to be controlled. The implementation of the magnetorquers where done similarly to Mey [18]. For each magnetorquer, two output pins from the MCU are used to control a H-bridge. The output terminals of the H-bridge are connected to the terminals of the magnetorquer, allowing the current to flow in both directions. The connections are show in figure 4.6. The control signals from the MCU are applied through NAND gates with a PWM signal. By default both terminal signals will be low, causing both inputs of the H-bridge to be high, regardless of the value of the PWM signal. This will cause the H-bridge to turn on the bottom transistors to put the H-bridge in a slow decay mode, in which case the magnetorquer's current will drop to zero. When one magnetorquer terminal control signal from the MCU is set high the PWM signal will switch the bridge on and off and its duty cycle will scale the average current of the magnetorquer to the desired value. Due to the fact that two MCUs are used, it became possible to add redundancy to the magnetorquers by giving both microcontrollers the ability to drive the magnetorquers, making magnetic control possible even if one of the microcontrollers fails. This can be done using multiplexers on all the control lines. The select line can be controlled by the OBC, or automatically by connecting the control line to the power line of a specific MCU with a pulldown resistor. The control will then be executed by the selected MCU by default when the specific MCU is switched on, but in case of failure of one MCU, control will switch to the other MCU.

Two A3901 H-bridges and two SN74HC132 NAND gates were used, similar to that proposed by Mey. Two A74AC11257 were used to multiplex the signals from the MCUs. The

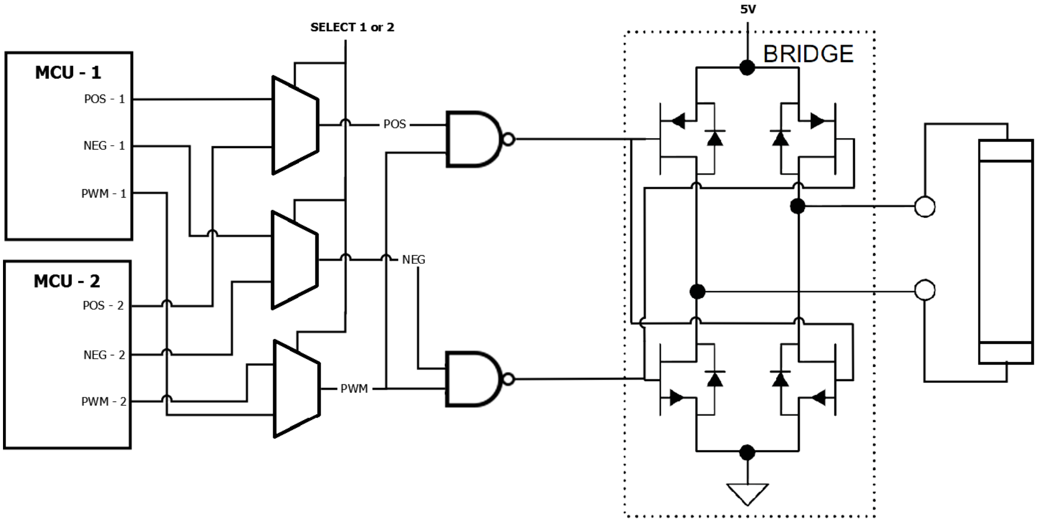

Figure 4.6: Magnetorquer implementation

select line of the multiplexer was routed to the main PC104 header, allowing the OBC to select which MCU is in control of the torquer rods. The current of all the magnetorquers are measured using an INA139 current shunt monitor with a sense resistor of 0.2 Ω and a load resistor 51 kΩ, allowing current measurements of up to 323 mA. A 1 μF is used in parallel with the load resistor to filter the measurement with a cutoff frequency of 3 Hz. This current measurement can be used to compensate for variance in the magnetorquer resistance due to temperature changes.

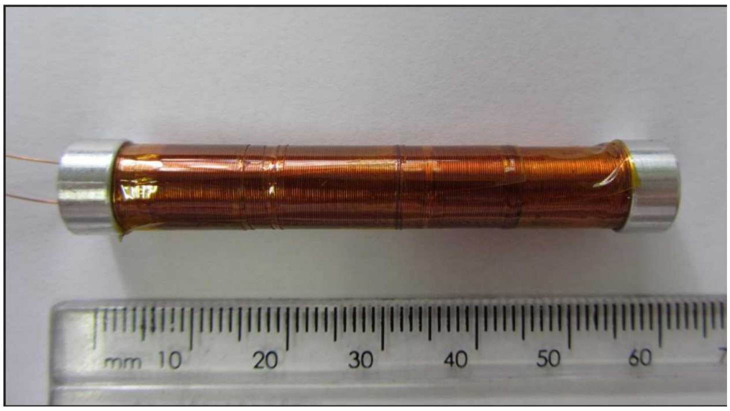

Figure 4.7: CubeTorquer

The torquer rod which will be used is CubeTorquer, designed at the ESL at Stellenbosch University. This torquer rod has a resistance of 30±1 Ω, a nominal magnetic moment of 0.2 Am^2 and a magnetic gain constant of 2.9024 Am^2/A. From this we can find the torquer current with no PWM scaling,

$$\begin{aligned} I_{unscaled} &= \frac{5 \text{ V}}{30.5} \\ &= 163.9 \text{ mA}, \end{aligned} \tag{4.2.1}$$

the required current for a magnetic moment of 0.2 Am^2,

$$\begin{aligned} I_{required} &= \frac{0.2}{2.9024} \\ &= 68.91 \text{ mA}, \end{aligned} \tag{4.2.2}$$

the duty cycle of the PWM to scale the current to the required value,

$$\begin{aligned} PWM_{scale} &= \frac{I_{required}}{I_{unscaled}} \\ &= 42.04\%, \end{aligned} \tag{4.2.3}$$

and the power consumption when the torquer is on,

$$\begin{aligned} P_t &= 5 \text{ V} \times 68.91 \text{ mA} \\ &= 344.6 \text{ mW}. \end{aligned} \tag{4.2.4}$$

Torquer rods can only be mounted in certain configurations as to not let their magnetic fields influence each other. In order to use the minimum amount of space within the 1-U, two CubeTorquer rods will be mounted on CubeControl in a T-formation. The third magnetorquer will be an air coil magnetorquer. This magnetorquer will require a separate structure. A prototype was designed and manufactured and is shown in figure 4.8.

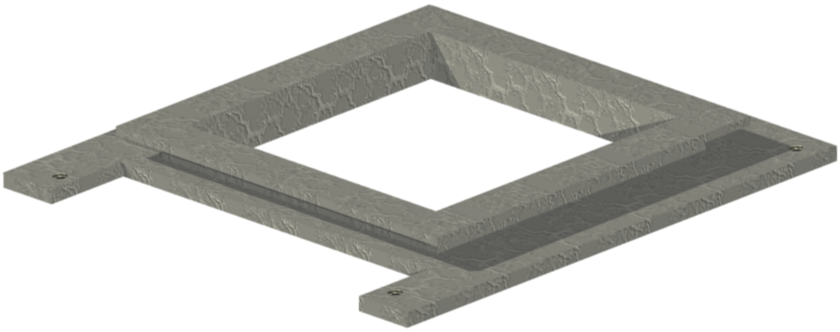

Figure 4.8: Air coil magnetorquer structure prototype

The magnetic moment of an air coil magnetorquer is

$$M = nIA. \tag{4.2.5}$$

For a square area A enclosed by the coil, a $5V$ supply voltage and a wire with a resistance of 0.67Ω per meter the current through the coil is

$$\begin{aligned} I &= \frac{V}{R_{\Omega/m} l} \\ &= \frac{5}{0.67\frac{\Omega}{m} \times n \times 4\sqrt{A}} \\ &= \frac{1.86}{n\sqrt{A}}. \end{aligned} \tag{4.2.6}$$

Now M becomes,

$$\begin{aligned} M &= nIA \\ M &= n \times \frac{1.86}{n\sqrt{A}} \times A \\ M &= 1.86\sqrt{A}. \end{aligned} \tag{4.2.7}$$

We see that the magnetic moment of the coil is only dependent on the area when the voltage stays constant. More coils will increase the resistance and reduce the power ($P = \frac{V^2}{R}$), making the coil more efficient. The maximum area achieved in the prototype is $0.042m^2$, resulting in a magnetic moment of $0.12Am^2$. For a 400 turn coil the resistance will be:

$$\begin{aligned} R &= 0.065 \text{ m} \times 4n \times 0.67\Omega/\text{ m} \\ R &= 69.7\Omega \end{aligned} \tag{4.2.8}$$

A coil with a magnetic moment of 0.24 Am^2 can be made using two coils in parallel. A magnetorquer was manufactured with two 400 turn coils, the maximum the structure could fit. The power consumption of this coil is 710 mW. Below is a table summarizing the parameters of the magnetorquers.

Table 4.3: Magnetorquer parameters

Parameter	**Condition**	**Value**	**Unit**
CubeTorquer			
Magnetic moment		0.2	Am^2
Power		344.5	mW
Mass		22	g
Mounting brackets mass	For 1 torquer	5.3	g
Length		60	mm
Diameter		10	mm
Magnetorquer Coil			
Magnetic moment		0.24	Am^2
Power		710	mW
Mass		67.6	g
Height		6.2	mm
Area		95 × 90	mm^2

4.3 Rate Sensor

The rate sensors are required to be small, low power and accurate. Two micro-electro-mechanical system (MEMS) rate sensors were analysed, namely the LCG50-100 and the CRM200. Throughout this section a sample rate of 10 Hz was used for both sensors.

4.3.1 LCG50-100

The LCG50-100 has an output noise (DC to 100 Hz) rated at $0.005°/\text{s}/\sqrt{\text{Hz}}$. Its power consumption is less than 40 mW. The dimensions of the module are 29.4 mm × 29.4 mm × 11.7 mm and it must be mounted on a separate structure from the CubeControl PCB. The angular rate output of this sensor is an analogue signal with a 2.5 V bias and a 16 mV/°/s (±15%) scale factor. The sensor also provides a temperature output. In order to get the maximum accuracy from the sensor, the outputs of the sensor are filtered with an analogue operational amplifier circuit and then sampled with the use of a 16-bit ADC external to the MCU, as shown in figure 4.9. The ADC then relays the measurements to the MCU via I2C. The use of this external ADC reduces the number of MCU pins required as multiple ADC's can communicate on the same I2C bus, allowing the MCU to sample more analogue signals.

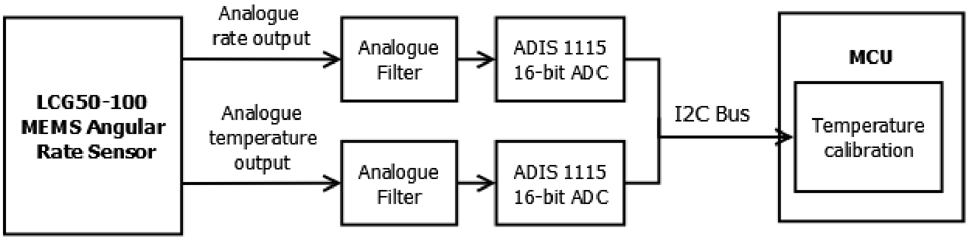

Figure 4.9: LCG50 supporting circuitry

4.3.1.1 Analogue filter design

The design of the filter went through two iterations. Initially a first order inverting low pass filter with a 2.5 V bias was used to scale the rate output to the desired range and reduce high frequency noise. The temperature output was filtered using a non-inverting operational amplifier circuit. Satellites rarely have initial angular velocities larger than 25°/s. The filter was designed to be able to measure angular rates, ω, of ±25°/s for the worst case scale factor, $K_{scale} = 18.4$ mV/°/s, and voltage range, $V_{range} = \pm 2.3$ V.

The first operational amplifier filter design used is shown in figure 4.10.

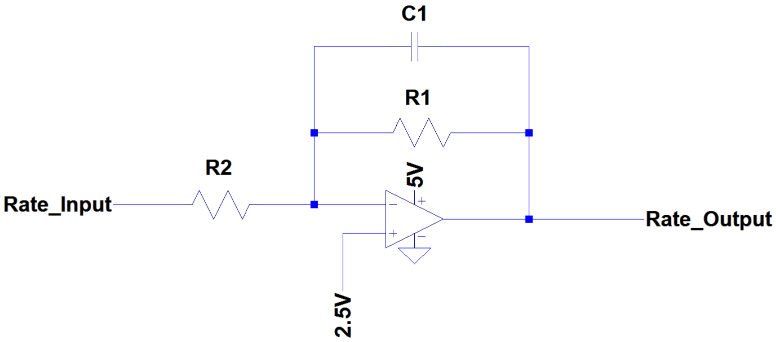

Figure 4.10: First order inverting low pass filter

The output voltage scale factor, K_{rate}, is,

$$\begin{aligned} K_{rate} &= V_{range}/\omega \\ &= 92 \text{ mV}/°/\text{s} \end{aligned} \tag{4.3.1}$$

and the filter gain, K_f, becomes

$$\begin{aligned} K_f &= K_{rate}/K_{scale} \\ &= 5. \end{aligned} \tag{4.3.2}$$

The resistance of R_1 is chosen as $270k\Omega$. The gain of the filter is defined as

$$K_f = \frac{R_1}{R_2} \tag{4.3.3}$$

resulting in the R_2 resistor minimum value

$$\begin{aligned} R_2 &= \frac{270000}{5} \\ &= 54000 \ \Omega. \end{aligned} \tag{4.3.4}$$

The resistance of R_2 is chosen as 68 kΩ. In order to reduce the high frequency noise, the filter was designed to have a cut-off frequency of 5 Hz, which would allow sampling at 10 Hz without aliasing according to the Nyquist theorem. The cut-off frequency is defined as:

$$\begin{aligned} f_c &= \frac{1}{2\pi R_1 C_1} \\ \therefore C_1 &= \frac{1}{2\pi \cdot 270 \text{ k}\Omega \cdot 5 \text{ Hz}} \\ &= 118 \text{ nF}. \end{aligned} \tag{4.3.5}$$

The value of C_1 was chosen as 150 nF resulting in a 3.9 Hz cut-off frequency.

Figure 4.11a shows the filtered rate measurements taken from the sensor when stationary. There appears to be a low frequency (<0.1 Hz) oscillation with a peak to peak value of 6°/s. Changing the sample period of the measurements had the effect of changing the apparent frequency of the noise. From this it was deduced that this oscillation was caused by aliasing, and that the noise was at a specific high frequency. The datasheet mentions that there may exist a narrow-bandwidth tone in the region of 340 Hz under certain conditions. In order to eliminate this high frequency noise another first order low pass filter was added in series to increase the roll-off. Figure 4.11b shows the rate measurements filtered with two first order filters. It can be seen the oscillation is no longer present and the peak-to-peak value of the noise is reduced to about 0.15°/s.

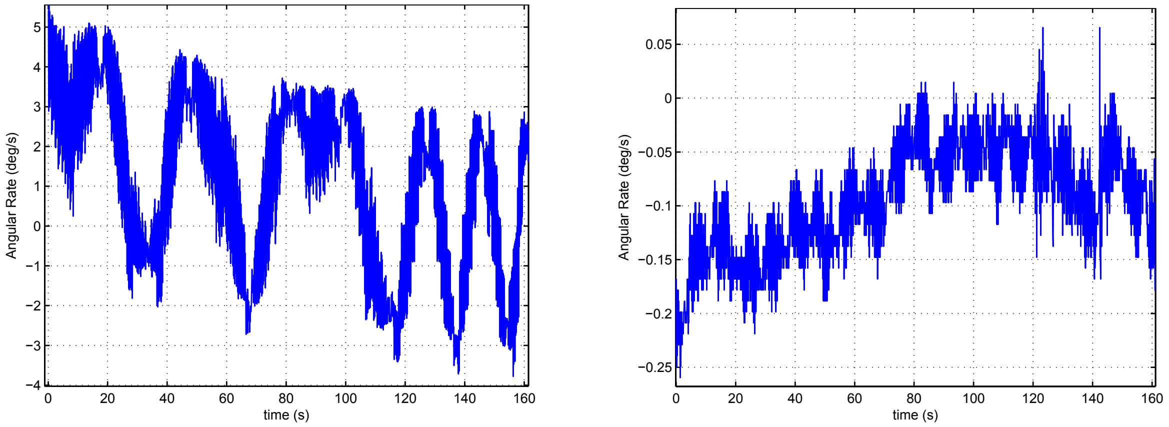

(a) One 1st order filter

(b) Two 1st order filters

Figure 4.11: Filtered angular rate measurements (note difference in scale)

Using two operational amplifiers requires extra space on the PCB. Instead of using two first order filters in series, a 2nd order multiple feedback (MFB) filter was used in the second iteration of the filter. The MFB architecture was chosen above the Sallen-Key architecture because it is less sensitive to component variations and has a superior high frequency response [46]. The topology is shown in figure 4.12.

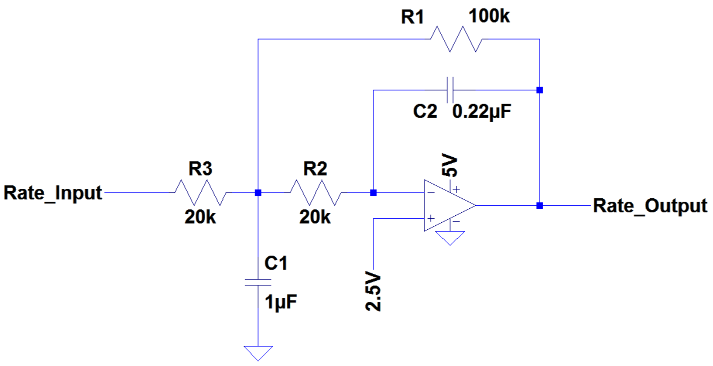

Figure 4.12: MFB filter

The gain of the filter must be at least 5 to allow the measurement of angular rates up to 30°/s, and the cut-off frequency is required to be close to 5 Hz. The cut-off frequency, f_c, and gain, K_f, of a MFB filter is defined as:

$$f_c = \frac{1}{2\pi\sqrt{R_1 R_2 C_1 C_2}} \tag{4.3.6}$$

$$K_f = \frac{R_1}{R_3}. \tag{4.3.7}$$

The components where limited by the available capacitor values. The values for C_1 and C_2 where chosen as $1uF$ and $0.22uF$ respectively. Choosing R_3 equal to R_2 was another design choice to simplify the design. From equations 4.3.6 and 4.3.7, R_1 was calculated to be 100 kΩ and both R_2 and R_3 to be 20 $k\Omega$. This results in a cut-off frequency of 7.6 Hz. The result of this filter can be seen in figure 4.17a.

4.3.1.2 Temperature Output

The rate sensor measurement is influenced by the sensor temperature. It is therefore important to know the sensor temperature in order to remove the sensor drift caused by the variation in sensor temperature.

The temperature output was scaled using a non-inverting operational amplifier filter. The resistors for this operational amplifier circuit was chosen as 100 kΩ and 20 kΩ for a gain of 6. With a temperature scale factor of 6.25 mV/°C and an output voltage of 424 mV at 0°C, this relates to a measurable temperature range from −68°C to 65°C from 0 V to 5 V.

4.3.2 CRM200

The output noise of the CRM200 is rated at $0.018°/\text{s}/\sqrt{\text{Hz}}$. Its power consumption is 16.5 mW. The module comes in a surface mount package with dimensions of 6.3 mm × 5.5 mm × 2.7 mm. The sensor can be configured as an SPI slave, allowing its rate and temperature measurements to be transmitted digitally to the MCU. The MCU can then use a simple digital filter to reduce high frequency noise. A higher order filter can be implemented on the main OBC to reduce computation time on the CubeControl MCU.

4.3.2.1 Digital filter design

The noise of the CRM200 is non-gaussian with interesting properties. Figure 4.14a shows the raw sensor data when a 0.1° /s angular rate step occurs at 211 s. This was done using

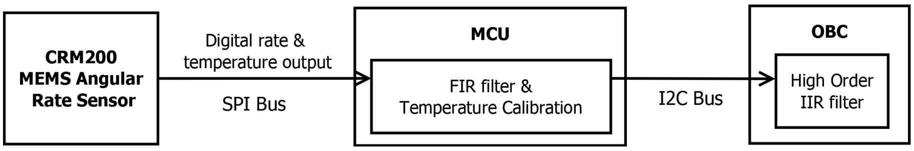

Figure 4.13: CRM filtering

an Ideal Aerosmith 1270 VS Rate table, which has 0.1% accuracy. The regularity of certain measurements (0.665 and 0.84) is much higher than other values. The actual rate does however seem to be the average of the measured values. The following FIR filter was implemented on the MCU,

$$y(n) = \sum_{k=0}^{9} 0.1x(n-k) \tag{4.3.8}$$

with $x(n)$, the raw rate sensor measurement, sampled at 100 Hz. A 10 Hz output rate can then be achieved by only calculating every tenth filtered output, $y(n)$, greatly reducing computation time on the MCU. The filtered signal is shown in figure 4.14b. The noise now appears more gaussian with the modus at the correct rate.

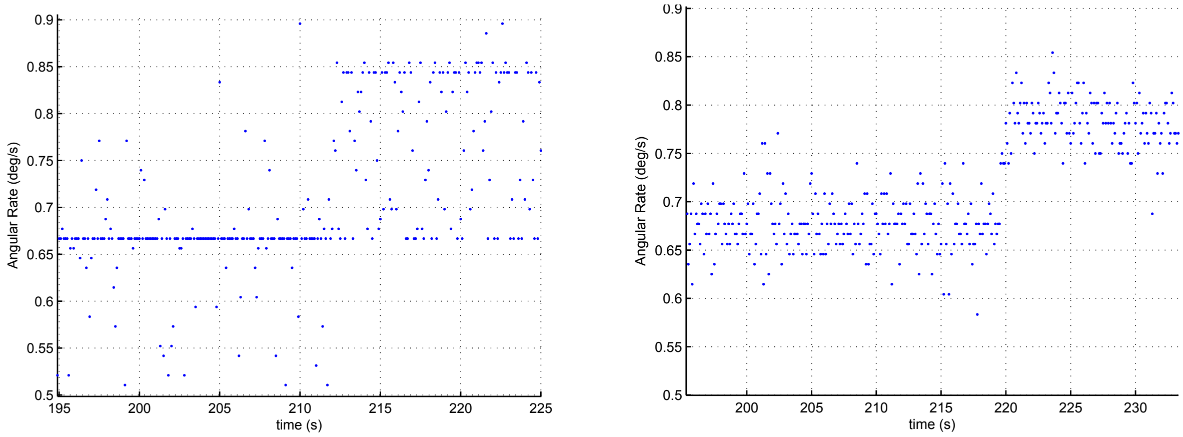

(a) Raw sensor data (b) FIR filtered data

Figure 4.14: CRM measurements: Step input

A fifth order Butterworth IIR filter was used to further reduce the noise. The $\mathcal{S}$-plane polynomial for a normalized fifth order Butterworth filter with cut-off frequency $\omega_c = 1$ rad/s is:

$$s^5 + 3.236s^4 + 5.236s^3 + 5.236s^2 + 3.236s + 1. \tag{4.3.9}$$

By substituting s with s/ω_c a new cut-off frequency can be chosen [47]. For a 1 second control period a 1Hz cut-off frequency will ensure the filter has a sufficiently fast transient response. The $\mathcal{Z}$-domain transfer function of the filter is shown below.

$$H(z) = \frac{0.0005767z^5 + 0.0105z^4 + 0.01887^3 + 0.005336z^2 + 0.0001487z + 1}{z^5 - 3.017z^4 + 3.893z^3 - 2.623z^2 + 0.9141z - 0.1309} \tag{4.3.10}$$

When the signal shown in figure 4.14b is filtered using this IIR filter, the signal shown in figure 4.15 is obtained.

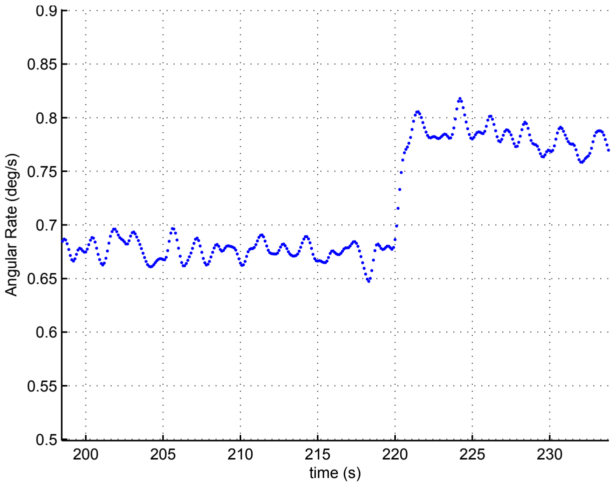

Figure 4.15: CRM200 rate measurements with IIR filter

4.3.3 Noise Analysis and Comparison

Noise in the output of the rate sensors can be attributed to a number of sources. The main types of noise include quantization noise, angle random walk, bias instability, rate random walk and drift rate ramp [48].

The Allan variance method has been proven to be an effective way to differentiate between different sources of noise and analyse their properties. In order to characterize the noise of the rate sensors, the Allan variance of each sensor's noise was examined.

4.3.3.1 Allan Variance

Consider a data set with N points with a sample time of t_0. If clusters of n data points are formed, with $n < N/2$, and the average value of each cluster is calculated, a new data set of N/n data points is formed with data points designated Ω_k. The Allan variance, $\sigma^2(\tau)$, of the original data set is the variance of Ω, or [49]:

$$\sigma^2(\tau) = \frac{1}{2}\langle[\Omega_{k+1} - \Omega_k]^2\rangle. \tag{4.3.11}$$

The value of $\sigma^2(\tau)$ is dependent on the cluster lengths. Varying n has the effect of changing τ, the sample time of Ω_k. Doing this, the magnitude of the different frequencies of the noise can be analysed. The two types of noise that were investigated were angle random walk and rate random walk.

Angle random walk, measured in $^\circ/\mathrm{s}/\sqrt{\mathrm{Hz}}$, is high frequency noise characterized by a white noise spectrum on the gyro rate output [48]. The effect of this noise can be reduced using appropriate filters. The value of the angle random walk can be read from the log-log plot of $\sigma(\tau)$ at $\tau = 1$ s on the -1/2 slope of the curve [49].

The rate random walk appears as a drift in the sensor bias. The main cause of this noise in MEMS sensors is temperature variation. Rate random walk is measured in $^\circ/s^2/\sqrt{\ \mathrm{Hz}}$ and can be read from the log-log plot of $\sigma(\tau)$ at $\tau = 3$ s on the 1/2 slope of the curve.

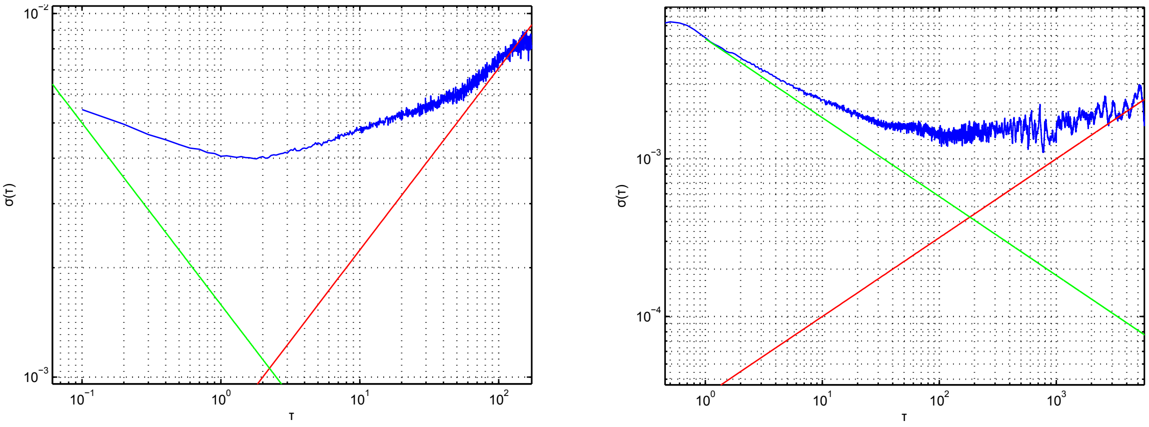

(a) LCG50 Allan variance

(b) CRM Allan variance

Figure 4.16: Allan variance

Figure 4.16 shows the log-log plot of the Allan variance of both rate sensors. The angle random walk of the LCG and CRM are $1.6 \times 10^{-3\circ}/\mathrm{s}/\sqrt{\mathrm{Hz}}$ and $6.3 \times 10^{-3\circ}/\mathrm{s}/\sqrt{\mathrm{Hz}}$ respectively. The rate random walk is $1.23 \times 10^{-3\circ}/\mathrm{s}^2/\sqrt{Hz}$ for the LCG and $0.055 \times 10^{-3\circ}/\mathrm{s}^2/\sqrt{\mathrm{Hz}}$ for the CRM200. From this we can deduce that the high frequency noise is less on the LCG than on the CRM, but has significantly higher drift. This can also be seen in figure 4.17, which shows the measurement outputs of the rate sensors when subjected to two 0.1°/s, two 0.05°/s and three 0.02°/s angular rate steps. The peak-to-peak noise of the CRM is larger, although the LCG measurements drift when the angular rate remains constant.

4.3.4 Temperature Calibration

As mentioned previously, temperature variation in MEMS sensors causes sensor drift. In order to compensate for this, the sensor should be temperature calibrated. This can be done by measuring the rate output and temperate output of the sensor when it is at rest while changing the sensor temperature. A polynomial can then be found which relates the temperate drift to the rate drift.

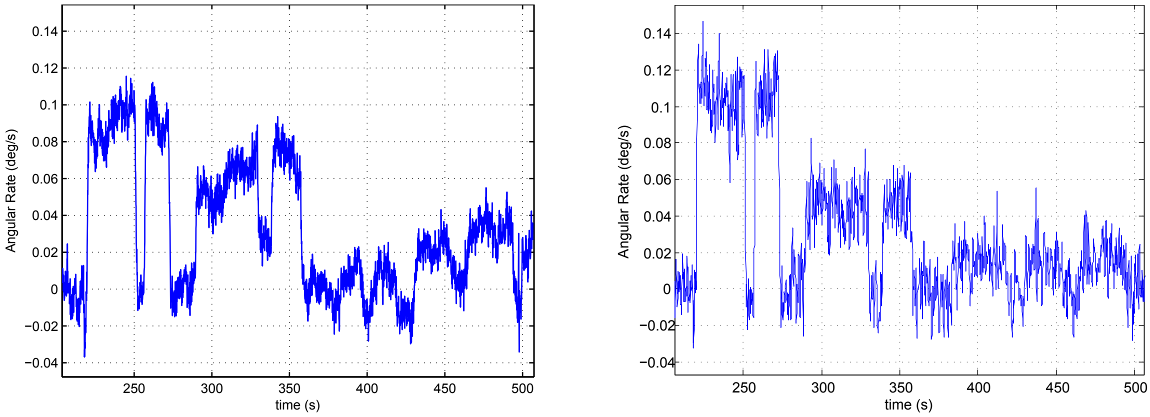

(a) LCG50 noise (b) CRM noise

Figure 4.17: Noise on rate sensors with angular steps input

Both sensors where put in a temperature oven and the temperature was swept from 25^{o}C up to 60^{o}C and back down in a period of 90 minutes. The following plots show the rate output drift with the bias at 25°C removed and a third order polynomial fitted in a least squares sense.

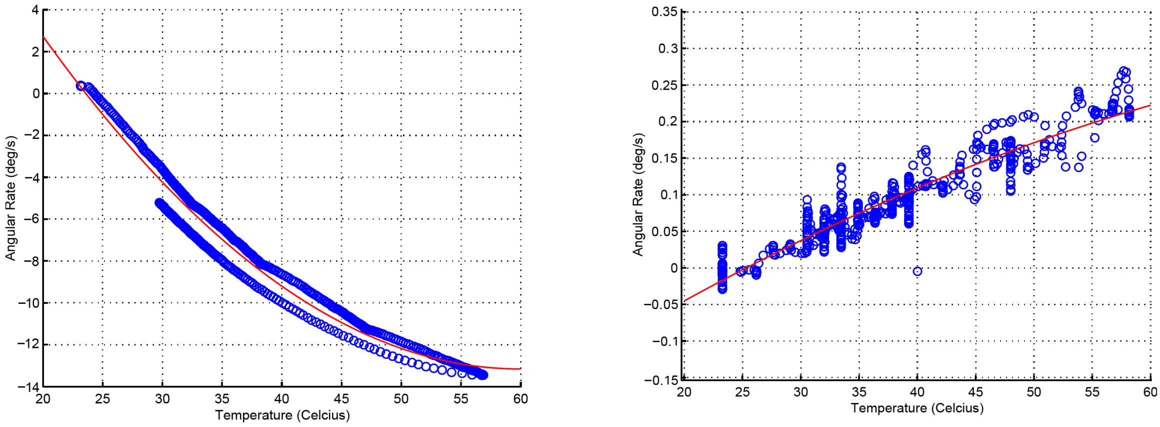

(a) LCG50 noise (b) CRM noise

Figure 4.18: Rate drift during temperature variation

The LCG is very sensitive to temperature variation with the rate output drifting a total of 14°/s. The measurements also do not follow the same path when the sensor is heated and when it cools down, with more than 1°/s difference in the rate measurement for the same temperature. This means that the bias cannot be calculated solely from the temperature measurements and will have to be estimated from other sensors. This bias correction can be done using slow (typically 1 Hz) attitude vector sensors like the magnetometer or horizon and sun sensors [50].

The CRM output only drifts 0.4°/s and the measurements follow the same path when heated and when cooled. Only the temperature measurement of the CRM is therefore required to accurately estimate its rate bias.

4.3.5 Comparison

Table 4.4 shows a summary of the rate sensor properties.

Table 4.4: Rate sensor properties

Parameter	**LCG50-100**	**CRM200**
Power		
Supply voltage	5 V	3.3 V
Power consuption	<40 mW	<16.5 mW
Physical		
Dimensions (mm)	29.4 × 29.4 × 11.7	6.3 × 5.5 × 2.7
Mass	12 g	0.3 g
Noise		
Angle Random Walk	1.6×10^{-3} °/s/$\sqrt{\text{Hz}}$	6.3×10^{-3} °/s/$\sqrt{\text{Hz}}$
Rate Random Walk	1.23×10^{-3} °/s^2/$\sqrt{\text{Hz}}$	0.055×10^{-3} °/s^2/$\sqrt{\text{Hz}}$
RMS noise	0.018 °/s	0.011 °/s

The fact that the CRM200 is small, can be mounted on a PCB and uses less power makes it easier to be incorporated on a CubeSat. Given that this sensor rate output varies linearly and predictably makes it easy to calibrate. This sensor does, however, require a lot of digital filtering and its angle random walk is higher than that of the LCG50. The LCG50 however is larger, uses more power and requires additional analogue filters. Its large bias drift with temperature variation also means that the sensor's bias will need to be estimated continually.

With proper estimation of the LCG50 bias, it will be able to provide marginally better measurements than the CRM200. Whether the advantage of slightly better rate measurements, accompanied with the reduced MCU computations required, outweighs the larger space and power requirements, depends on the mission. On ZACUBE-02 the rate sensor is not critical to the ADCS, therefore the CRM200 was chosen.

4.4 Aerodynamic Paddles

The aerodynamic paddles of the satellite will be folded down along the sides of the satellite during launch. The paddles will use a MAEVA hinge, consisting of bended metal strips, which will passively deploy the paddles and keep them fixed in the deployed position after release from the P-POD. After deployment stepper motors will be used to control the rotational angle of the paddles. Optical sensors will provide angular feedback to obtain the zero paddle angle.

4.4.1 Stepper Motors

Stepper motors offer simple and precise position control, making them well suited for the control of the aerodynamic paddle.

4.4.1.1 Hardware setup

As the motor will only be rotating the paddle in free space and the required rotational speed is less than 2°/s, the torque requirement of the motor is low. The motor should however have a accurate step resolution. If the step angle is too big, quantization of the output torque can reduce performance. The motor must also be small and lightweight to make it suitable for use on a CubeSat.

The motor chosen is the FAULHABER AM0820-V-5-56. This is a permanent magnet type stepper motor with a step resolution of 18°. A Series 08/1 64:1 gearhead is used in combination with the motor to decrease the step resolution to 0.28°. The motor torque is rated at 0.65 mNm, and the gearhead efficiency is 70%, resulting in an output torque of 29 mNm for full steps. This combination of motor and gearhead has a total length of 35.4 mm and a diameter of 8 mm and weighs only 7.9 g. This length allows two motors to fit into the 100 mm width of the Cubesat, leaving 29.2 mm for the paddle hinges. The motor and gearhead meet all the requirements.

The motors are driven using the A3901 dual full bridge motor drivers. Four I/O pins from the microcontroller are connected to the A3901 inputs. These pins switches the bridge outputs, connected to the motor phases, through the step sequence. The load voltage of the A3901, V_{BB}, is 5 V as to accommodate the motor. The minimum voltage for the input pins to register a logic one is $V_{BB}/2$, which allows the use of the MCU I/O pins, that operate at 3.3 V. The maximum current consumption per motor phase is 90 mA, which is below the maximum 400 mA the A3901 can deliver.

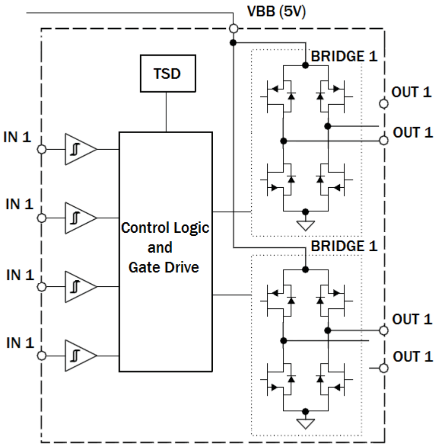

Figure 4.19: A3901 block diagram

4.4.1.2 Test Results

Initially the stepper motors were driven in half step mode with the motor phases always switched on. The current consumption using this method is too high, and therefore it is required to switch off the phases for a set time after each step. When the motor phases are switched off the motor jumps to its detent position. This occurs because the teeth of the magnetized rotor wants to align with the stator phases. When the motor is operated in half-step mode with the phases switched off for 0.5 s after each step the detent positions of the motor become apparent. When running the motor using this method the motor jumped to every second full-step every time the phases where switched off. In order to reduce the chance of missed steps, four consecutive half steps where performed with a hold-time of 2 ms for each half step. This was done in such a way that the motor would always stop in a detent position. The phases are then switched off for 92 ms in order to reduce current consumption. This manner of operation resulted in a motor speed of 5.6°/s, with an average power consumption of 65 mW when turning. The step resolution is 0.56°.

The torque capabilities of the motor were tested using a 5.8 mm diameter gear and a grooved strip as shown in figure 4.20.

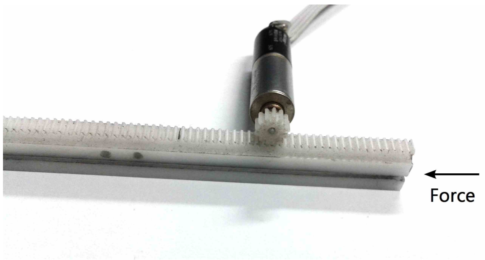

Figure 4.20: A3901 block diagram

The motor was able to resist an external force of up to 2.9 N, or a torque of 8 mNm, before not being able to overcome the detent torque and friction of the gearhead. This is sufficient for actuation of the aerodynamic paddles which will not experience large external torques. The holding torque of the motor (with phases switched off) was 19 mNm.

4.4.2 Optical Sensor

Although the angular position of the paddle can be calculated by counting the steps performed by the motor, feedback for a reference position is required for the eventuality that the step count is lost during operation such as after a power failure. This sensor will then allow the paddle to be brought back to its zero position.

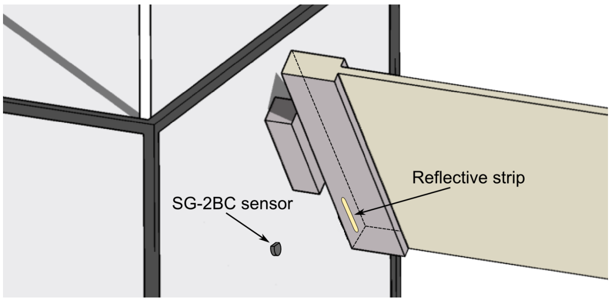

Figure 4.21: SG2BC posision on paddle

An infra-red LED and photo-transistor can provide feedback on the zero position. The LED and transistor can be mounted together on the satellite body and point towards the paddle as shown in figure 4.21. By having a reflective strip on the spot that the LED shines on when the paddle is at its zero position, the transistor will switch on. The MCU can detect this by measuring the voltage across a sense resistor.

The SG-2BC was chosen to serve as this sensor as it combines an IR-LED and phototransistor in a single package. The circuit diagram of the SG-2BC is shown in figure 4.22. The value of R_D is 1 kΩ, and the diode forward voltage is 1.3 V, resulting in a diode current of 2 mA. The emitter current is rated for 25 μA at this diode current when the SG-2BC is over a reflective area. The value for R_L is 120 kΩ. Assuming that V_{CE} is 0.7 V when the transistor is on, only 22 μA is required to reach a load voltage of 2.6 V. The load voltage is buffered with a voltage follower operational amplifier circuit, and then measured by a MCU analogue pin. The power consumption of the diode and R_D is 6.6 mW. The power consumption of the transistor and 120 kΩ resistor is negligible.

The sensor was tested using the setup shown in figure 4.23a. The sensor was mounted to a rotary stage 20 mm from the centre of rotation. A black non-reflective box with a 2.4

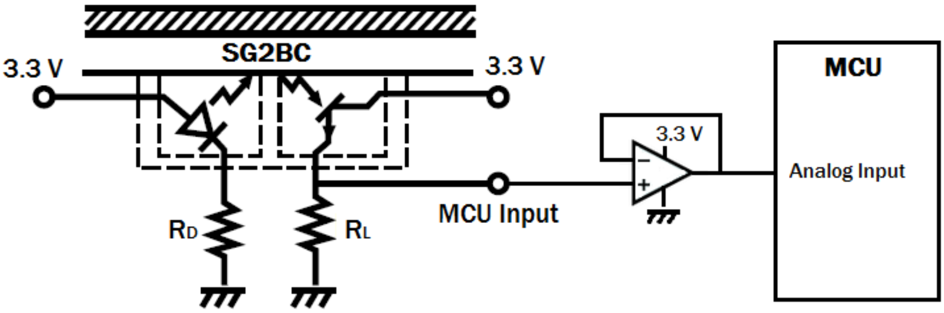
SG2BC
3.3 V
3.3 V
MCU
3.3 V
Analog Input
MCU Input
RD
RL

Figure 4.22: SG2BC circuit diagram

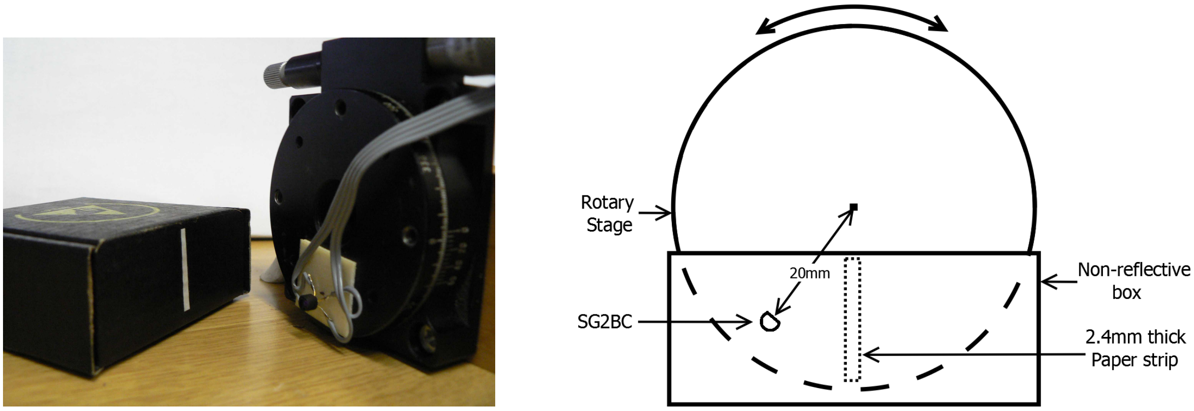
Rotary Stage
SG2BC
20mm
Non-reflective box
2.4mm thick Paper strip

(a) Actual setup (b) Diagram setup

Figure 4.23: SG2BC accuracy test setup

mm thick strip of white reflective paper was placed 0.8 mm in front of the sensor. The sensor was then rotated over the strip of paper. As the sensor comes closer to the paper, more IR light is reflected, and the output of the sensor increases to the point where the sensor is directly over the strip of paper and the maximum IR light is reflected back. The rotary stage was rotated around the centre position by 1° steps, followed by 0.5° steps. The output from the MCU ADC is shown in figure 4.24.

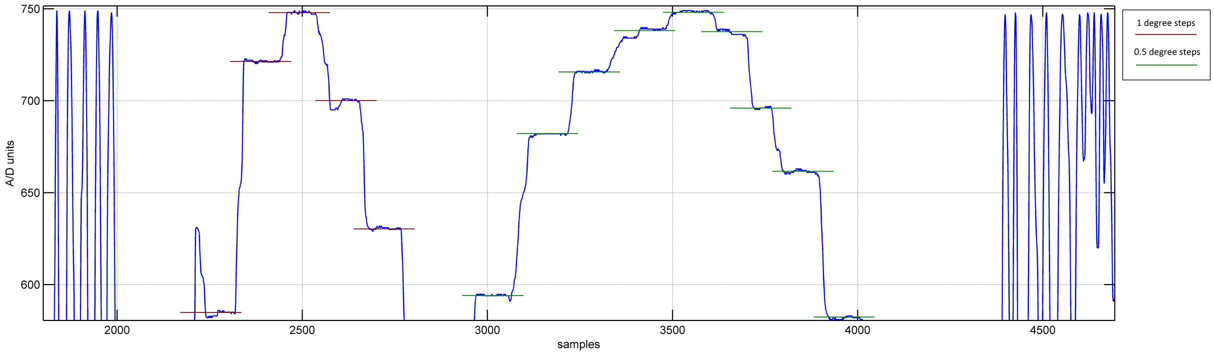

Figure 4.24: MCU A/D output

Different outputs are clearly visible, even for 0.5° steps. The maximum ADC value stays the same throughout the test, as can be seen from a series of quick rotations done around the centre position before and after the angular steps. From this it can be deduced that the sensor will be able to detect the centre position of the paddle to within the 0.56° step resolution of the motor.

4.5 Magnetometer

The HMC1053 was chosen to be the magnetometer for the satellite. It is designed for low magnetic field sensing and is in a very compact package, making it ideal for this application. Its reliable operation in space has also been verified by BEESAT-1 as mentioned in section 1.3.3.4. Its power consumption is 33 mW from a 3.3 V source.

4.5.1 Amplifier Circuit

The analogue output of the magnetometer, referenced to 1.65 V, is sent through an operational amplifier filter. The output of the filter is sampled by an external ADS1115 16-bit ADC, used to utilized the 120 μG resolution of the HMC1053. When designing the operational amplifier circuit, shown in figure 4.25, the worst case bridge offset and sensitivity must be considered to prevent the analogue signal from saturating. For 3.3 V operation, the sensitivity of the HMC1053, K_{sen}, is between 2.64 mV/G and 3.64 mV/G. The typical bridge offset for 3.3 V operation, V_{offset}, is ±1.65 mV, but it can be as high as ±4.13 mV. The maximum strength of the earth's magnetic field, B_{max}, is about 0.6 G. The largest signal from the magnetometer, V_{mag}, will then be:

$$\begin{aligned} V_{mag} &= K_{sen}B_{max} + V_{offset} \\ &= 3.64 \text{ mV/G} \times 0.6 \text{ G} + 4.13 \text{ mV} \\ &= 6.31 \text{ mV}. \end{aligned} \tag{4.5.1}$$

The ADS1115 has different options for its full scale voltage V_{scale}, including ±2.048 V and ±1.024 V, which is also referenced to 1.65 V by comparing the voltages from the channels 0, 1 and 2 with the 1.65 V on channel 3. The maximum operational amplifier gain, K_{op-amp}, is,

$$K_{op-amp} = V_{scale}/V_{mag} \tag{4.5.2}$$

or 325 for a V_{scale} of ±2.048 V and 162 for ±1.024 V. The gain of the operational amplifier is $R1/R2$. Resistor values of $R1 = 1.2\ M\Omega$ and $R2 = 5.1$ kΩ was chosen for a gain of 235.

When a magnetometer has a large bridge offset the ADS1115 can be set up for a V_{scale} of ±2.048 V, or, if the magnetometer has a smaller bridge offset the V_{scale} can be ±1.024 V, increasing the measurement resolution.

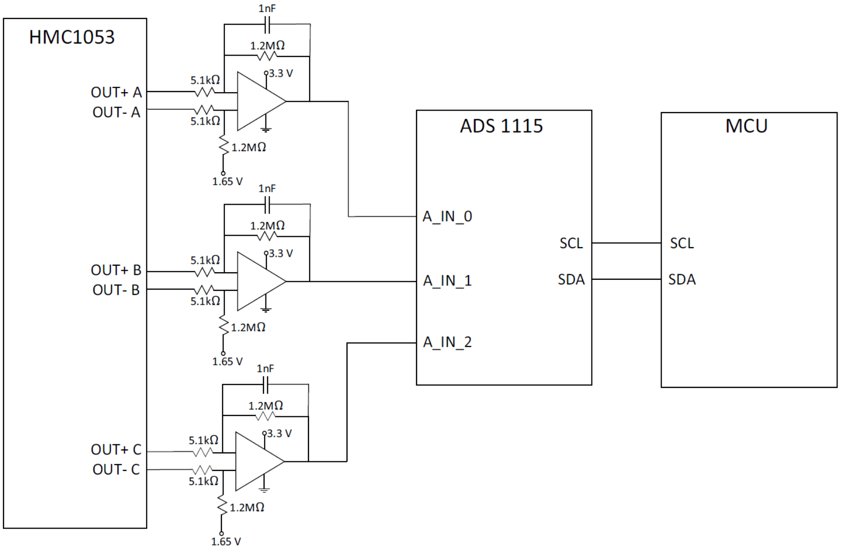

Figure 4.25: HMC1053 implementation

The ADS1115 ADC measures the magnetic field with a resolution of 81 μG when the V_{scale} is ± 2.048 V. The ADS1115 measurement is relayed to one of the MCUs via I2C. The output of the operational amplifier is also relayed directly to the second MCU to enable redundacy on the MCUs for magnetic control.

4.5.2 Temperature Compensation

The HMC1053 has a typical sensitivity temperature coefficient of -2700ppm/°C. In order to compensate for this, thermistors where added to the operational amplifier circuit in parallel with $R2$. Figure 4.26a shows the variation in the required gain for the HMC1053 output along with the variation in the operational amplifier gain with different thermistors in parallel with $R2$. Figure 4.26b shows the error percentage of the magnetometer output and the error percentage of the magnetometer with the compensation with the different thermistor values. The compensation circuit with the 120 kΩ thermistor keeps the error below 2% for temperatures between 10°C and 50°C and below 0.5% for temperatures between 20°C and 45°C. The 120 kΩ thermistor was therefore used.

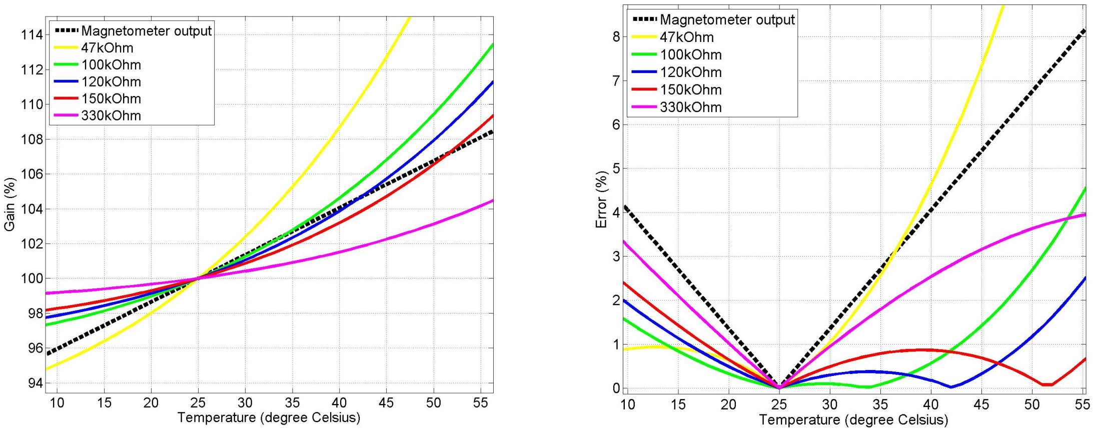

(a) Variation of Gain vs Temperature (b) Error vs Temperature

Figure 4.26: Temperature calibration gains and errors

4.5.3 Set/Reset Strap

The HMC1053 has a set/reset strap, which is a spiral of metalization which is used to condition the magnetic domains of the magneto-resistive elements. Current pulses must be sent through the set/reset strap periodically in opposite directions for the best performance. The circuitry used is shown in figure 4.27a. When the gate of the IRF7509 is driven high the NMOS transitor switches on and the PMOS switches off, and when the gate is driven low the NMOS transitor switches off and the PMOS switches on. By selecting which IRF7509 gate is driven high, the polarity of the voltage applied to the strap can be controlled. The 1 μF isolates the battery from high current spikes.

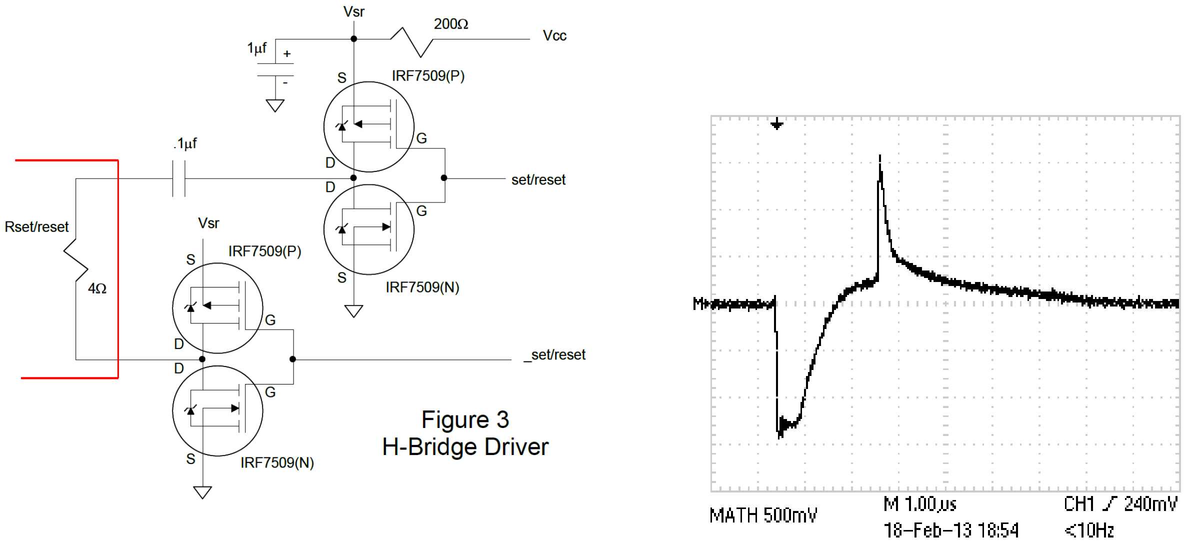
Vsr
200Ω
Vcc
1µf
+
-
S
IRF7509(P)
G
D
.1µf
set/reset
D
G
Rset/reset
Vsr
S
IRF7509(P)
4Ω
S
IRF7509(N)
G
D
_set/reset
D
G
S
IRF7509(N)
Figure 3
H-Bridge Driver
M
MATH 500mV
M 1.00µs
18–Feb–13 18:54
CH1 ⁄ 240mV
<10Hz

(a) Set/Reset circuit (b) Set/Reset strap voltage

Figure 4.27: Magnetometer Set/Reset

The voltage across the set/reset strap, when the set/reset line is switched high and low 2 μs later, is shown in figure 4.27b. The resistance of the set/reset strap was measured at 3 Ω, and the peak voltage is 1.5 V. The peak current is thus 0.5 A.

The magnetometer will be mounted on a deployable boom in order to reduce noise from the satellite electronics. The large set/reset strap pulse currents will cause noise and losses if flowing through a long cable. The set/reset circuitry was instead placed on the same PCB the magnetometer was mounted on. Having the operational amplifier circuitry and ADC on the PCB also reduces the noise from the cable. The size of the first PCB was 15 mm × 9 mm × 5.8 mm and it has a cable constisting of ten wires twisted to produce a bundle with a diameter of 1.8 mm. It has the HMC1053 and the reset circuitry on the PCB and is shown in figure 4.28a. The second PCB also had the operational amplifier cicuitry and ADC on the PCB. The size of the second PCB was 15.1 mm × 15.3 mm × 5.1 mm.

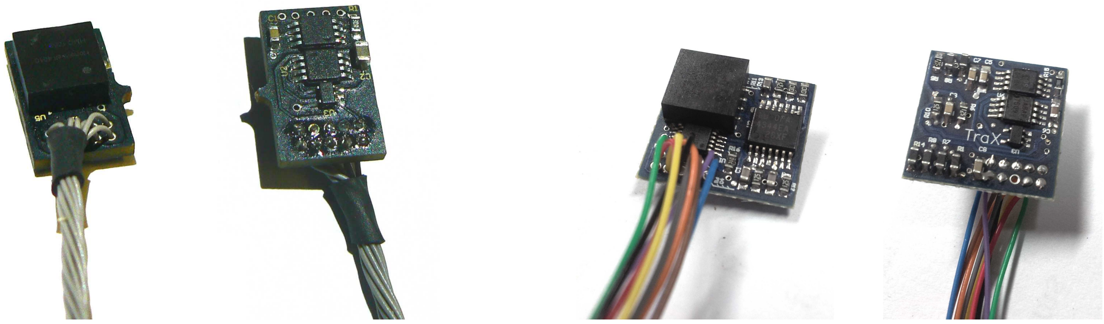
(a) First magnetometer PCB (b) Second magnetometer PCB

Figure 4.28: Top and bottom of magnetometer PCBs

4.6 Coarse Sun Sensor

The coarse sun sensor is implemented with the use of six SLCD-61N8 planar photodiodes. These diodes provide a linear short circuit current over a wide range of illumination. They where implemented as shown in figure 4.29.

With this circuit the short circuit current is measured, providing an accurate reading of the light intensity. The output of the operational amplifier is connected to a MCU ADC pin, which provides a 10-bit value relating to the light intensity. The typical short circuit current of the SLCD-61N8, I_{sc}, is rated at 170 μA at 25 mW/cm^2. For the solar constant of 137 mW/cm^2 assuming a linear sensitivity, the maximum I_{sc} will be 930 μA. A 1.8 kΩ

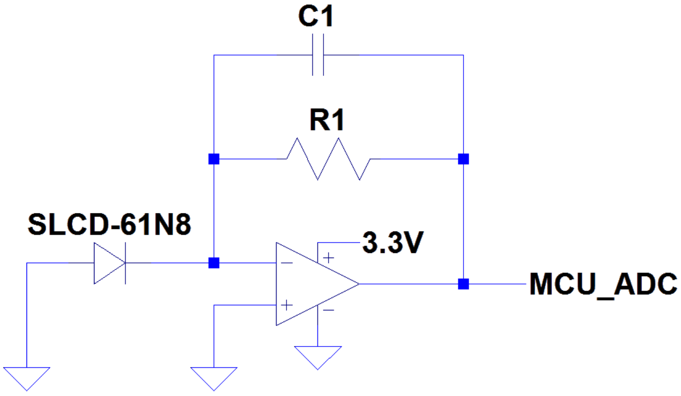

Figure 4.29: Photodiode Operational Amplifier circuit

resistor was chosen for $R1$ providing a maximum sense voltage of 1.67 V, leaving a 50% buffer for component uncertainty.

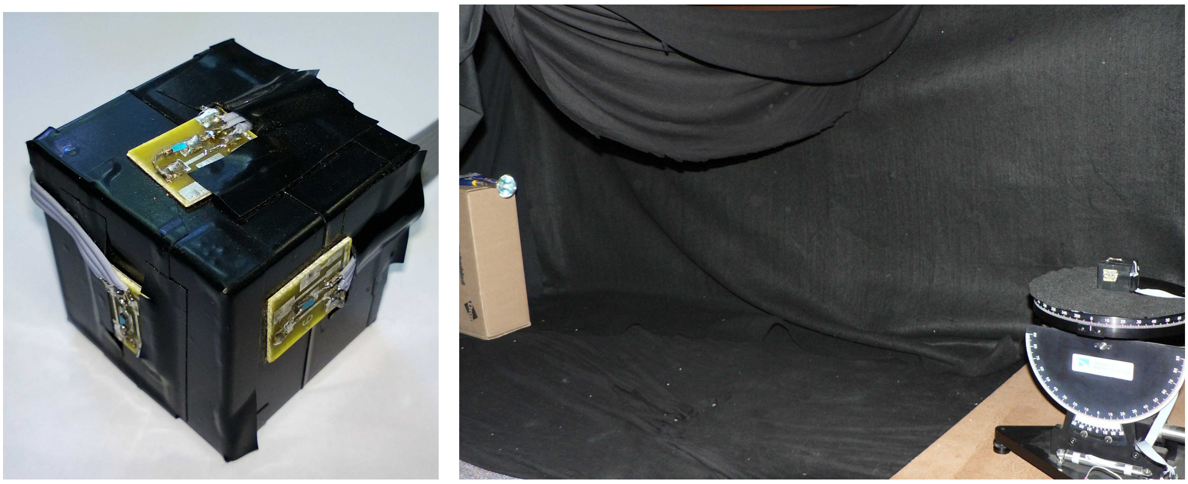

(a) Coarse sun sensor block (b) Actual Coarse sun sensor test setup

Figure 4.30: Coarse sun sensor test

In order to test the accuracy of the sensor, three diodes were fitted orthogonally to a square, in X, Y, and Z directions, and mounted upon a 2-axis rotation stage. The rotation stage was put in a 1.6 m × 0.9 m × 0.7 m area enclosed with black cloth. A 50 W DC lamp was placed opposite to the rotation stage at a distance of 1.3 m. The test setup is shown diagrammatically in figure 4.31. With this setup a resistor value of 390 kΩ for $R1$ resulted in a maximum output voltage of 1.7 V, which is below the saturation voltage of 3.3 V.

The sensors were calibrated by rotating the sensor from 0 degrees, pointing orthogonally to the light source, to 90 degrees, directly facing the light, and measuring the resulting output AD value. Each sensor was rotated in both directions, for example, the X-axis sensor was rotated 90 degrees about the Y-axis, and 90 degrees about the Z-axis. Ideally

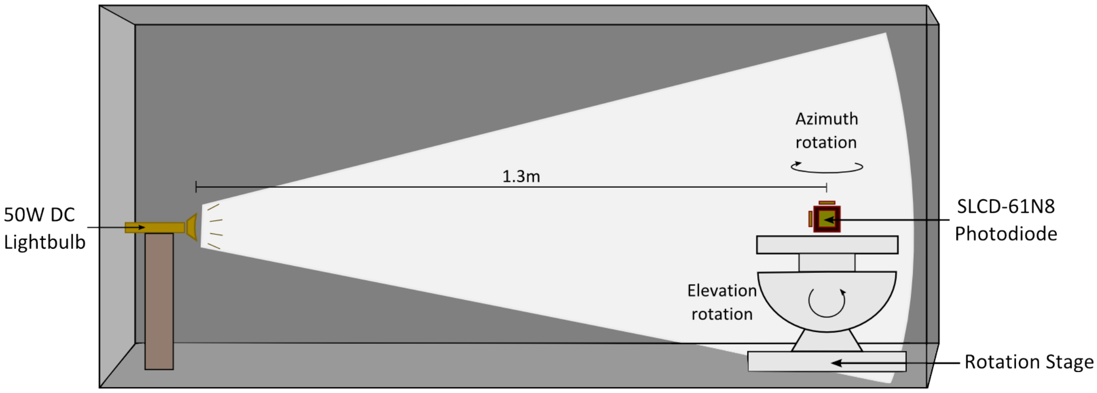

Figure 4.31: Coarse sun sensor test setup

the output would be the same, but due to the mounting and the soldering around the sensor there was a notable difference.

The sun vector is defined as an elevation and azimuth angle as shown in figure 4.32. The values of X_i, Y_i and Z_i are calculated from the incidence angle of the light on each sensor.

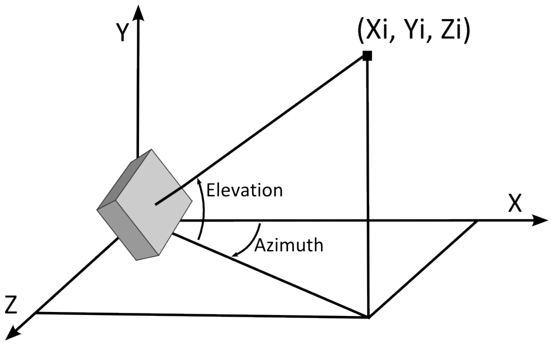

Figure 4.32: Sun vector angles

The incidence angle of the light on each sensor is deducted from the AD value. This is done using a lookup table or a function that relates the AD value to the light incidence angle. A high order polinomial can be found using the polyfit function of MATLAB. To get an accurate function, however, a very high order polinomial was needed. As the AD output is very sinusoidal, a sine function, with its parameters tuned to fit the graph, was used instead, which produced a smaller error than even a 10th order polinomial. Figure 4.33 shows the AD output of each sensor along with the fitted sine function.

Note the difference in the output AD value when rotating the sensor about different axis.

The function which relates the light incidence angle, θ_i, to the AD output value, f_{AD}, is:

$$f_{AD}(\theta_i) = K_1 \sin(K_2\theta_i + K_3) + K_4. \tag{4.6.1}$$

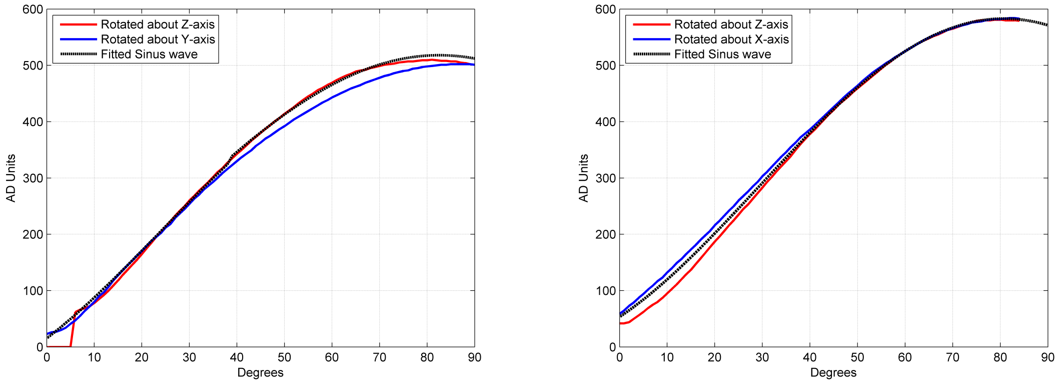

(a) X-axis sensor

(b) Y-axis sensor

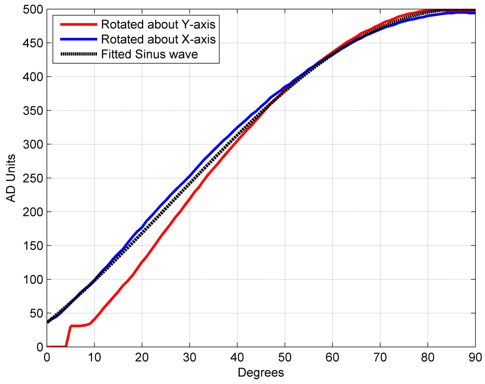

(c) Z-axis sensor

Figure 4.33: Sensor output calibration

The incidence angle can be caculated from the AD value with

$$\theta_i \;=\; \frac{\sin^{-1}[\frac{f_{AD}(\theta_i)-K_4}{K_1}] - K_3}{K_4}. \tag{4.6.2}$$

Figure 4.34 shows the accuracy of the sensor over a range of elevation and azimuth angles.

In figure 4.34a we see that the azimuth error is lower that 5 degrees for low elevation angles, but increases for elevation angles greater than 50 degrees. This error can be attributed to the inaccuracies seen in figure 4.33c for rotational angles smaller than 40 degrees. The elevation error seen in figure 4.34b is mostly below 3 degrees, only rising to 4 degrees at high elevation and at zero elevation, caused by the deviation seen in figure 4.33b at low angles. The absolute error in the sun vector angle, as seen in figure 4.34c, remains below 3 degrees for 48% of the test, the errors being due to a combination of the errors in elevation and azimuth. It is therefore concluded that with proper mounting and calibration the sun vector can be calculated to accuracies better than 5 degrees.

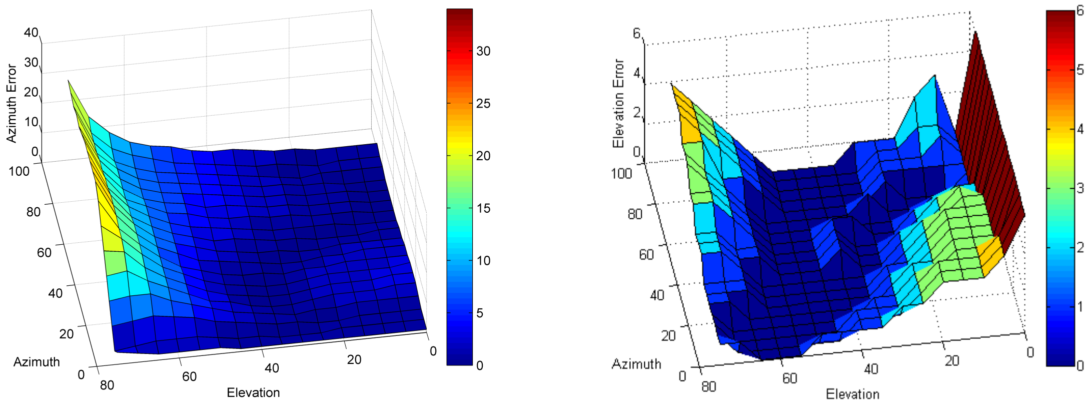

(a) Azimuth error (b) Elevation error

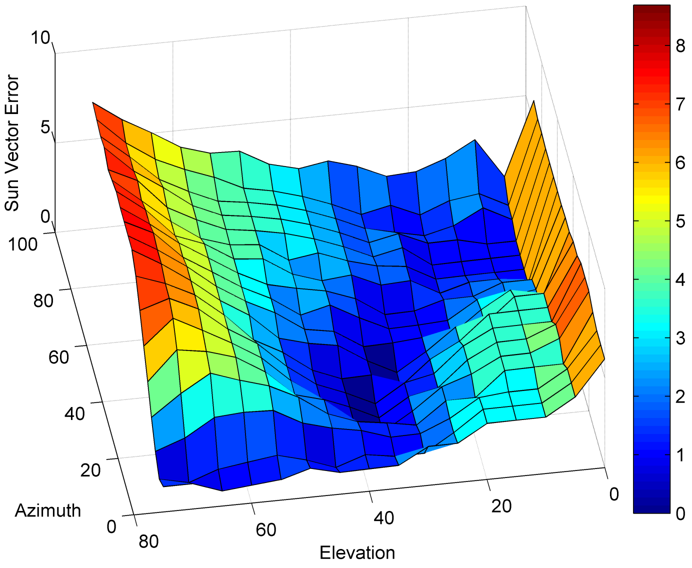

(c) Sun vector error

Figure 4.34: Coarse sun sensor accuracy

4.7 Microcontrollers

The tasks of controlling the different sensors and actuators on the CubeControl module are divided between two MCUs. Both MCUs must be able to do magnetic control. They both require:

- Six IO pins for the magnetorquer terminals
- One PWM pin for the magnetorquer current scaling
- One ADC pins for the magnetorquer current measurement
- One IO pin for the set/reset strap of the magnetometer

- Two I2C pins for communication with the OBC

The one MCU, which controls most of the sensors and the stepper motors, also require:

- Eight IO pins for controlling two stepper motors
- Two ADC pins for the paddle centre position feedback
- Two I2C pins for communication with the external ADC of the magnetometer
- Six ADC pins for the course sun sensor measurements
- Three ADC pins for the power measurements on the 3.3 V, 5 V and battery voltages

The second MCU will control all the BLDC motors. This MCU must have:

- Three IO pins for the direction control of the BLDC motors
- Three PWM pins for the current reference control signal of the BLDC motors
- Two IO pins for the switching of the 5 V and battery power for the BLDC motors
- One ADC pin for the battery voltage measurement
- Three ADC pins for the analogue magnetometer measurements
- Three SPI pins (MOSI, MISO and SCK) for the SPI bus on which the angular encoders and CRM200 rate sensor communicates
- Four IO pins for the slave select lines for the angular encoders and rate sensor
- One IO pin for the rate sensor reset line

The total number of pins required is 32 pins for the first MCU and 29 pins for the second MCU. For the first MCU a PIC18F45K22 met all the pin and function requirements and was chosen. For the second MCU a PIC18F47J13 was chosen. Having two different MCUs offers some component redundancy. For more accurate magnetometer measurements, the PIC18F47J13 offers a 12-bit ADC, compared to the 10-bit ADC of PIC18F45K22. For both PICs a 11.092 MHz external crystal oscillator is used from which a 44.368 MHz clock frequency is obtained using the 4× phase lock loop (PLL). The power consumption of the PIC18F45K22 during operation was measured at 55mW, and the PIC18F47J13 power consumption at 67 mW.

4.8 Power Switching

When the CubeControl module is integrated within the satellite it must be able to be switched on or off in order to save power and isolate errors. The redundancy in the magnetic control also requires that the two MCU's power be switched independently from each other. Figure 4.35 shows all the power switches on the CubeControl module, which components run from which power source and the signals between the different ICs.

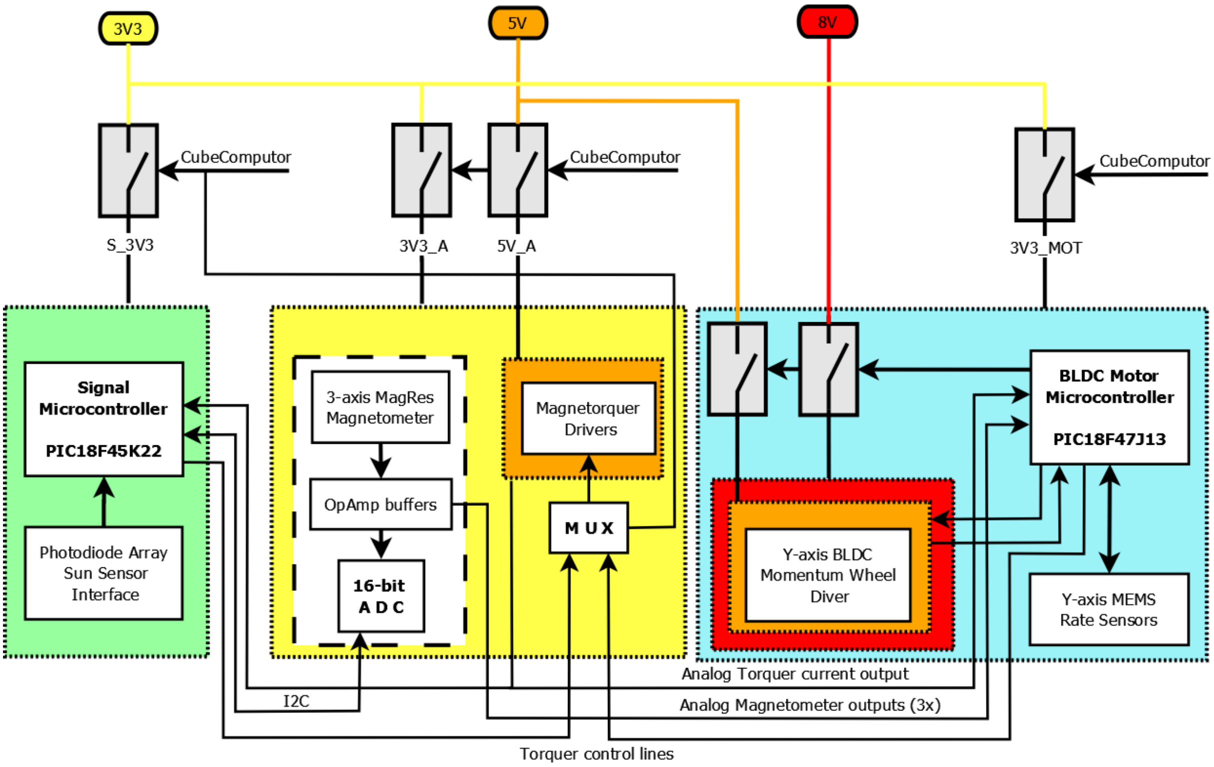
3V3
5V
8V
CubeComputor
CubeComputor
CubeComputor
S_3V3
3V3_A
5V_A
3V3_MOT
Signal Microcontroller
PIC18F45K22
Photodiode Array Sun Sensor Interface
3-axis MagRes Magnetometer
OpAmp buffers
16-bit ADC
Magnetorquer Drivers
MUX
BLDC Motor Microcontroller
PIC18F47J13
Y-axis BLDC Momentum Wheel Diver
Y-axis MEMS Rate Sensors
Analog Torquer current output
I2C
Analog Magnetometer outputs (3x)
Torquer control lines

Figure 4.35: CubeControl power switching

Three enable lines from CubeComputer are used to switch the signal PIC electronics, the motor PIC electronics and the common electronics, which include the magnetorquer and magnetometer circuitry. The motor PIC also has the ability to switch the motor electronics on or off.

For the 3.3 V and 5 V power sources a FPF2124 intelligent power switch is used. It has a selectable current limit between 0.15 A and 1.5 A. When the maximum current is exceeded the switch turns off and remains off until the "ON" pin is cycled. For the battery voltage a FPF2701 is used, which can be used for input voltages up to 36 V. Its current limiting works the same as the FPF2124, but its current limit is between 0.4 A and 2 A.

The overall power consumption of the CubeControl module is monitored using INA139 current shunt monitors on all the power lines. A 0.2 Ω series resistor is used with a 33 kΩ output resistor for a maximum measureable current of 0.5 A on each line. A 1 μF capacitor is used to filter the measurement with a 95% settling time of 100 ms.

Back powering can occur when ICs with different power sources are connected to each other and only one of them is switched on. To prevent back powering, I2C buffers are used on all the MCU I2C lines. Each MCU also uses a TLV2765 operational amplifier to buffer analogue signals from ICs powered by other power sources, such as the analogue magnetometer signals and the overall power consumption measurements. This operational amplifier has a shutdown feature, which allows the outputs to be put into high impedance mode, protecting the MCU ADC pins. The shutdown pin is connected to the power supply line of the MCU, automatically putting the operational amplifier in the shutdown mode when the MCU is powered down.

Chapter 5

Software Design

In this chapter the software design of the two microcontrollers (MCUs) are discussed as it is implemented on the CubeControl module used in the QB50 ADCS bundle. The techniques described here are applicable to both MCUs, except when stated otherwise.

5.1 Goals

The goal in developing the software is to make it simple for the On-Board Computer (OBC) to read the sensor data, send actuator commands and control the overall functioning of the CubeControl module. Attention is given to scheduling the tasks properly to avoid late measurements and lag in setting actuator control signals. The telemetry data is arranged in such a way to minimize transmission length but retain measurement resolution.

The OBC can request the following sensor data from CubeControl:

- The magnetometer measurements
- The coarse sun sensor measurements
- The Y-axis rate sensor measurement
- The momentum wheel speed

It can set and read the following actuator commands:

- The magnetorquer on time
- The momentum wheel reference speed/torque

The following operational data can be read:

- The status telemetry, containing the runtime, and software versions
- Error flags, indicating operational faults
- The time since the last syncronize command was received
- The 3.3 V, 5 V and battery voltage power usage
- The magnetorquer current
- The momentum wheel current
- The battery voltage at the motor driver input

CubeControl can also receive the following operational commands:

- Reset the microcontroller
- Switch the 5 V and battery voltages for the momentum wheel driver on/off
- Clear error flags
- Deploy the magnetometer boom

5.2 Overview

Both microcontrollers operate from a 11.092 MHz external crystal oscillator, from which a 44.368 MHz clock frequency (internal f_{osc}) is obtained using the 4× PLL. The instruction clock ($f_{osc}/4$) then operates at 11.092 MHz. This specific frequency allows high UART baud rates with small timing errors.

On a power cycle or reset command the microcontroller enters the *main()* function. All the MCU pins are initialized by setting the appropriate configuration registers. The MCU sets the status telemetry, which contains the identification information of the PIC, its software version and the run time. Each time a telemetry value is updated a corresponding telemetry buffer in **I2C.c** is loaded with the new values. The timers are initialized and turned on just before the program enters the main *while(1)* loop.

An overview of the program flow is shown in figure 5.1. From within the main loop the different operations are called to be executed based on the status of the control flags, which are continuously polled. Timers that create low priority interrupts are used to schedule when the control flags are to be set. Telecommands, which set actuator control signals, operation modes and telemetry requests are received via I2C. I2C communication is serviced in a high priority interrupt.

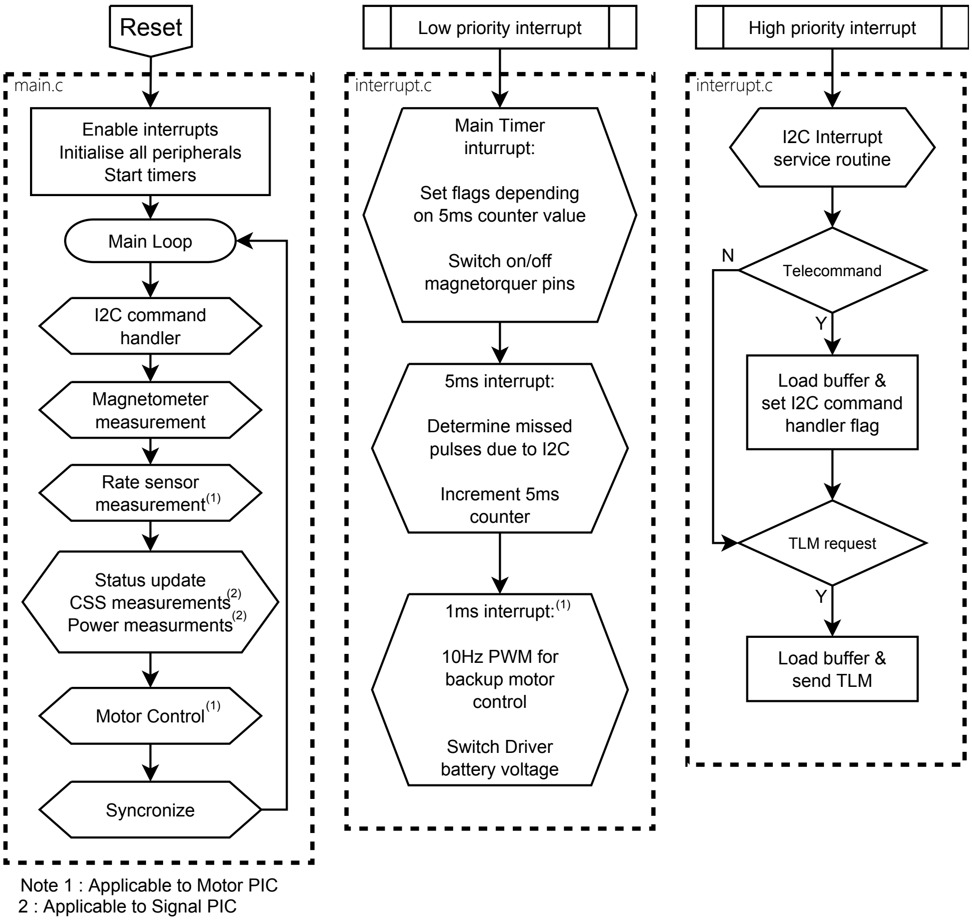
Reset
main.c
Enable interrupts
Initialise all peripherals
Start timers
Main Loop
I2C command handler
Magnetometer measurement
Rate sensor measurement(1)
Status update
CSS measurements(2)
Power measurments(2)
Motor Control(1)
Syncronize
Low priority interrupt
interrupt.c
Main Timer inturrupt:
Set flags depending on 5ms counter value
Switch on/off magnetorquer pins
5ms interrupt:
Determine missed pulses due to I2C
Increment 5ms counter
1ms interrupt:(1)
10Hz PWM for backup motor control
Switch Driver battery voltage
High priority interrupt
interrupt.c
I2C Interrupt service routine
Telecommand
N
Y
Load buffer & set I2C command handler flag
TLM request
Y
Load buffer & send TLM
Note 1 : Applicable to Motor PIC
2 : Applicable to Signal PIC

Figure 5.1: Program flow overview

The control flag operations include:

- I2C command handler, which executes telecommands based on the data within the I2C read buffer.
- Magnetometer measurement, which takes a single magnetometer measurement from the HMC1053.
- Rate sensor measurement, which takes a single rate sensor measurement from the CRM200 (motor PIC only).
- Status update, which updates the runtime. The signal PIC also updates the power and coarse sun sensor telemetry data.

- Motor control flag, which calculates the motor control signal and sets the duty cycle of the control pin.
- Synchronize flag, which resets the timer counters.

5.3 Scheduling

The ADCS estimators and controllers require that sensor data are received and actuators commands are sent at precise intervals. It is therefore important that the timing of the CubeControl module operations be synchronized with the OBC. This is achieved using a synchronize telecommand and a 5 ms timer to schedule the tasks. CubeControl is configured to operate at a 1 second control period within which all the operations need to be completed. Below, in figure 5.2, the scheduling within the CubeControl module is shown.

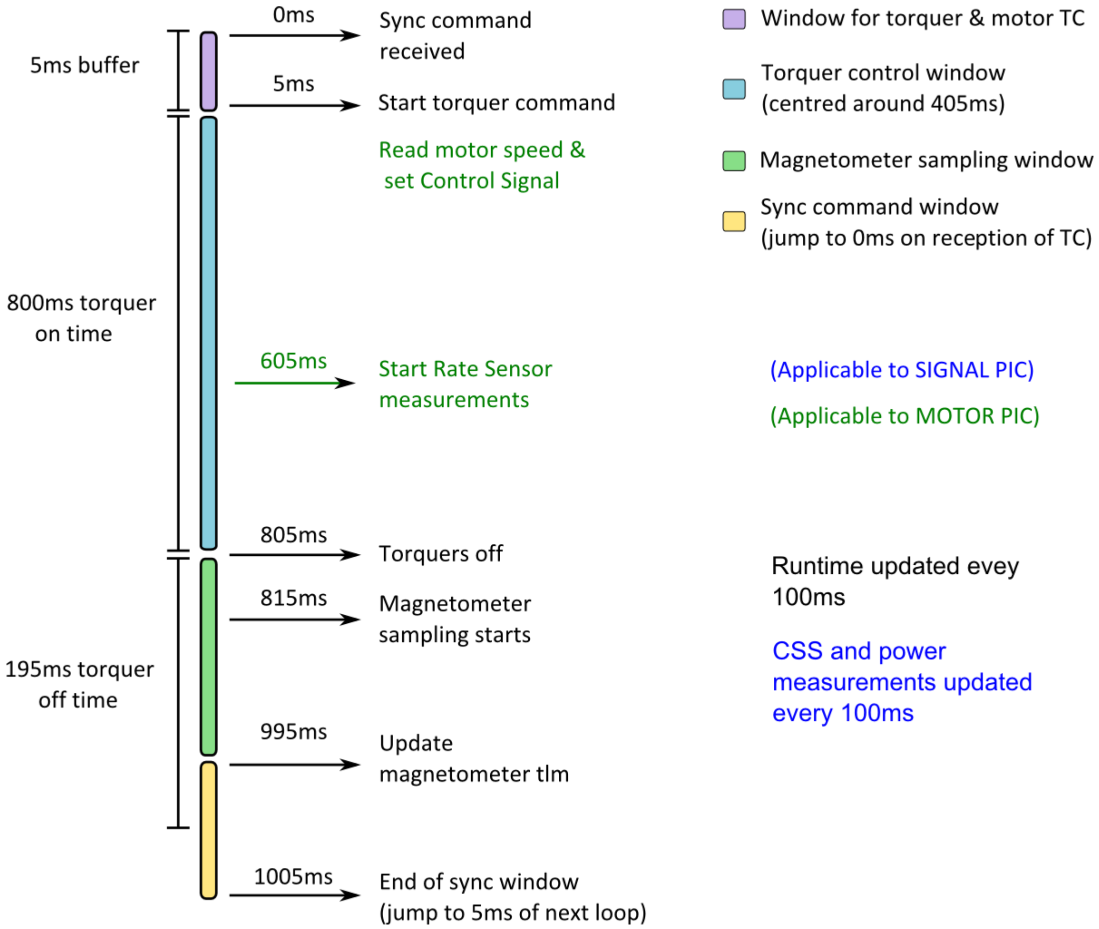
5ms buffer
800ms torquer on time
195ms torquer off time
0ms
Sync command received
5ms
Start torquer command
Read motor speed & set Control Signal
605ms
Start Rate Sensor measurements
805ms
Torquers off
815ms
Magnetometer sampling starts
995ms
Update magnetometer tlm
1005ms
End of sync window (jump to 5ms of next loop)
Window for torquer & motor TC
Torquer control window (centred around 405ms)
Magnetometer sampling window
Sync command window (jump to 0ms on reception of TC)
(Applicable to SIGNAL PIC)
(Applicable to MOTOR PIC)
Runtime updated evey 100ms
CSS and power measurements updated every 100ms

Figure 5.2: CubeControl 1s control period timing

When the synchronize telecommand is received the 5 ms timer is immediately reset and the interrupt flags are cleared. The synchronize flag is also set, which will trigger the

5 ms counter to be reset from within the main loop. The counter must be reset in the main loop to avoid the error which can occur if the synchronize command interrupted the program when it was busy servicing the 5 ms interrupt, causing an faulty incrementation. The 5 ms timer interrupt will trigger the main timer interrupt. It will also determine if interrupts were missed due to continuous high priority I2C communication and set the 5 ms counter to the appropriate value.

The main timer interrupt sets the control flags depending on the value of the 5 ms counter. On the first interrupt, on the motor PIC, the motor speed is read and the motor control flag is set. The 800 ms window for the magnetorquer control also starts here. Therefore it is important that both the magnetorquer and motor commands are received within the first 5 ms. Both the magnetorquer and motor commands' last byte indicate whether the command is regarded as a synchronize command. Only one of the commands must be set as a synchronize command.

The magnetorquer pins are also switched within the main timer interrupt. A counter, starting with a value of 20 at the 5 ms mark, increments towards 100. When the value equals 100 minus the on-time set by the user, one of the terminals of the magnetorquer is switched, depending on the direction of the command. The counter value then decrements back from 100 to 0. The one magnetorquer terminal is switched at 100 minus the on-time once again to turn to magnetoquer rod off again. This implemetation centres the control pulse within the 800 ms window.

The rate sensor control flag is set at the 605 ms mark. This allows 210 ms for 1000 measurements to be taken before the magnetometer sampling starts at 815 ms. After the magnetorquer window there is a 10 ms delay before the Set/Reset strap is set. Afterwards there is a further 5 ms delay (10 ms for motor PIC) before the magnetometer sampling flag is set. These delays ensure that the magnetorquers and Set/Reset pulsing does not influence the magnetometer readings. In figure 5.3 the analogue output from one of the magnetometer channels is shown, illustrating these delays.

When both PICs are switched on the Set/Reset strap is controlled by the Signal PIC, in which case the extra wait for the motor PIC ensures valid readings when both PICs are synchronized. At 905 ms the Set/Reset strap is cleared and at 910 ms (915 ms for motor) the reset measurements starts. The magnetometer telemetry will be updated by 995 ms. There is then a 10 ms window for the sync commands. If the sync command is not received by the 1005 ms mark, the magnetorquer command is cleared, and the timer jumps to the next control period.

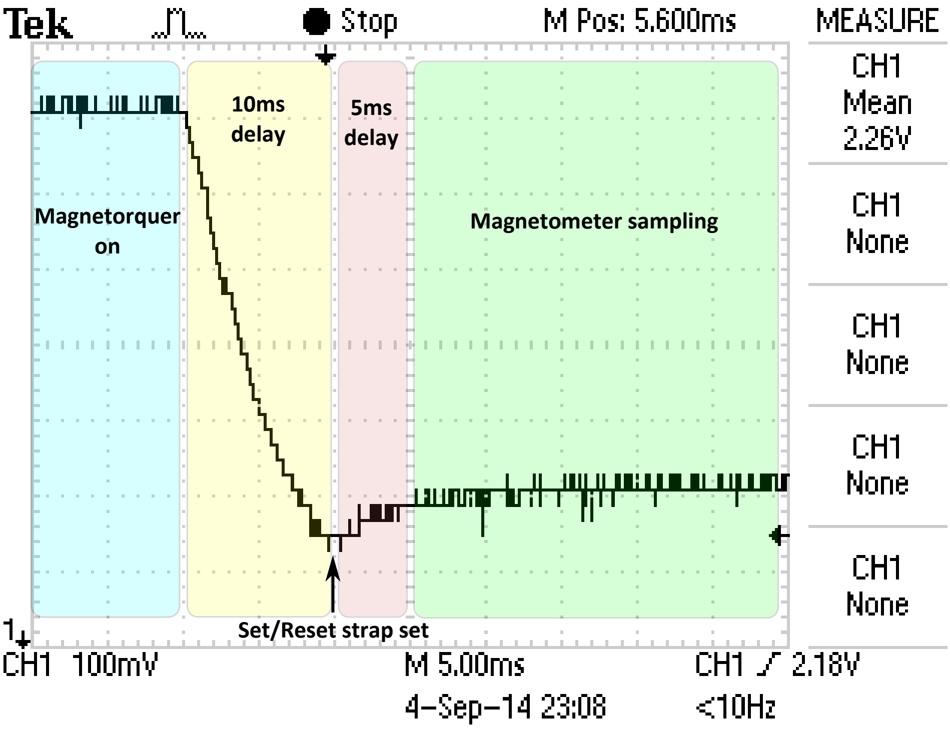

Figure 5.3: Magnetometer analogue output during delays

5.4 High Priority Interrupt

The I2C communication service routine is executed in a high priority interrupt. The microcontrollers are set up to operate as slaves. The Signal PIC address (read command) is 0xAA, and the motor PIC address is 0xCC. The I2C module is set up to create an interrupt on address matches, after each byte and on stop conditions. Clock stretching is also enabled to allow the PICs enough time to load the transmission buffer when sending telemetry data. The structure of an I2C message is shown in figure 5.4.

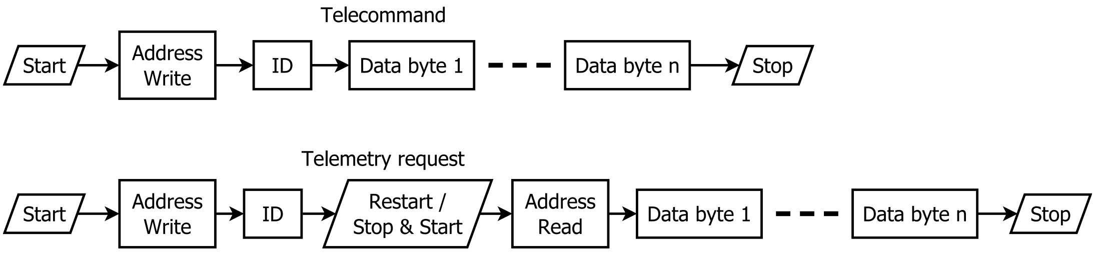
Telecommand
Start
Address Write
ID
Data byte 1
Data byte n
Stop
Telemetry request
Start
Address Write
ID
Restart / Stop & Start
Address Read
Data byte 1
Data byte n
Stop

Figure 5.4: I2C message structure

For a telecommand a start condition is followed by the PIC address with the read/write bit clear (write). An ID byte is sent first which indicates that the message is a telecommand by having the MSB clear, and also indicates which telecommand it is. The following bytes are all data bytes. For a telemetry request the ID will have the MSB set. Either restart or a stop and start condition can then be received. The next address byte will have the read/write bit set (read), which will prompt the PIC to transmit the telemetry data.

The program flow of the interrupt service routine (ISR) is shown in figure 5.5. A telemetry request will be serviced as follows: an address match will occur with the Read_not_Write bit within the SSP1STAT register set. The PIC will then set the state to '2' (reception). The next byte received will contain the ID of the telemetry package which is to be sent. The I2C write buffer will then be set to point to the corresponding telemetry buffer. Either a stop and start condition, or a restart condition can then be received. The Read_not_Write bit will now be clear which will result in the PIC setting the state to '3' (transmission) and loading the data within the I2C write buffer into the transmit buffer.

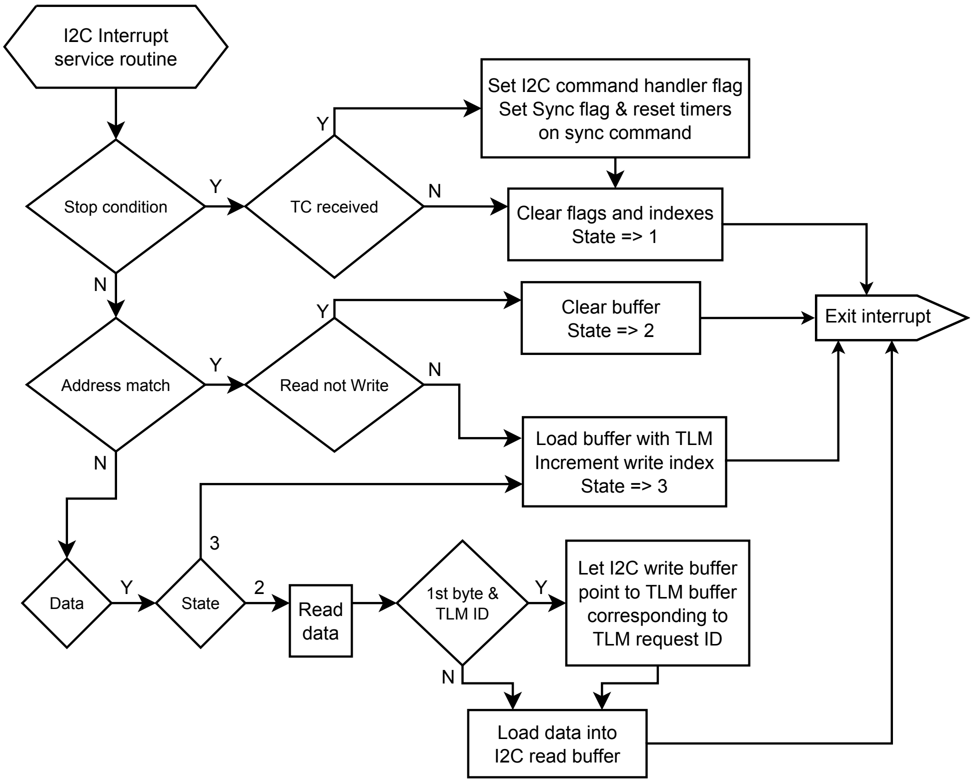
I2C Interrupt service routine
Stop condition
Y
TC received
Y
Set I2C command handler flag
Set Sync flag & reset timers
on sync command
N
Clear flags and indexes
State => 1
N
Address match
Y
Read not Write
Y
Clear buffer
State => 2
Exit interrupt
N
Load buffer with TLM
Increment write index
State => 3
N
Data
Y
State
3
2
Read data
1st byte & TLM ID
Y
Let I2C write buffer point to TLM buffer corresponding to TLM request ID
N
Load data into I2C read buffer

Figure 5.5: I2C ISR

A telecommand will be processed as follows: the Read_not_Write bit will be set and the state will be set to '2'. The next will be a telecommand ID, which will be stored along with all the following bytes until the stop condition is detected. On the stop condition interrupt the I2C command handler flag will be set which will trigger the command to be executed in the main loop.

5.5 Magnetometer Subroutine

When the magnetometer control flag is set, the subroutine shown in figure 5.6 is triggered from the main loop. The subroutine takes a single magnetometer measurement in one of the axes, increments the corresponding axis buffer and cycles to the next axis.

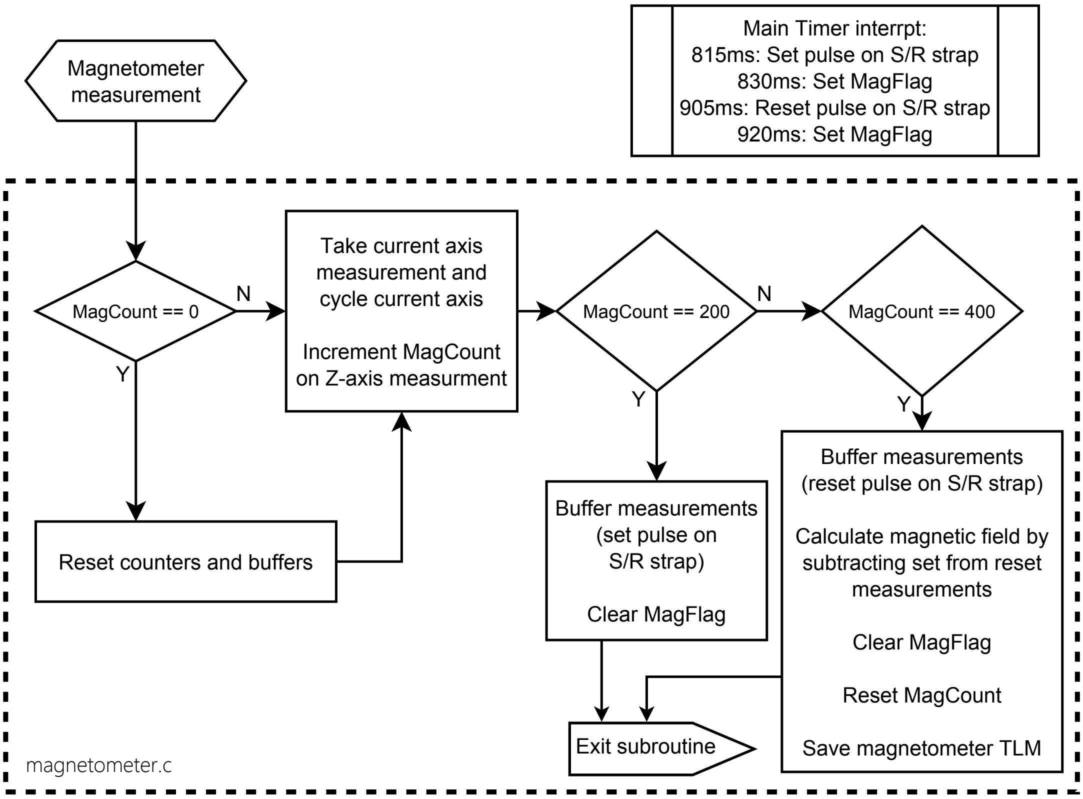
Main Timer interrpt:
815ms: Set pulse on S/R strap
830ms: Set MagFlag
905ms: Reset pulse on S/R strap
920ms: Set MagFlag
Magnetometer measurement
MagCount == 0
N
Y
Take current axis measurement and cycle current axis
Increment MagCount on Z-axis measurment
MagCount == 200
N
Y
MagCount == 400
Y
Reset counters and buffers
Buffer measurements (set pulse on S/R strap)
Clear MagFlag
Buffer measurements (reset pulse on S/R strap)
Calculate magnetic field by subtracting set from reset measurements
Clear MagFlag
Reset MagCount
Save magnetometer TLM
Exit subroutine
magnetometer.c

Figure 5.6: Magnetometer subroutine

The motor PIC samples the analogue magnetometer output with its 12bit ADC channel. It takes 200 measurements per axis for its positive “set” measurements, and 200 measurements for its negative “reset” measurements, taking 32 ms for a set of 200 measurements. To prevent overflows, the data type of the buffer for each axis is a 32 bit long integer. On completion of the set and reset measurements the resulting value is divided by 20, resulting in an overall gain of 10, and stored. The maximum difference between the set and reset voltages is:

$$\begin{aligned} V_{dif} &= 2 \times V_{sen} \times K_{op-amp} \times B_{earth} \\ &= 2 \times (1.2 \times 3.3\ \text{V})\ \text{mV/V/G} \times \frac{1.2\ \text{M}\Omega}{5.1\ \text{k}\Omega} \times 0.6\ \text{G} \\ &= 1.12\ \text{V} \end{aligned} \tag{5.5.1}$$

where V_{sen} is the magnetometer sensitivity, K_{op-amp} is the gain of the operational amplifier circuit and B_{earth} is the maximum magnetic field. The maximum difference relates to an

AD value of 1390, or 13902 with a gain of 10. This value is stored in a 16 bit signed short ensuring that an overflow cannot occur.

The signal PIC requests the 16 bit measurement made by the ADS1115 via I2C. It takes 15 positive "set" measurements, and 15 negative "reset" measurements per axis which are averaged. The difference between the positive and negative is then stored in a 16 bit signed short integer.

5.6 Momentum Wheel Subroutine

The motor driver is controlled using a PWM pin connected to the reference voltage input, a direction pin, and power switches for the 5 V and battery voltages. The speed of the motor is determined using the Hall sensor outputs which are fed through a 3-input XOR gate. The XOR output is connected to a T1CKI pin, which increments the timer 1 module register on a rising edge. One revolution of the motor creates six such edges. The register is read each second, resulting in a speed resolution of 10rpm. The reading and clearing of the timer 1 register occurs within the main timer interrupt at the 5 ms mark if the syncronize command was received on time. If the syncronize command is not received the motor speed is read at 1005 ms. In this case a flag will be set which prevents a syncronize command from reading the timer prematurely. This flag is cleared at 995 ms.

The operation of the motor is set with telecommands. The power telecommand sets the state of the 5 V and battery power supply to the driver. A control mode telecommand sets the speed controller gain and the driver switching method. When a torque command is received the "speed-not-torque" flag, S_n_T, is cleared and the control signal will be set to the requested value. When a reference speed command is received, the S_n_T flag is set. The absolute value of the reference speed is stored and the direction pin is set based on the reference speed direction. The PIC will then calculate the required control signal to spin the wheel up to the specified speed. By limiting the control signal to positive values (between 0% and 100%) and assuming the measured motor speed is in the same direction as the reference speed direction control is possible without direction feedback.

The motor control flag is set along with the reading of the motor speed within the main timer interrupt. The motor controller subroutine is called from the main loop. The program flow of the motor control function is shown in figure 5.7. The motor speed is limited at 9000 rpm. If the speed exceeds this limit a zero control signal will be set. If the S_n_T flag is clear the duty cycle of the PWM is set equal to M_PWM_REF, the value received in the torque telecommand. If a speed command larger than 15 rpm (minimum speed) was received the motor control law is implemented to determine the control signal.

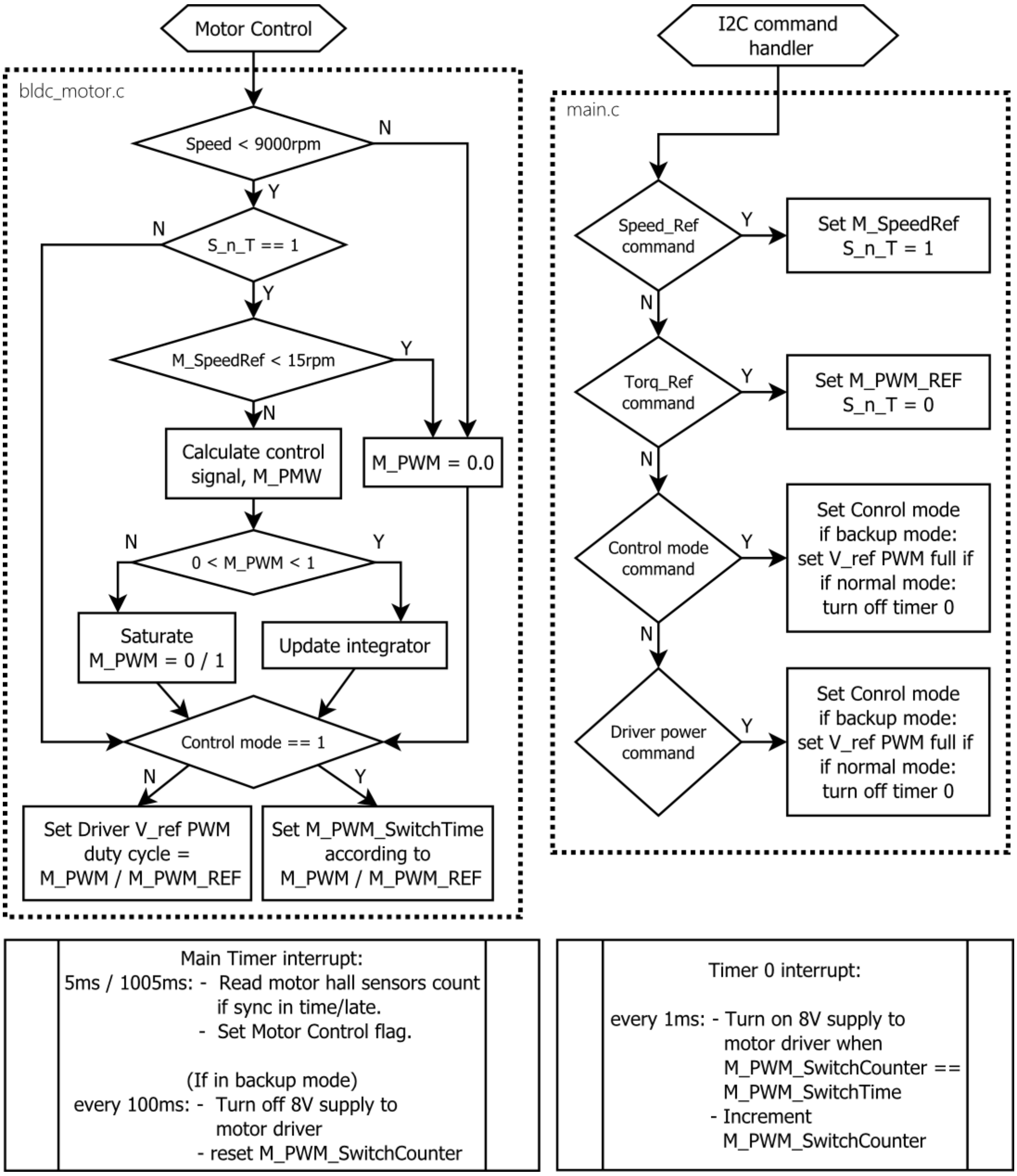
Motor Control
bldc_motor.c
Speed < 9000rpm
N
Y
S_n_T == 1
N
Y
M_SpeedRef < 15rpm
Y
N
Calculate control signal, M_PMW
M_PWM = 0.0
0 < M_PWM < 1
N
Y
Saturate M_PWM = 0 / 1
Update integrator
Control mode == 1
N
Y
Set Driver V_ref PWM duty cycle = M_PWM / M_PWM_REF
Set M_PWM_SwitchTime according to M_PWM / M_PWM_REF
I2C command handler
main.c
Speed_Ref command
Y
Set M_SpeedRef S_n_T = 1
N
Torq_Ref command
Y
Set M_PWM_REF S_n_T = 0
N
Control mode command
Y
Set Conrol mode if backup mode: set V_ref PWM full if if normal mode: turn off timer 0
N
Driver power command
Y
Set Conrol mode if backup mode: set V_ref PWM full if if normal mode: turn off timer 0
Main Timer interrupt:
5ms / 1005ms: - Read motor hall sensors count if sync in time/late.
- Set Motor Control flag.
(If in backup mode)
every 100ms: - Turn off 8V supply to motor driver
- reset M_PWM_SwitchCounter
Timer 0 interrupt:
every 1ms: - Turn on 8V supply to motor driver when M_PWM_SwitchCounter == M_PWM_SwitchTime
- Increment M_PWM_SwitchCounter

Figure 5.7: Motor subroutine

If the control signal is between 0% and 100% the integrator is updated. If not, but the direction is correct, the integrator is not updated in order to avoid integrator wind-up. It is also possible that speed commands are received during transients, which can result in the control signal being saturated in the wrong direction. In this case the integrator is updated which will bring the control signal back to the appropriate value.

When operating in the normal driver switching method, the control signal is set using the registers of the PWM timer. A non-liniarity of the driver for small commands is compensated for with the use of a look-up table. When using the backup switching method the duty cycle of the PWM pin is set to 100% and a variable, M_PWM_SwitchTime, is set to the control signal duty cycle value. The control is then achieved by switching the battery supply with a PWM signal at 10 Hz. Timer 0 is used, which creates a low priority interrupt every 1 ms on which a counter is incremented to 100. When the counter equals 100 minus the M_PWM_SwitchTime value the battery voltage is switched on.

The subroutine for the control of the reaction wheels is similar to that of the momentum wheel, except for the speed measurement, which is calculated using an AS5055 angular encoder instead of the Hall sensors. Also, the control period of the reaction wheel controller is 100 ms instead of the 1 s control period of the momentum wheel controller. The reaction wheel controller is described further in section 6.3.

5.7 Rate Sensor Subroutine

The motor PIC communicates with the rate sensor via a SPI interface. The clock pin frequency is set at Fosc/64, or 0.7 MHz, which is within the required frequency range specified by the CRM200 datasheet. The timing requirements of the CRM200 are met using *wait()* functions. Six bytes are read on each measurement. The first is a status byte which verifies that the sensor was set up correctly. The second and third byte contains the rate data. Bytes 4 and 5 contain the temperature reading. Byte 6 is a checksum byte. The rate sensor takes 1000 rate measurements which are summed and then divided by 250. This filters the measurements and scales the value to the appropriate range. The flag to start taking measurements is set at the 605 ms mark. The *readRate()* function adds a single measurement and increments the measurement counter. When the counter reaches 1000 the *FilterRate()* function is called, which implements the filter described in section 4.3.2. The flag is then cleared and the new telemetry loaded into the appropriate buffer. This takes 198 ms to complete, which means the magnetometer measurements does not overlap with the rate sensor measurements. The output of the rate sensor is in the range ±75°/s with a scale factor of 96 A/D units per °/s. With the gain of 4 provided by the oversampling the output range is ±28800 A/D units, which is stored in a signed short data type.

Chapter 6

Interfacing and Testing

This chapter describes the interfacing setup used to communicate with the CubeControl module. It also discusses the reaction wheel speed control algorithms and compares the modelled behaviour with that of the actual reaction wheel.

6.1 Interfacing Setup

The interfacing setup shown in figure 6.1 was used to test the CubeControl module. A MATLAB Simulink model, shown in Appendix B, was created to act as a graphical user interface (GUI). Telecommands are set based on a series of switches and slider values, and telemetry data is plotted using scopes which also save the data to the MATLAB workspace. A S-function block is used to open a COM port which allows communication with a CubeDock module using a UM232R USB-to-UART converter. The S-function executes the *mdlOutputs()* function every sample period. Within the *mdlOutputs()* function the S-function block inputs are read and telecommands are sent to CubeDock. Telemetry data is then read from CubeDock after which the S-function block outputs are set. Following the telemetry data a ‘done’ character is received which indicates the end of the sample period.

The CubeDock module supplies the CubeControl module with power as well as acting as an OBC, communicating with the CubeControl module over the I2C interface. It implements a one second loop in which it sends the synchronize (actuator) commands, initiating the control period of CubeControl, and requests the previous telemetry data which is relayed to MATLAB followed by the ‘done’ character. Telecommands received from MATLAB are serviced in an interrupt routine which immediately relays the telecommand to CubeControl, except in the case of the actuator synchronize commands. For actuator commands the data is stored and sent to CubeControl in the beginning of the next one second control period.

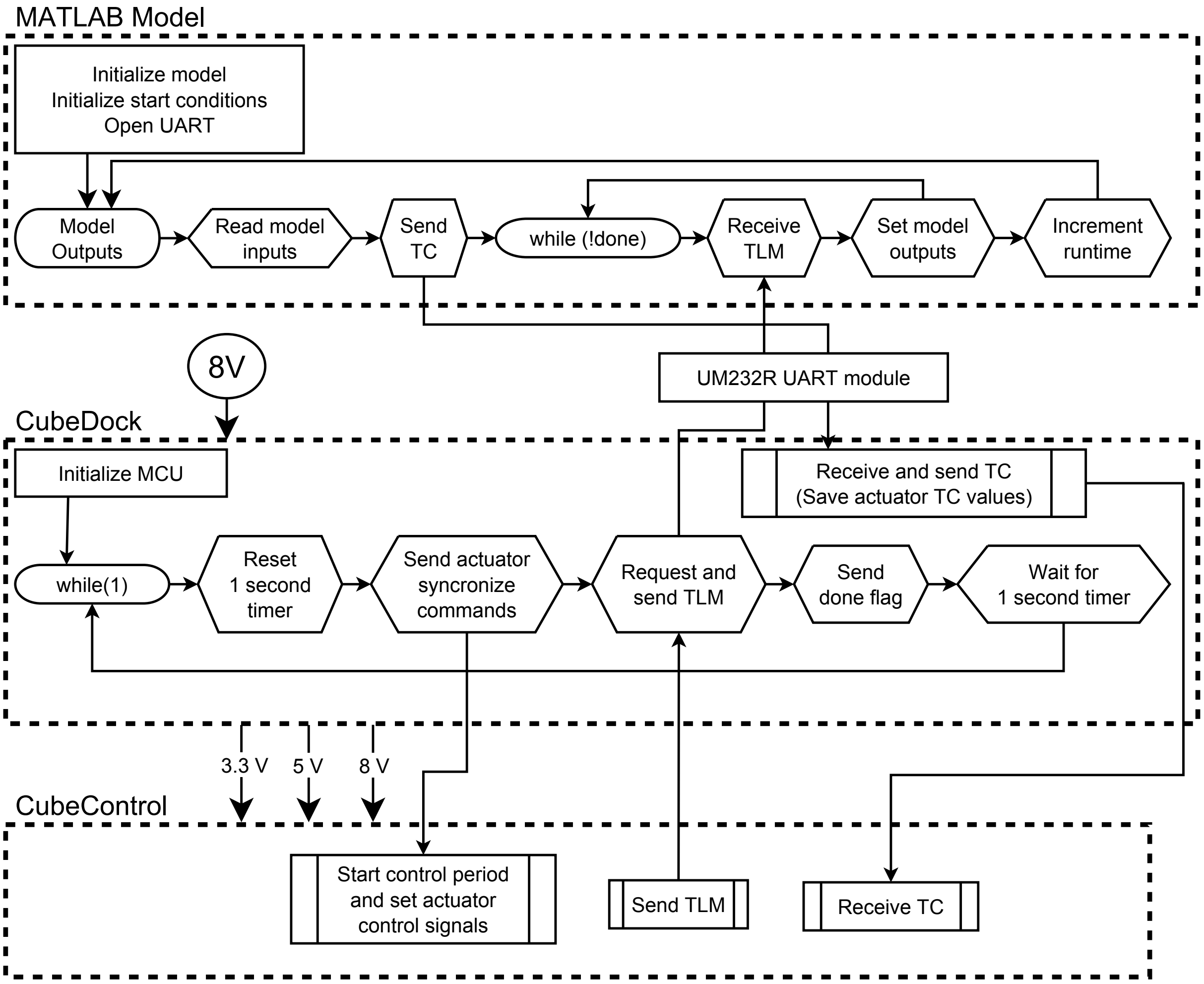
MATLAB Model
Initialize model
Initialize start conditions
Open UART
Model Outputs
Read model inputs
Send TC
while (!done)
Receive TLM
Set model outputs
Increment runtime
8V
UM232R UART module
CubeDock
Initialize MCU
Receive and send TC
(Save actuator TC values)
while(1)
Reset 1 second timer
Send actuator syncronize commands
Request and send TLM
Send done flag
Wait for 1 second timer
3.3 V
5 V
8 V
CubeControl
Start control period and set actuator control signals
Send TLM
Receive TC

Figure 6.1: Interfacing setup

Using this setup with the telecommands and telemetry requests mentioned in section 5.1 the correct functioning of all the hardware components were verified.

6.2 Magnetometer Calibration

In order to get an accurate measurement of the magnetic field the magnetometer sensitivity, K_{sen}, and bias offset, V_{offset}, mentioned in equation 4.5.1, need to be determined. Accurate calibration of the magnetometer is done in orbit, but an initial calibration is also required. This calibration was done using a Helmholtz coil and a FVM400 fluxgate magnetometer. The fluxgate probe and HMC1053 magnetometer was placed within the

Helmholtz coil with their axis aligned. Using the fluxgate magnetometer measurements as feedback, the magnetic field was controllable with a peak error of less than 40 nT.

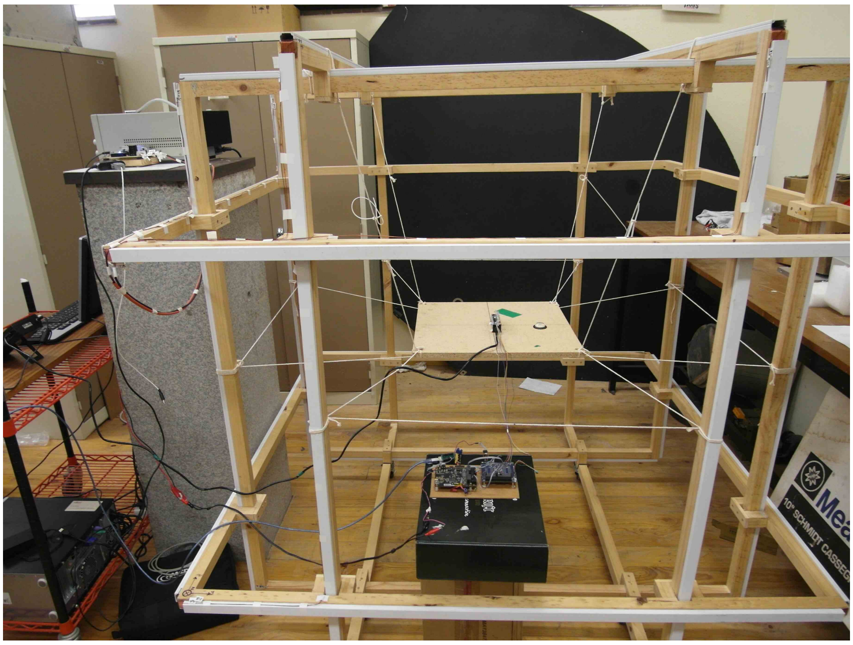

Figure 6.2: Magnetometers inside Helmholtz coil

The Helmholtz coil was firstly used to cancel out the geomagnetic field. The HMC1053 magnetometer measurements are then equal to the magnetometer biases. The required gain for each axis is then determined separately by subjecting the magnetometer to an 40 μT magnetic field in the specific axis and subtracting the bias from the measurement. The applied field divided by the measurement is then equal to the required gain. In table 6.1 the offsets and sensitivities of two HMC magnetometers are shown. The values for K_{sen} and V_{offset} fall within the range specified by the HMC1053 datasheet.

Table 6.1: Magnetometer baises and sensitivities

Parameter	**Bias (units)**	**$\mathbf{V_{offset}}$ (mV)**	**Gain (nT/unit)**	**$\mathbf{K_{sen}}$ (mV/G)**
Magnetometer 1				
X - axis	-59.9	-0.004	2.3	2.887
Y - axis	2949	0.2	2.366	2.807
Z - axis	1505	0.1	2.26	2.937
Magnetometer 2				
X - axis	-1285	-0.085	2.249	2.952
Y - axis	154	0.01	2.441	2.721
Z - axis	675	0.045	2.362	2.811

Using the calibration values listed in table 6.1, the noise levels on each axis where measured for a zero and a 40 μT magnetic field. The average mean errors and RMS noise levels around the mean values for 300 samples are listed in table 6.2.

Table 6.2: Magnetometer errors

Parameter	**Zero field mean error (nT)**	**Zero field RMS error (nT)**	**40 uT field mean error (nT)**	**40 uT field RMS error (nT)**
Magnetometer 1				
X - axis	-1.2	21.8	40	23.8
Y - axis	7.7	26.8	63	27.3
Z - axis	-3.8	25.5	102.7	18.7
Magnetometer 2				
X - axis	4.9	18.1	86.1	17.9
Y - axis	-15.3	14.5	75.2	14.8
Z - axis	-22.5	15.6	-41.8	16.4

The temperature compensation circuit was also tested by measuring vector magnitude variation for a [40 40 40] μT magnetic field vector when the temperature goes from 21°C to 50°C. The variation of the vector magnitude measured with a magnetometer without temperature compensation was 4.36 μT, while a magnetometer with temperature compensation gave a 1.59 μT variation. For both magnetometers the direction of the magnetic field vector changed by less than one degree.

6.3 Reaction Wheel Control

The control period of the reaction wheel is 100 ms during which the speed measurement is updated and the control signal calculated and set.

6.3.1 Speed Measurement

The speed of the motor is calculated using consecutive angle measurements from the AS5055 magnetic encoder. The AS5055 measures the motor angle with 12 bit resolution (0 to 4095). A set of 11 measurements are taken with 5 ms between each measurement. These measurements are taken in the last 55 ms of the 100 ms control period to minimize measurement lag.

Two methods were used for deducing the motor speed from the angle measurements. Method one takes the average angle difference between the consecutive measurements. The calculated motor speed using this method equates to the total angle difference between the first and last measurement divided by the time between the first and last measurement.

Method two uses least squares fitting to find the slope of the straight line formed by all the angle measurements, y_i, at their respective measurement times, x_i, according to equation 6.3.1.

$$\omega_{unit/5ms} = \frac{n\Sigma_{i=1}^{n} x_i y_i - \Sigma_{i=1}^{n} x_i \Sigma_{i=1}^{n} y_i}{n\Sigma_{i=1}^{n} x_i^2 - \Sigma_{i=1}^{n} x_i} \tag{6.3.1}$$

As the output of the AS5055 corresponds to an angle between 0 and 360 degrees, rollover to next revolution of the motor must be considered. For each measurement the difference in the angle from the previous measurement is stored. Figure 6.3 shows the angle difference measurements for a motor speed of 3500 units per 5 ms, figure 6.3a with the first angle measurement taken at 250 units, and figure 6.3b with the first angle measurement taken at 2000 units.

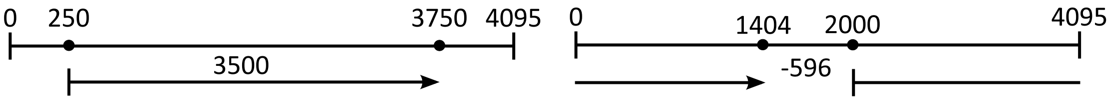

(a) No rollover (b) One rollover

Figure 6.3: Angle difference measurements at 3500 units / 5 ms

Based on the previously calculated speed and the angle difference measurement, the rollover is determined and corrected using the angle difference ranges shown in table 6.3. The unit of the values in the table is the raw AS5055 angle output difference per 5 ms. Acceleration is also taken into account with a margin of 500 units (1465 rpm) change per 100 ms.

Table 6.3: Rollover correction

Previously Calculated Speed	**Angle Difference Measurement**				
-6000 to -3000	1692 to 4095	-2404 to 1596	-4095 to -2500	-	-
-3000 to 0	-	596 to 3596	-3500 to 500	-4095 to -3596	-
0 to 3000	-	3596 to 4095	-500 to 3500	-4095 to -596	-
3000 to 6000	-	-	2500 to 4095	-1596 to 2404	-4095 to -1692
Rollovers	-2	-1	0	1	2
Correction	-8192	-4096	-	+4096	+8192

Figure 6.4 shows the speed measurements, derived using the two methods previously mentioned, when the control signal to the motor are at different constant values.

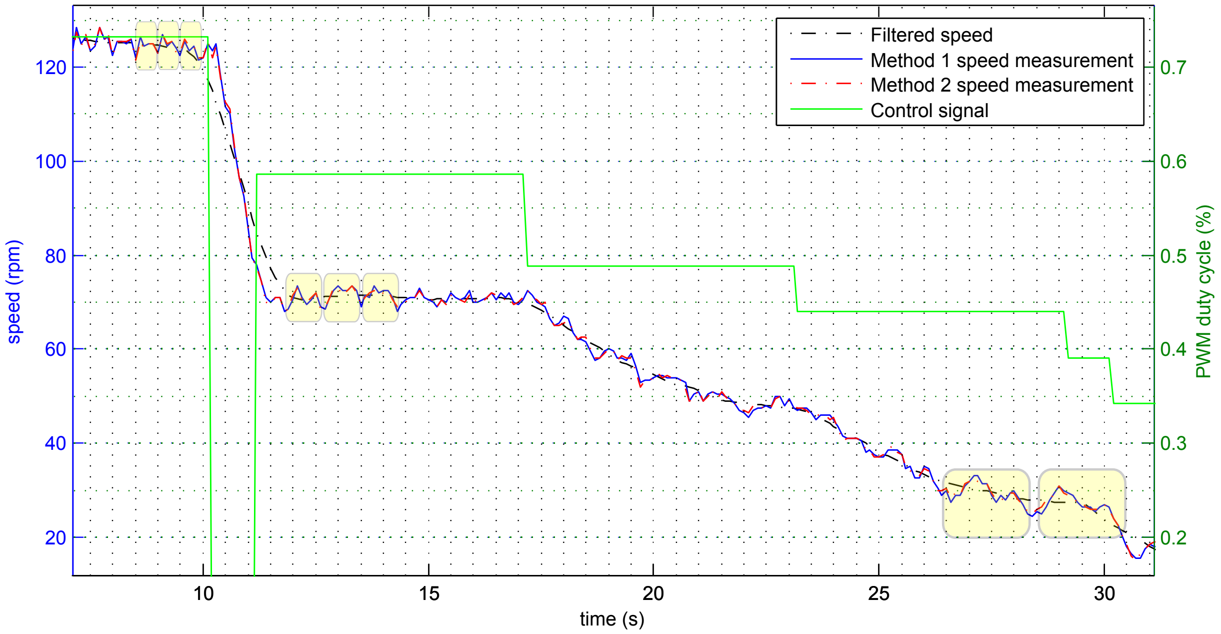

Figure 6.4: Slow speed measurements

The noise on the speed measurements is reduced with a 17 point symmetric moving average filter to obtain the filtered speed shown in the figure. We can see that there is little difference between the calculated speeds of the two methods. We also notice, highlighted in yellow, that there is a periodical deviation in the speed measurement. The period of this deviation is 0.5 s near 120 rpm, close to 1s at 70 rpm, and 2 s at 30 rpm. It correlates with a single rotation of the motor and indicates that the misalignment of the magnet dominates the measurement error.

Figure 6.5 shows the speed measurements when the control signal is slowly ramped up. Method one deviates from the filtered speed with as much 10 rpm peak, while the error of method two stays below 4 rpm. The noise on the speed measurements of method one also varies, reaching maximum noise levels at 540 s and 590 s and minimum noise levels at 565 s.

Figure 6.6 shows the absolute and RMS errors of both speed measurement methods when the motor speed is ramped from 0 to 10000 rpm. The error of method 1 has minimum values at $1200 \times n$ rpm speeds. This coincides with exact multiples of rotations being completed within the 50 ms sample time, which means that the angle measurements are taken at the same rotor position. This also indicates that the misalignment of the magnet causes periodic angle measurement errors over one revolution. The error of method 2 has

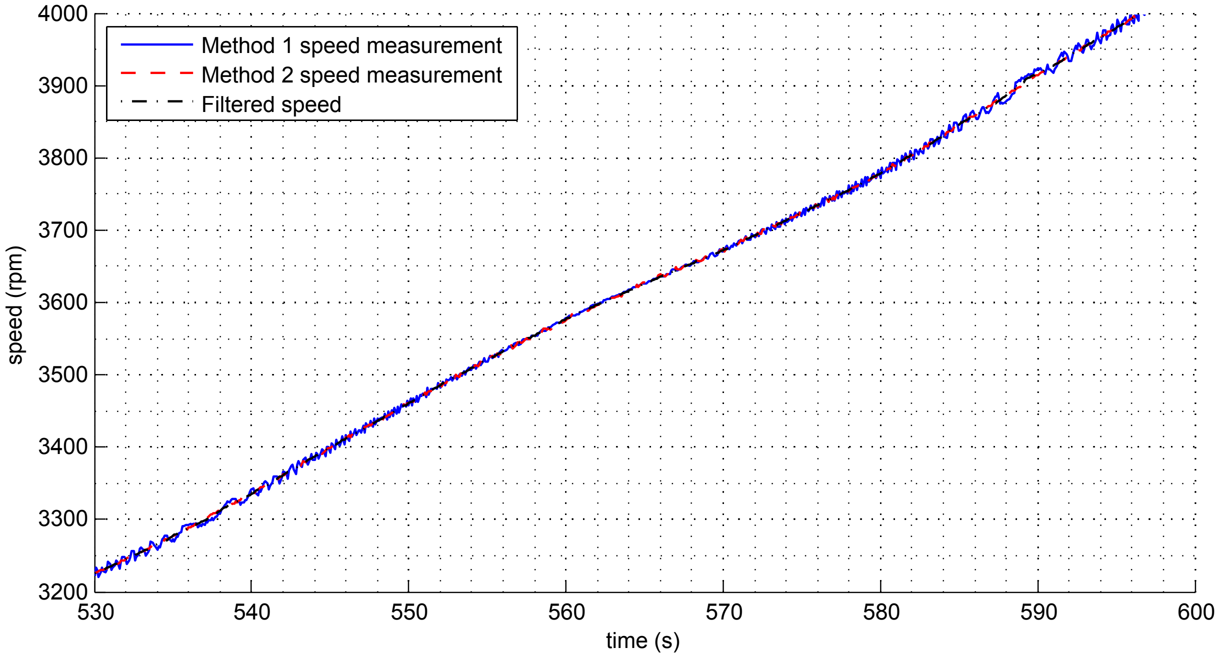

Figure 6.5: Ramp speed measurement noise

a minimum value at 6000 rpm, which coincides with half revolutions being completed in the 5 ms sample time. Method two generally performs better than method one at high speed, with an average RMS error at motor speeds between 1500 rpm and 5000 rpm of 1.4 rpm compared to a 3 rpm RMS error given by method 1. This is due to the better utilization of all the angle measurement samples in complete revolutions within the 50 ms sample time. Method two was used for speed calculation in the speed controller.

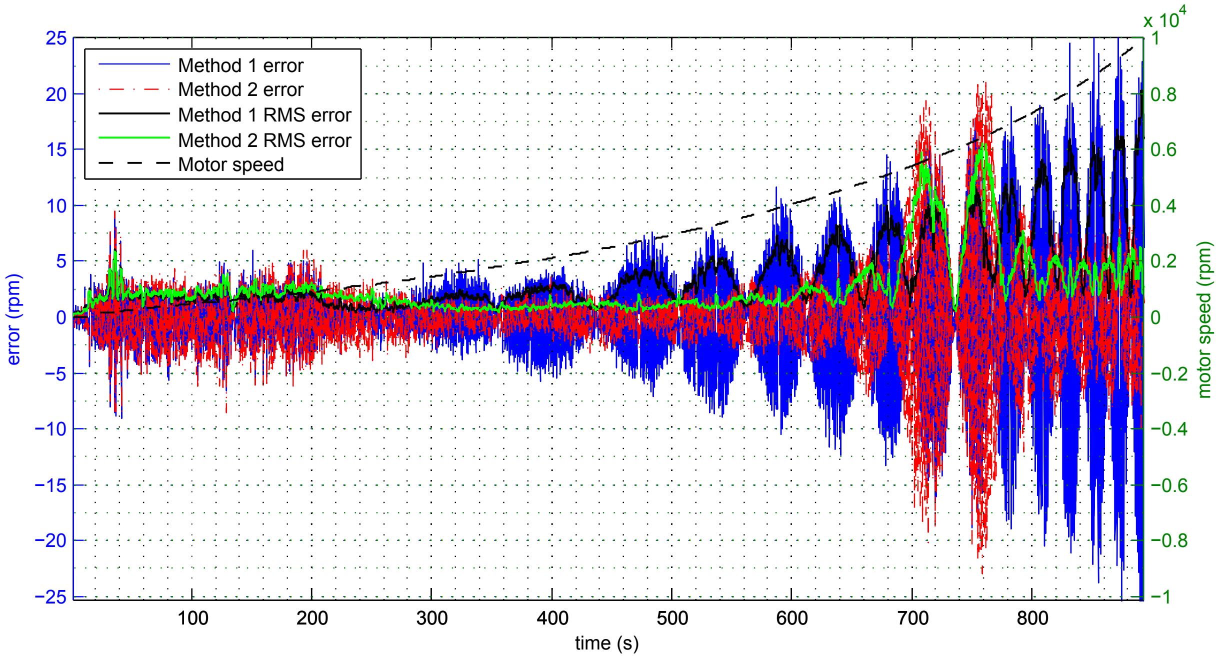

Figure 6.6: Ramp speed noise

6.3.2 Controller Model

The reaction wheel can be modelled as a single pole system, with the control signal from the MCU directly relating to motor current and angular acceleration. The angular acceleration, α_m, is expressed as:

$$\alpha_m = \frac{\tau_m}{I_{flywheel}} - \omega_m C_v, \tag{6.3.2}$$

with τ_m the motor torque and $I_{flywheel}$ the inertia of the flywheel. The motor speed is ω_m and C_v is the dynamic friction torque constant. The motor torque is,

$$\tau_m = I_m K_m, \tag{6.3.3}$$

with I_m the motor current and K_m the torque constant of the motor, defined in the specification sheet. The motor current is

$$I_m = PWM_{\%} I_{max}, \tag{6.3.4}$$

with $PWM_{\%}$ the duty cycle of the PWM control set by the MCU. I_{max} is maximum motor current defined in equation 4.1.1. Below is a model of the closed loop system with a PI controller.

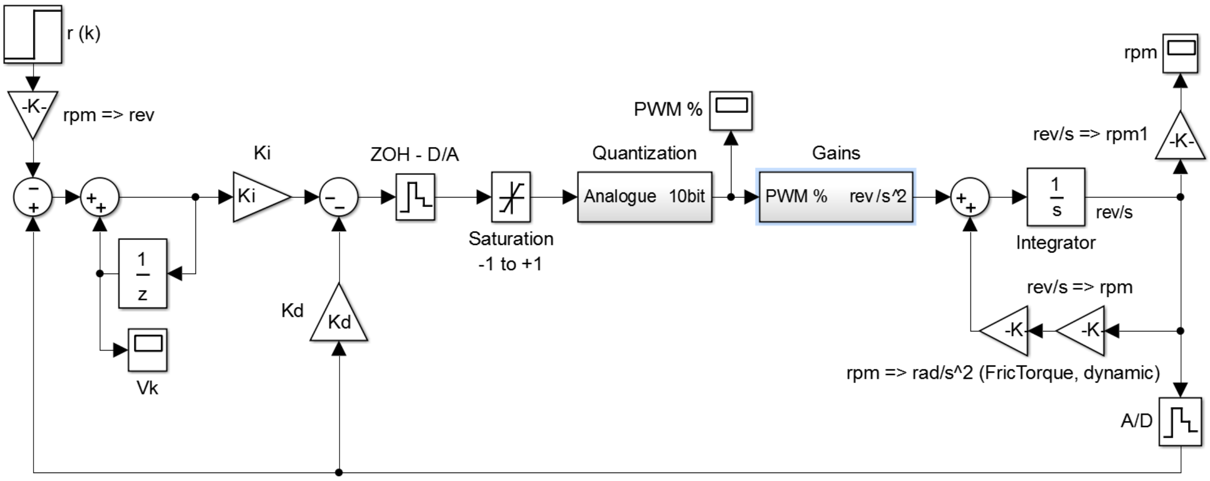
r (k)
-K-
rpm => rev
Ki
Ki
ZOH - D/A
PWM %
Quantization
Analogue 10bit
Gains
PWM % rev/s^2
Saturation
-1 to +1
1/z
Vk
Kd
Kd
1/s
rev/s
Integrator
rpm
rev/s => rpm1
-K-
rev/s => rpm
-K-
-K-
rpm => rad/s^2 (FricTorque, dynamic)
A/D

Figure 6.7: Reaction wheel closed loop model

The system was designed to be optimally damped with the damping factor $\zeta = 0.707$ and have a 2% settling time of 1s. The controller gains, K_i and K_d are calculated as proposed by Gerber [45].

6.3.3 Reaction Wheel Test Results

The reaction wheel was tested using the above mentioned speed calculation and speed control algorithms. In the following graphs the transient response of the motor is compared to that of the model.

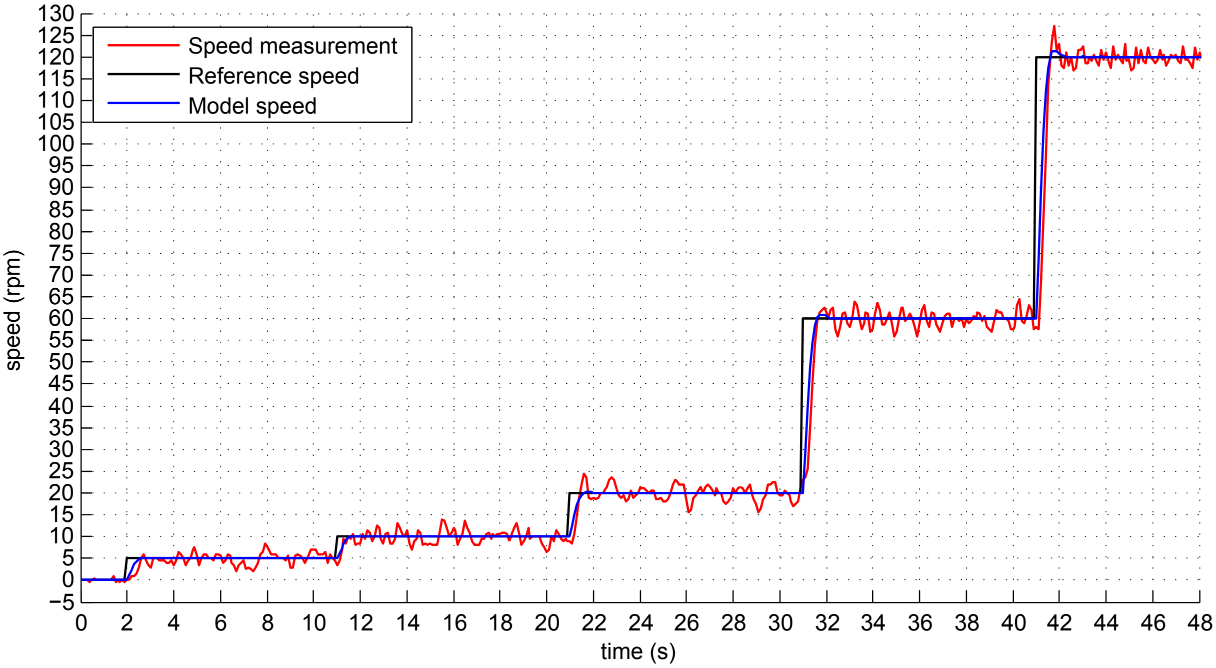

Figure 6.8: Low speed transient response

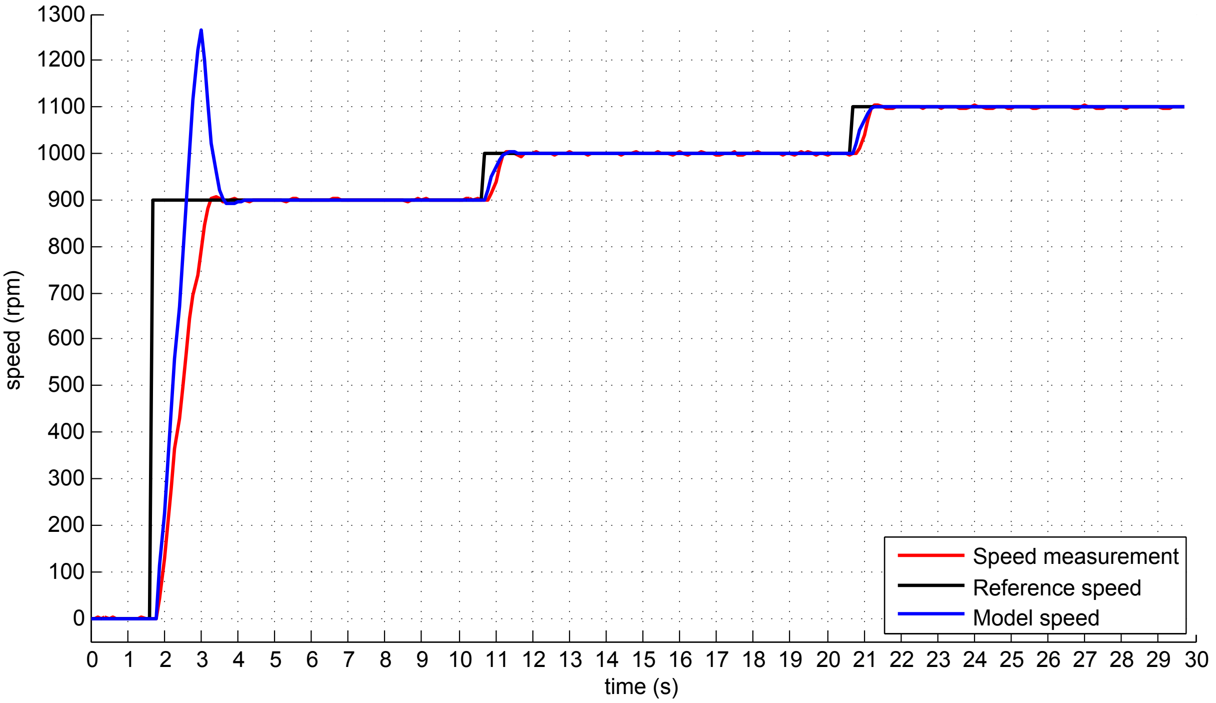

Figure 6.9: High speed transient response

Figure 6.8 shows the motor behaviour for a series of low speed step commands. The measured speed follows the reference speed with a RMS error of between 0.9 rpm and 2.4 rpm for speed commands as low as 5 rpm. The damping and settling time matches the modelled values closely.

In figure 6.9 the motor was given 900 rpm, 1000 rpm and 1100 rpm speed commands. The 900 rpm step command saturates the control signal, resulting in a longer settling time. It demonstrates that the integrator wind-up prevention described in section 5.6 successfully prevents undesired settling effects unlike the model which did not include integrator wind-up prevention. The steady state RMS noise at these speeds was between 0.9 rpm and 2.7 rpm.

Overall it was established that the motor speed could be controlled with an average RMS error of below 3 rpm. A motor speed of 3 rpm relates to an angular momentum of 0.622 μNms or an angular rate of 0.007 deg/s around the lowest inertia (0.005 kg m^2) axis of a 3kg 3-U CubeSat.

Chapter 7

Conclusion

This chapter concludes the thesis with a summary of the project. The results regarding the ADCS module design, hardware components and software design is given, followed by recommendations for further development.

7.1 ADCS Module Design

Research into previous CubeSat missions showed that, although their attitude control performance are generally still very limited compared to that of larger satellites, three axis ADCS modules are being developed, being necessary for many satellite applications. Reaction wheels were deemed necessary for accurate 3-axis control. The requirements of the ZACUBE-2 mission were analysed and it was concluded that a sensor and actuator interface module needed to be developed. This module, named CubeControl, together with CubeSense, a Nadir and fine sun sensor, and CubeComputer, an OBC, meet all the requirements for the mission and is comparable with commercial CubeSat ADCS modules.

7.2 Hardware Development

Viable components were identified for all the required sensors and actuators. Schematics and PCB designs were made to incorporate all the hardware. Two engineering modules of a CubeControl PCB with three reaction wheels for the ZACUBE-2 mission were manufactured. PCBs for a deployable magnetometer and magnetic encoders for a reaction were also designed and manufactured. All the sensors and actuators were tested using a MATLAB interfacing program and a CubeDock module, which communicates with the CubeControl module in a manner representative of an OBC.

The magnetorquer design proposed by Mey [18] was adapted to enable two MCUs to drive the magnetorquers, providing redundancy for magnetic control. A magnetorquer coil was also designed which, with two magnetorquer rods in a T-formation, provides a compact 3-axis solution.

The HMC1053 magnetometer was mounted on a small separate PCB along with a 16-bit ADC, which communicates to a MCU over an I2C interface, to maximize the sensor accuracy. The magnetometer outputs are also sampled by a secondary MCU for magnetic control redundancy.

Two MEMS rate sensors, the LCG50-100 and the CRM200, were evaluated. With proper filtering, both sensors provided angular rate information with low enough noise levels to be useful during detumbling. With bias estimation, using and accurate attitude sensor such as a fine sun sensor, the LCG50-100 will provide marginally less noise than the CRM200, but the CRM200 is simpler to incorporate on the CubeControl module and has a lower power consumption, for which reasons it was chosen for use on CubeControl.

The angular control of the aerodynamic paddles will be done using two stepper motors and an IR LED and phototransitor IC. Tests found that the angle of the paddle will be controllable with a 0.56° resolution. The centre position can also be sensed with this accuracy.

A coarse sun sensor was implemented using six photodiodes. A tuned sine function was used to characterize the relation between the AD output and light incidence angle. It was concluded that the light incidence vector can be measured with an accuracy of below 5° for the entire FOV.

A reaction wheel was designed using a FAULHABER 1509 006 B BLDC Micromotor, a L6235 BLDC driver and a AS5055 angular encoder. A speed control algorithm designed for the reaction wheel was able to follow speed commands as low as 5rpm with an RMS error of 3 rpm, or 0.622 μNms.

7.3 Software Design

Software for the CubeControl module was developed with special attention given to scheduling the different operations within a 1 second control period. A special synchronize command also ensures that the actuator commands are set and sensor data is read at a constant rate and with short delays, which is required for the ADCS controllers. The software and hardware was tested using a MATLAB GUI, S-function and a CubeDOCK module which communicated with CubeControl in a manner representative of an OBC.

7.4 Other Missions

The hardware design was adapted to suit the needs of the DeOrbitSail mission and the QB50 mission, each for which engineering and flight modules were manufactured. For these missions a design for a momentum wheel was used. Correct functioning of the CubeControl module used in the QB50 mission was verified within a ADCS bundle, also containing a CubeComputer and CubeSense module. Two of these ADCS bundles have been flown in the QB50 precursor missions. Successful detumbling has already been demonstrated on the QB50P1 and QB50P2 satellite.

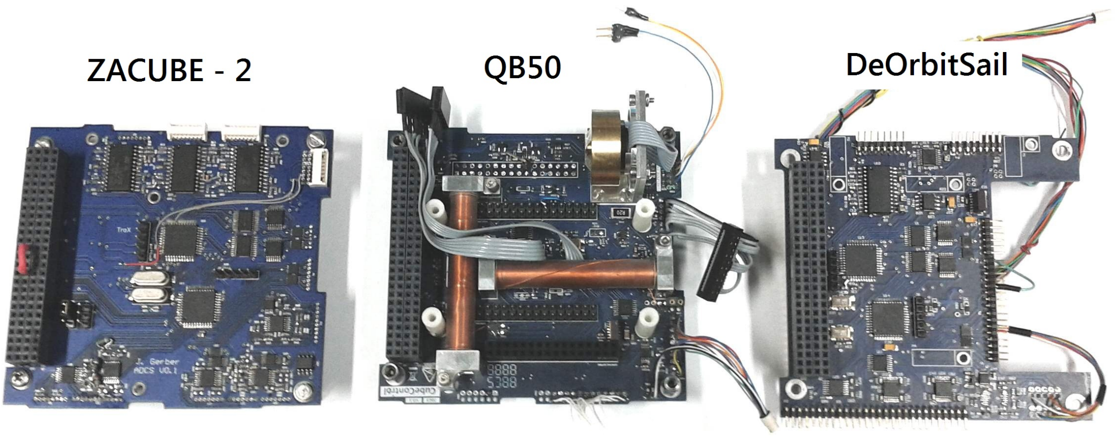

Figure 7.1: Mission specific CubeControl modules

7.5 Further Recommendations

The speed measurement and performance of the reaction wheel can be improved by better alignment of the magnetic encoder, diametrically magnetized magnet and the motor rotor shaft. To do this a better quality encoder PCB with tighter mounting tolerances need to be designed. Misalignment can also be compensated for in software by measuring the angle output error and storing the error value in a lookup table which can then be used to correct discrepancies. A final design for a mounting bracket for three wheels must still be designed. A method for measuring the vibrations in the motor due to unbalances to ensure that it is within acceptable limits must also be developed. Research in other BLDC motor drivers can be done to see if improvement can be made which regard to the minimum allowable voltage and power use.

A temperature measurement circuit, which can give the MCU a digital reading on the temperature, can be implemented in the magnetometer circuit. This will allow the temperature calibration to occur in software as well as ensuring that the temperature stays within acceptable limits. The calibration procedure for the magnetometers can be improved by also calculating the misalignment of the HMC1053 axis as they are not perfectly orthogonal.

Research in modelling the effect of the Earth albedo on the coarse sun sensors can be done in order to improve the accuracy. The effect of different configurations of the photodiodes on the accuracy of the sun vector measurement can be investigated.

A test setup with the entire ADCS bundle, mounted on a three-axis rotation table, which tests the functioning of the fine sun sensor, earth sensor, magnetometer, magnetorquers, rate sensors and reaction wheels in unison can be developed. This will serve to verify the operation of all subsystems and point out possible future improvements. In addition, a procedure for the in-situ calibrating of the different sensors in this test setup, or in flight, must be developed.

Bibliography

[1] R. Munakata, *CubeSat Design Specification*, Cal Poly SLO, January 2009. [Online]. Available: http://www.srl.utu.fi/AuxDOC/tke/radmon/cubesat_standard.pdf

[2] J. Bouwmeester and J. Guo, “Survey of worldwide pico-and nanosatellite missions, distributions and subsystem technology,” *Acta Astronautica*, vol. 67, no. 7, pp. 854–862, 2010.

[3] K. Sarda, C. Grant, S. Eagleson, D. Kekez, and R. Zee, “Canadian advanced nanospace experiment 2: On-orbit experiences with a three-kilogram satellite,” in *22nd Annual AIAA/USU Conference on Small Satellites*, 2008.

[4] J. C. Springmann and J. W. Cutler, “Flight results of a low-cost attitude determination system,” *Acta Astronautica*, vol. 99, pp. 201–214, 2014.

[5] D. Werner, “Commercial Spaceflight — With 2 More Cubesats in Orbit, Earth-imaging Startup Planet Labs Ships Next Batch of 28 to Wallops,” *Space News*, November 2013.

[6] C. Boshuizen, *Dove-3 Orbital Debris Assessment Report (ODAR)*, Cosmogia, September 2012. [Online]. Available: https://apps.fcc.gov/els/GetAtt.html?id=130310&x=.

[7] H. Kayal, F. Baumann, K. Briess, and S. Montenegro, “Beesat: A pico satellite for the on-orbit verification of micro wheels,” in *3rd International Conference on Recent Advances in Space Technologies.* IEEE, 2007, pp. 497–502.

[8] K. Briess, F. Baumann, and S. Trowitzsch, “Present and future picosatellite missions at TU Berlin,” in *8th Int. Symp. of IAA on Small Satellites for Earth Observation, Berlin*, 2011, pp. 49–52.

[9] B. Johnston-Lemke, K. Sarda, C. Grant, and R. Zee, “Arc-minute attitude stability on a nanosatellite: Enabling stellar photometry on the smallest scale,” in *25th Annual AIAA/USU Conference on Small Satellites*, 2011.

[10] "Orbital elements," Ocotber 2007. [Online]. Available: http://en.wikipedia.org/wiki/Orbital_elements

[11] G. Smith, "Radiation: An invisible invader throughout the galaxy!" October l997. [Online]. Available: http://quest.arc.nasa.gov/people/journals/space/smith/radiation10-07.html

[12] *AN213: Set/Reset function for magnetic sensors*, Honeywell. [Online]. Available: http://www.seraphim.com.tw/upfiles/c_supports01284968029.pdf

[13] *AN 212: Handling Sensor Bridge Offset*, Honeywell. [Online]. Available: http://www51.honeywell.com/aero/common/documents/myaerospacecatalog-documents/Defense_Brochures-documents/Magnetic__Literature_Application_notes-documents/AN212_Handling_of_Sensor_Bridge_Offset.pdf

[14] J. Auret, "Design of an aerodynamic attitude control system for a CubeSat," Master's thesis, Stellenbosch University, March 2012.

[15] "QB50: The project," April 2014. [Online]. Available: https://www.qb50.eu/index.php/project-description-obj

[16] P. J. Botma, "The design and development of an ADCS OBC for a CubeSat," Master's thesis, Stellenbosch University, 2011.

[17] H. E. Loubser, "The development of sun and nadir sensors for a solar sail CubeSat," Master's thesis, University of Stellenbosch, March 2011.

[18] P. H. Mey, "Development of attitude controllers and actuators for a solar sail Cubesat," Master's thesis, Stellenbosch University, March 2011.

[19] J. Puig-Suari, C. Turner, and W. Ahlgren, "Development of the standard cubesat deployer and a cubesat class picosatellite," in *Aerospace Conference*, vol. 1. IEEE, 2001, pp. 1–347.

[20] "CUTE-I Attitude Determination Subsystem (ADS)," June 2003. [Online]. Available: http://lss.mes.titech.ac.jp/ssp/cubesat/index_e.html

[21] "Michael's list of cubesat satellite missions," August 2009. [Online]. Available: http://mtech.dk/thomsen/space/cubesat.php

[22] M. Swartwout, "Cubesat database," 2014. [Online]. Available: https://sites.google.com/a/slu.edu/swartwout/home/cubesat-database

[23] K. Woellert, P. Ehrenfreund, A. J. Ricco, and H. Hertzfeld, "Cubesats: Cost-effective science and technology platforms for emerging and developing nations," *Advances in Space Research*, vol. 47, no. 4, pp. 663–684, 2011.

[24] D. Selva and D. Krejci, "A survey and assessment of the capabilities of Cubesats for Earth observation," *Acta Astronautica*, vol. 74, pp. 50–68, 2012.

[25] K. Sarda, C. Grant, S. Eagleson, D. D. Kekez, and R. E. Zee, "Canadian advanced nanospace experiment 2 orbit operations: two years of pushing the nanosatellite performance envelope," in *ESA Small Satellites, Services and Systems Symposium*, 2010.

[26] D. Rankin, D. D. Kekez, R. E. Zee, F. M. Pranajaya, D. G. Foisy, and A. M. Beattie, "The CanX-2 nanosatellite: expanding the science abilities of nanosatellites," *Acta Astronautica*, vol. 57, no. 2, pp. 167–174, 2005.

[27] "Gunter's space page," 2014. [Online]. Available: http://space.skyrocket.de/

[28] Q. Hardy and N. Bilton, "Start-ups aim to conquer space market," *The New York Times*, March 2014.

[29] "Dove-1 and Dove-2 nanosatellites," 2014. [Online]. Available: https://directory.eoportal.org/web/eoportal/satellite-missions/d/dove

[30] "BeeSat-1 (Berlin experimental educational satellite-1)," 2014. [Online]. Available: https://directory.eoportal.org/web/eoportal/satellite-missions/b/beesat-1

[31] K. Carroll, S. Rucinski, and R. Zee, "Arc-minute nanosatellite attitude control: Enabling technology for the BRITE stellar photometry mission," in *18th Annual AIAA/USU Conference on Small Satellites*, 2004.

[32] W. J. Larson, J. R. Wertz *et al.*, *Space mission analysis and design.* Microcosm, 1992.

[33] W. H. Steyn, "A multi-mode attitude determination and control system for small satellites," Ph.D. dissertation, Stellenbosch University, 1995.

[34] "Understanding space radiation," October 2002. [Online]. Available: http://spaceflight.nasa.gov/spacenews/factsheets/pdfs/radiation.pdf

[35] A. Barnard, "Overview of space radiation environments and effects," Presentation, Stellenbosch University, 2013.

[36] P. Chetty, *Satellite technology and its applications.* Tab Books, 1988.

[37] J. R. Wertz, *Spacecraft Attitude Determination and Control.* D. Reidel Publishing Company, 1978.

[38] M. Díaz-Michelena, "Small magnetic sensors for space applications," *Sensors*, vol. 9, no. 4, pp. 2271–2288, 2009.

[39] E. Matandirotya, R. R. Van Zyl, D. J. Gouws, and E. F. Saunderson, "Evaluation of a commercial-off-the-shelf fluxgate magnetometer for cubesat space magnetometry," *JoSS*, vol. 2, pp. 133–146, 2013.

[40] H. Hauser, L. Kraus, and P. Ripka, "Giant Magnetoimpedance Sensors," *IEEE Instrumentation & Measurement Magazine*, pp. 28–32, June 2001.

[41] J. A. Geen, S. J. Sherman, J. F. Chang, and S. R. Lewis, "Single-chip surface micromachined integrated gyroscope with 50/h allan deviation," *IEEE Journal of Solid-State Circuits*, vol. 37, no. 12, pp. 1860–1866, 2002.

[42] I. Song and B. Lee, "Mems-based angular rate sensors," in *Proceedings of IEEE Sensors 2004.* IEEE publication, 2004, pp. 650–653.

[43] S. Chapman, *Electric machinery fundamentals.* Tata McGraw-Hill Education, 2005.

[44] *L6235: DMOS Driver for three-phase brushless DC motor*, STMicroelectronics. [Online]. Available: http://www.st.com/web/en/resource/technical/document/datasheet/CD00002347.pdf

[45] J. Gerber, "Nano-reaction wheel for cubesat applications," Final Year Project, Stellenbosch University, Descember 2010.

[46] J. Karki, "Active low-pass filter design," Application report, Texas Instruments, July 2000. [Online]. Available: http://www.ti.com/lit/an/sloa049b/sloa049b.pdf

[47] P. Cheung, "Poles, zeros and filters," Class Notes, Imperial College, February 2011. [Online]. Available: http://www.ee.ic.ac.uk/pcheung/teaching/ee2_signals/Lecture%209%20-%20Poles%20Zeros%20&%20Filters.pdf

[48] H. Hou, "Modeling inertial sensors errors using allan variance," Master's thesis, University of Calgary, September 2004.

[49] *IEEE Standard Specification Format Guild and Test Procedure for Single-Axis Interferometric Fiber Optic Gyros*, IEEE Standard, Descember 2008. [Online]. Available: http://www.control.aau.dk/uav/reports/12gr1052/sources/books_and_rapports/allan_variance_IEEE.pdf

[50] W. H. Steyn, “An Attitude Control System for SumbandilaSAT an Earth Observation Satellite,” in *The 4S (Small Satellite Systems and Services) Symposium.* Rhodes Greece: ESA Proceedings SP-660, May 2008.

Appendices

Appendix A

Mechanical Drawings

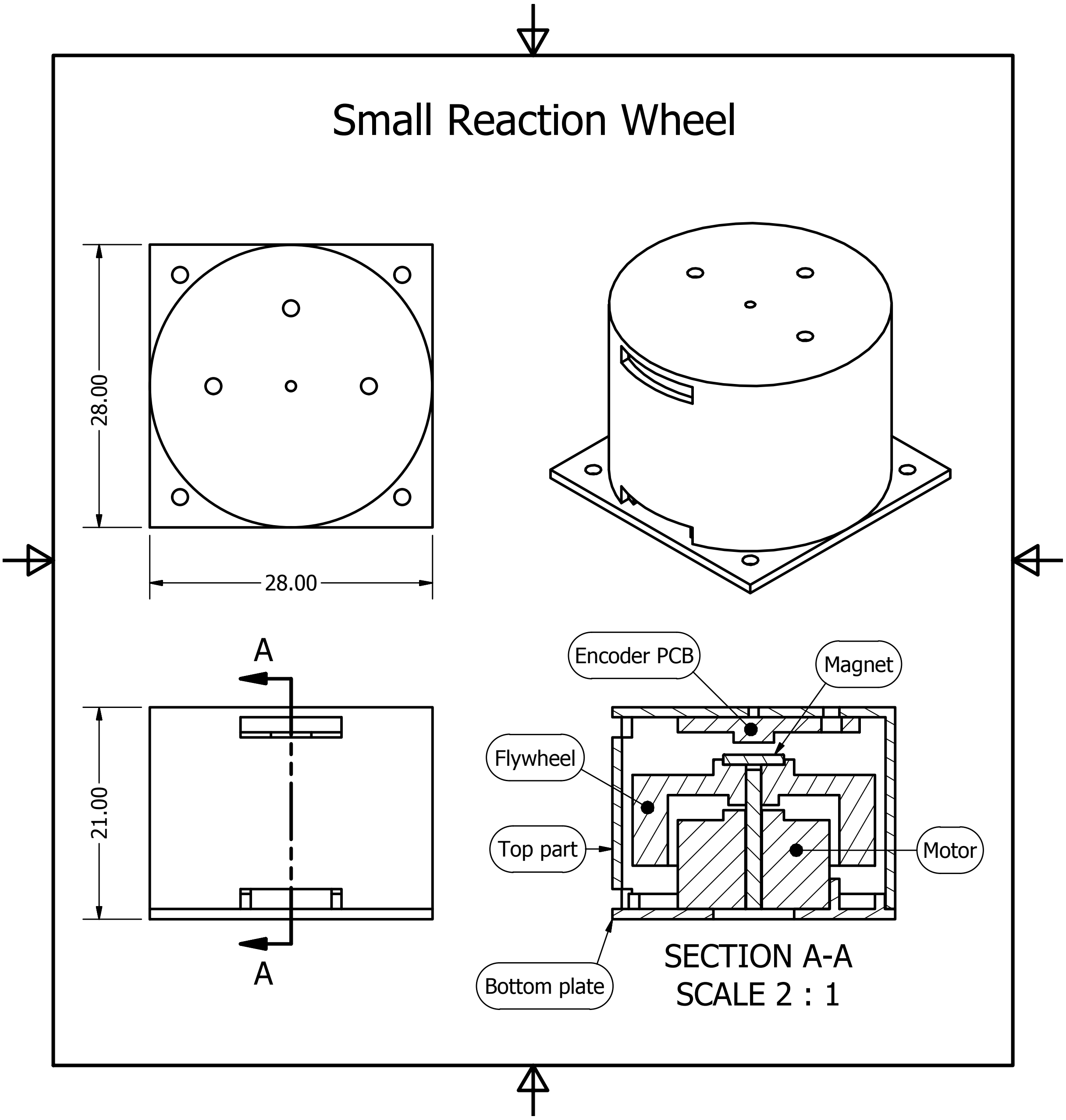
Small Reaction Wheel
28.00
28.00
A
21.00
A
Encoder PCB
Magnet
Flywheel
Top part
Motor
Bottom plate
SECTION A-A
SCALE 2 : 1

Appendix B

Simulink GUI

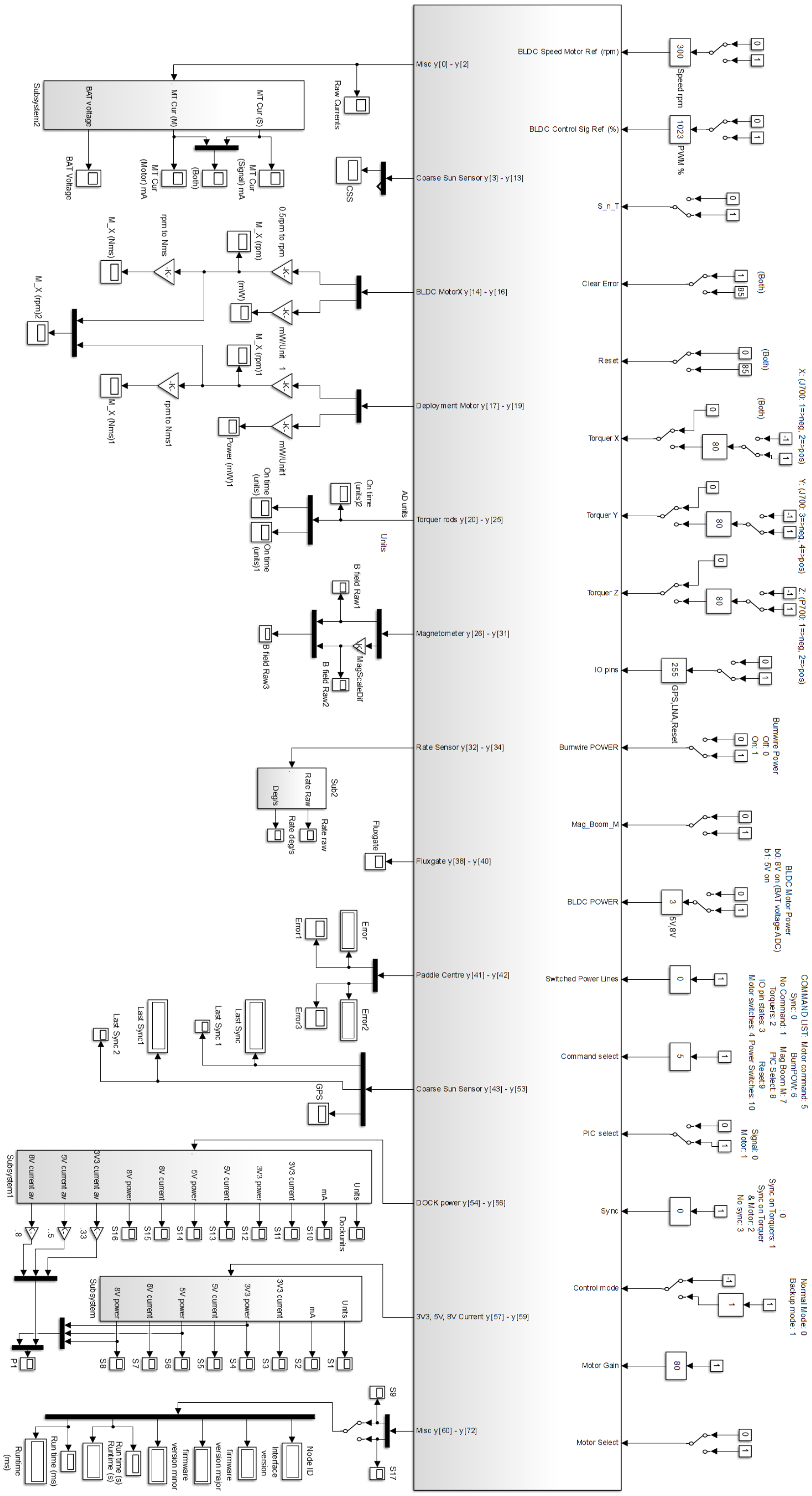
Misc y[0] - y[2]
Coarse Sun Sensor y[3] - y[13]
BLDC MotorX y[14] - y[16]
Deployment Motor y[17] - y[19]
Torquer rods y[20] - y[25]
Magnetometer y[26] - y[31]
Rate Sensor y[32] - y[34]
Fluxgate y[38] - y[40]
Paddle Centre y[41] - y[42]
Coarse Sun Sensor y[43] - y[53]
DOCK power y[54] - y[56]
3V3, 5V, 8V Current y[57] - y[59]
Misc y[60] - y[72]
BLDC Speed Motor Ref (rpm)
BLDC Control Sig Ref (%)
S_n_T
Clear Error
Reset
Torquer X
Torquer Y
Torquer Z
IO pins
Burnwire POWER
Mag_Boom_M
BLDC POWER
Switched Power Lines
Command select
PIC select
Sync
Control mode
Motor Gain
Motor Select
300
Speed rpm
1023
PWM %
(Both)
X: (J700: 1=>neg, 2=>pos)
Y: (J700: 3=>neg, 4=>pos)
Z: (P700: 1=>neg, 2=>pos)
80
255
GPS,LNA,Reset
Burnwire Power
Off 0
On 1
BLDC Motor Power
b0: 8V on (BAT voltage ADC)
b1: 5V on
3
5V8V
COMMAND LIST: Motor command 5
Sync 0
No Command 1
Torquers 2
IO pin states 3
Motor switches 4
BurnPOW 6
Mag Boom M 7
PIC Select 8
Reset 9
Power Switches 10
Signal 0
Motor 1
Sync on Torquers 1
& Motor 2
No sync 3
Normal Mode 0
Backup mode 1
Raw Currents
Subsystem2
BAT v voltage
MT Cur (M)
MT Cur (S)
BAT Voltage
MT Cur (Motor) mA
(Both)
MT Cur (Signal) mA
CSS
0.5rpm to rpm
M_X (rpm)
rpm to Nms
M_X (Nms)
(mW)
M_X (rpm)2
mW/Unit
M_X (rpm)1
rpm to Nms1
M_X (Nms)1
mW/Unit1
Power (mW)1
AD units
Units
On time (units)2
On time (units)
On time (units)1
B field Raw1
MagScaleDif
B field Raw2
B field Raw3
Sub2
Rate Raw
Deg/s
Rate raw
Rate deg/s
Fluxgate
Error
Error1
Error2
Error3
Last Sync
Last Sync1
Last Sync1
Last Sync 2
GPS
Subsystem1
Units
mA
3V3 current
5V current
8V current
3V3 power
5V power
8V power
3V3 current av
5V current av
8V current av
Dockunits
S10
S11
S12
S13
S14
S15
S16
3.3
5
8
Subsystem
S1
S2
S3
S4
S5
S6
S7
S8
P1
S9
S17
Node ID
Interface version
firmware version major
firmware version minor
Run time (s)
Runtime (s)
Run time (ms)
Runtime (ms)